TU/e EINDHOVEN UNIVERSITY OF TECHNOLOGY

Evaluation of constitutive equations for polymer melts and solutions in complex flows

Citation for published version (APA):
Baaijens, J. P. W. (1994). *Evaluation of constitutive equations for polymer melts and solutions in complex flows*. [Phd Thesis 1 (Research TU/e / Graduation TU/e), Mechanical Engineering]. Technische Universiteit Eindhoven. https://doi.org/10.6100/IR427177

DOI:
10.6100/IR427177

Document status and date:
Published: 01/01/1994

Document Version:
Publisher's PDF, also known as Version of Record (includes final page, issue and volume numbers)

Please check the document version of this publication:

• A submitted manuscript is the version of the article upon submission and before peer-review. There can be important differences between the submitted version and the official published version of record. People interested in the research are advised to contact the author for the final version of the publication, or visit the DOI to the publisher's website.
• The final author version and the galley proof are versions of the publication after peer review.
• The final published version features the final layout of the paper including the volume, issue and page numbers.

Link to publication

General rights
Copyright and moral rights for the publications made accessible in the public portal are retained by the authors and/or other copyright owners and it is a condition of accessing publications that users recognise and abide by the legal requirements associated with these rights.

• Users may download and print one copy of any publication from the public portal for the purpose of private study or research.
• You may not further distribute the material or use it for any profit-making activity or commercial gain
• You may freely distribute the URL identifying the publication in the public portal.

If the publication is distributed under the terms of Article 25fa of the Dutch Copyright Act, indicated by the "Taverne" license above, please follow below link for the End User Agreement:

www.tue.nl/taverne

Take down policy
If you believe that this document breaches copyright please contact us at:

openaccess@tue.nl

providing details and we will investigate your claim.

Download date: 04. Oct. 2023

Evaluation of Constitutive Equations for Polymer Melts and Solutions in Complex Flows

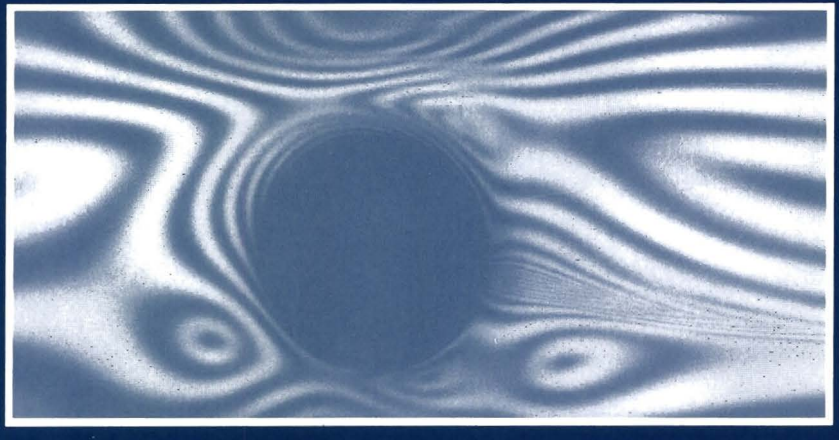

Hans Baaijens

Evaluation of Constitutive Equations for Polymer Melts and Solutions in Complex Flows

CIP-DATA KONINKLIJKE BIBLIOTHEEK, DEN HAAG

Baaijens, Johannes Petrus Wilhelmus

Evaluation of constitutive equations for polymer melts and solutions in complex flows / Johannes Petrus Wilhelmus Baaijens. - Eindhoven : Eindhoven University of Technology
Thesis Eindhoven. - With ref. - With summary in Dutch.
ISBN 90-386-0334-7
Subject headings: constitutive equations / viscoelastic flows

Druk: FEBO-Druk, Enschede

Evaluation of Constitutive Equations for Polymer Melts and Solutions in Complex Flows

PROEFSCHRIFT

ter verkrijging van de graad van doctor
aan de Technische Universiteit Eindhoven
op gezag van de Rector Magnificus, prof.dr. J.H. van Lint,
voor een commissie aangewezen door het College van Dekanen
in het openbaar te verdedigen
op woensdag 7 december 1994 om 16.00 uur

door

JOHANNES PETRUS WILHELMUS BAAIJENS

geboren te 's-Hertogenbosch

Dit proefschrift is goedgekeurd door de promotoren:

prof.dr.ir. H.E.H. Meijer
prof.dr.ir. F.P.T. Baaijens

en de copromotor:

dr.ir. G.W.M. Peters

Voor Daniëlle

Contents

Summary iii

1 Introduction 1
- 1.1 Context of this study . . . 1
- 1.2 Isothermal flow of incompressible, viscoelastic fluids . . . 4
- 1.3 A literature survey on combined experimental - numerical studies of viscoelastic complex flow fields . . . 7
- 1.4 Viscoelastic flow past cylinders . . . 10
- 1.5 Objectives and outline of this thesis . . . 12

2 Experimental methods and equipment 15
- 2.1 Introduction . . . 15
- 2.2 Laser Doppler anemometry . . . 15
- 2.3 Flow Induced Birefringence . . . 19
- 2.4 Discussion . . . 31

3 Rheological characterization in simple shear 35
- 3.1 Introduction . . . 35
- 3.2 Constitutive equations . . . 36
- 3.3 Definition of deformation types and material functions . . . 37
- 3.4 5% PIB/C14 solution . . . 38
- 3.5 9% PIB/C14 solution . . . 45
- 3.6 S1 solution . . . 48
- 3.7 LDPE melt . . . 54
- 3.8 Conclusions and discussion . . . 56

4 Steady flow of polyisobutylene solutions past a cylinder 59
- 4.1 Introduction . . . 59
- 4.2 Flow loop and flow cell . . . 60
- 4.3 Flow of 5 % PIB/C14 solution past a symmetrically confined cylinder . . . 60
- 4.4 Flow of 5 % PIB/C14 past an asymmetrically confined cylinder . . . 78
- 4.5 Flow past a cylinder for a 9 % PIB/C14 solution . . . 83
- 4.6 Discussion . . . 91

4.7 Summary and conclusions 97

5 Flow of LDPE melt past a confined cylinder **101**
5.1 Introduction 101
5.2 Experimental aspects 101
5.3 Computational aspects 102
5.4 Results 107
5.5 Conclusions and discussion 115

6 Conclusions and recommendations **117**
6.1 Conclusions 117
6.2 Recommendations 118

A Electromagnetic description of light **121**
A.1 Introduction 121
A.2 Maxwell equations 121
A.3 The electromagnetic wave equation 122

B Müller matrices **123**

C Laser beam dimensions **125**

D Measurement of stress optical coefficient in Couette flow **127**

E Estimation of statistical error in stresses measured with ROA **129**

References **133**

Samenvatting **141**

Acknowledgement **143**

Curriculum Vitae **145**

Summary

Realistic simulations of practical flows of viscoelastic polymeric liquids may benefit the development and optimization of industrial processing techniques (like injection molding, film blowing, mixing and compounding), improve the quality of the final product and reduce production costs. For example, the accurate prediction of frozen-in flow induced molecular orientation in injection molded products depends strongly on the adequacy of the modelling of the viscoelastic behavior of the melt during flow. This orientation, that is associated with the flow induced stress distribution, determines the anisotropy of physical properties and the long-term dimensional stability of the product.

Usually, constitutive equations are tested in simple shear flows. However, simple shear flows do not contain enough information on the fluid rheology to ensure reliable predictions in more complex flows (see for example Douven [32] and Tas [107]). In many cases the viscometric functions can only be measured in a range of shear rates that is smaller than the range present in the actual practical flow. Furthermore, measurement of material functions in elongational flows are often unreliable or impossible (Walters [112]). Therefore apart from simple shear flow, *complex flow* should be used to find the (parameters of) constitutive equations for polymer melts and solutions. In the past two decades, numerous constitutive equations have been proposed and, with the development of new reliable numerical techniques, simulations with viscoelastic constitutive models can be made presently in a reasonable range of complex flows. The mission is now to compare numerical simulations of these flows with experimental data to investigate the adequacy of the constitutive model used. Moreover, the measured data in complex flow can be used to improve the fit of the model parameters.

As a first step to this final goal, in this thesis the benchmark problem of the stagnation flow past a circular cylinder is used to test constitutive equations in a more rigorous way. Both a symmetrically and an asymmetrically confined cylinder are used. The constitutive equations are tested by means of a comparison of measured data of the velocity and/or stress field with finite element simulations. To facilitate the analysis both experimentally and computationally, model fluids are used instead of polymer melts in the main part of this study. Most results are obtained for a shear-thinning solution of 5% (w/w) polyisobutylene in tetradecane (referred to with 5% PIB/C14). In case of a low density polyethylene (LDPE) melt, a preliminary analysis is made using the same geometry.

First, model parameters are fitted on data measured in simple shear for two viscoelastic constitutive equations, the Phan-Thien Tanner (PTT) and Giesekus models. Both single

and four mode versions of these models are fitted, and their overall behavior is evaluated (in small strain oscillatory shear, steady shear and start-up of steady shear flow after a step in shear rate).

Second, for two polymer solutions pointwise measured velocity (with laser Doppler anemometry) and stress field (with flow induced birefringence) in the flow past a confined cylinder are compared with finite element simulations. Measured velocities and stresses agree well to excellently with the results of finite element computations. In case of the 5% PIB/C14 solution a comparison is made at five Deborah numbers between 0.25 and 2.31. Models with four modes instead of a single mode improve the agreement significantly. Differences between the four mode PTT and Giesekus equation are small. In case of a 9%(w/w) solution, larger differences are observed. For reference, simulations with a generalized Newtonian model (Carreau-Yasuda) are made as well. This model describes the velocity field excellently, implying that no pronounced effect of elongational stresses on the velocity field is present in the flows investigated. However, normal stresses can not be described realistically with a generalized Newtonian model, not even in a qualitative way.

Third, a preliminary analysis of the flow past a confined cylinder of a LDPE melt is made by comparing finite element simulations with (fieldwise) measured isochromatic birefringence patterns. The simulations with viscoelastic constitutive models were performed at Deborah numbers as high as 9.8. Measured fringe patterns agree moderately with the computed patterns. Most remarkably, in all cases the measured fringes are more concentrated near the cylinder surface and the downstream (stress) 'weld line' compared to the computed fringes.

The main conclusions and recommendations can be summarized as follows. (i) The experimental methods used proved to be powerful tools. (ii) The planar flows of the polymer solutions as investigated can be simulated quantitatively well. In future work on polymer solutions it is recommended, besides using higher Deborah numbers, to search a flow situation where normal stresses have a more pronounced influence on the velocity field, such that the flow discriminates more between the different models. (iii) In case of the LDPE melt, the observed discrepancy between experiments and computations is attributed to a deficiency of the models used. Evidently, in future studies these models should be improved. Moreover, apart from measurements of the stress field, the velocity field should be determined experimentally. (iv) Extension to the analysis of the transient rheological behavior of the fluid during start-up of the flow around the cylinder is promising as an even more rigorous test for the models.

Chapter 1

Introduction

1.1 Context of this study

Numerical simulations of complex flows of viscoelastic polymeric fluids are of practical relevance to develop and optimize polymer processing techniques. Examples are extrusion, (multi-layer) injection moulding, film-blowing and mixing. However, the application of such simulations in an industrial engineering environment is not widespread yet. The main reasons for this are the complexity of (i) the rheological behavior which has to be captured in a realistic *constitutive equation*, (ii) the adequate determination of its parameters, and (iii) the numerical problem that is obtained with the constitutive equation, which requires sophisticated numerical techniques and extended computer facilities.

The non-Newtonian behavior of polymeric liquids is related to their structure and is manifest in a number of physical phenomena that can not be observed in a Newtonian fluid (examples are shear thinning viscosity, normal stresses in simple shear and die swell; see Larson [70], Tanner [106]). The rheological behavior of macromolecular polymeric fluids has appeared to be so complex that attempts to describe their behavior has lead to the proposition of numerous and diverse constitutive equations. The choice of an appropriate constitutive equation is a central problem in rheology of complex fluids.

A comparison of computed results, obtained after choosing a constitutive equation with its proper material parameters, with measured (macroscopic) data must reveal whether the constitutive equation is adequate. In this thesis, the benchmark problem of viscoelastic flow past a cylinder with $R/h = 1/2$ (R: radius cylinder, h: half height of the channel) is used to test constitutive equations. It is one of the benchmarks problems for numerical techniques (Hassager [49]), and which was particularly recommended at the 'Cape Cod'-meeting [17] in 1993. It is the two dimensional analog of the benchmark problem of the 'falling sphere in a tube' problem, but it has the advantage of having the possibility of measuring the stress distribution around the cylinder with birefringence.

Complex flows can not only be used to test constitutive equations, but also to improve the choice of the model parameters. Usually parameters are determined using *viscometric flows* (i.e. simple shear) or *elongational flows*, where the kinematics are (partially) known

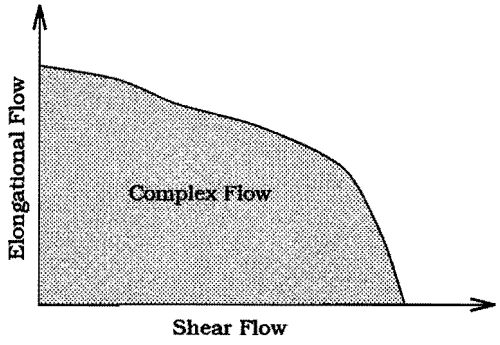

Figure 1.1: *Schematic classification of flows: horizontal axis refers to simple shear flows, vertical axis refers to the elongational flows. Complex flows have a combination of both types of deformation.*

a priori and the stress is measured. The rheology of the fluids are then characterized by (scalar) material functions, which can be used to fit model parameters of the constitutive equations. It has been found, however, that measurements in elongational flows often are impossible, unreliable or can only be obtained in a very small flow regime (e.g. Walters [112]). On the other hand, using information of shear flows only does not imply accurate, quantitative predictions in complex flows, i.e. multidimensional flows with mixed shear and elongational behavior (Armstrong et al. [4]). Despite many efforts to improve the elongational measurements (Walters [112]), it still can be doubted that behavior in complex flows is fully captured. Figure 1.1 illustrates that shear and elongational flows are only two limits of a general type of flow with mixed shear/elongational deformation. Moreover, the strain history is missing in this oversimplifying picture.

Since the complex flow involves mixed shear/elongational behavior, evaluation of constitutive equations in complex flows can give more reliable model parameters and distinguish better between the adequacy of the different constitutive equations, than can (at least) the viscometric flows [1]. Moreover, no a priori assumptions are made concerning the kinematics, which is subject of criticism in elongational flow experiments. Instead, both the velocity and stress field are measured and computed. The choice for viscometric flows by the early rheologists was deliberately made to be sure the *fluid* properties and not *flow* properties are measured. Nowadays, it is recognized that viscometric flows do not contain enough information to capture all necessary fluid parameters: the identificability is not sufficient (compare the conclusions of Oomens and coworkers ([51], [89] and [110]) on the identificability of inhomogeneous, anisotropic solid materials).

The disadvantage of this strategy is that the comparison between computations and experiments will not only be influenced by the accuracy of the constitutive equation, but

[1] It is emphasized that agreement with material functions in simple shear or elongational flows must be retained. However, usually the parameter fits are not unique and some other choice may be adequate too.

also by the accuracy of the numerical method. However, recent progress on numerical methods for viscoelastic flows has shown that reliable computations are possible (see Brown and McKinley [17]). Nevertheless it requires a constant attention.

In viscoelastic flows the dimensionless Deborah number is central: it characterizes the importance of elasticity in the flow. The number is defined by the ratio $De = \frac{\lambda_f}{\lambda_p}$, where λ_f is the characteristic time of the fluid and λ_p the characteristic process time. A typical range for practical flows of polymeric materials is $1 < De < 100$. In the past, numerical computations failed to converge at Deborah numbers of order unity. Recent developed numerical techniques have shifted this limit to higher values of the Deborah number, typically of ≈ 2 for the upper convected Maxwell model (for the benchmark problem of a sphere falling in a tube, see next section) and higher for more realistic models.

The ideal numerical simulation for practical purposes must be accurate, fast, stable, robust and capable of dealing with three-dimensional, time-dependent and non-isothermal flow conditions at high Deborah numbers. Such simulation can not be made presently. Most published studies on numerical simulations of viscoelastic flows deals with isothermal, stationary, two dimensional flow (planar or axisymmetric). In the present study only planar flows are considered. Extensions towards non-isothermal flows have been made in literature (e.g. Baloch et al. [10], Baaijens [8]). Time-dependent computations in two-dimensional problems have been reported by for example Baaijens [6] and Olsson [88]. Three-dimensional viscoelastic computations are presently hindered by the tremendous computer facilities that are required.

Confrontation of computations of the complex flow field with experiments can be achieved with:

global data: parameters like 'vortex size', 'reattachment length', 'entry pressure' (all used in 4:1 contractions), a pressure drop, or a 'friction coefficient' (often used in experiments with spheres falling in a circular tube). Such methods are often used and require no advanced experimental facilities. However, data of this kind can be rather misleading, because they need not reflect all relevant flow phenomena, nor need they be sensitive for the precise form of the constitutive equation in viscoelastic computations.

fieldwise data: flow visualization methods as streakline photography (visualizing the streamfunction in steady flows), birefringence patterns (visualizing the stress field), or deformation patterns.

pointwise data: *pointwise* measured stress and velocity fields: variables in the viscoelastic computations.

The latter type of data contains the most information, and is, therefore, preferred in the present study. To achieve a quantitative, accurate comparison with experiments, measurement techniques that can map both the velocity field and the stress field with sufficient resolution are needed. Laser Doppler anemometry (LDA) enables pointwise velocity measurements, as demonstrated for polymer solutions by for example the MIT group of

Armstrong and Brown (McKinley [80], Quinzani [93], Quinzani et al. [94], Raiford et al. [95]). The flow induced birefringence (FIB) technique for pointwise stress measurements in planar flows, developed by Fuller and Mikkelsen [38], completes the experimental tools that are required.

In the sequence of this chapter, first the equations that govern viscoelastic flows are described in Section 1.2. Then a compact literature survey is given of work on the evaluation of constitutive equations in complex flows of viscoelastic fluids and a review of studies of viscoelastic flows past cylinders (Section 1.4). Finally, Section 1.5 contains the objectives and the outline of this thesis.

1.2 Isothermal flow of incompressible, viscoelastic fluids

Isothermal flow of incompressible fluids is described by the equations for conservation of and momentum (neglecting gravity and body forces) and mass:

$$\rho(\frac{\partial \vec{v}}{\partial t} + \vec{v} \cdot \nabla \vec{v}) - \vec{\nabla} \cdot \boldsymbol{\sigma} = \vec{0} \tag{1.1}$$

$$\vec{\nabla} \cdot \vec{v} = 0. \tag{1.2}$$

where $\vec{v}$ denotes the velocity field, ρ is the density and $\boldsymbol{\sigma}$ the Cauchy stress tensor, defined by

$$\boldsymbol{\sigma} = -p\boldsymbol{I} + \boldsymbol{\tau} \tag{1.3}$$

where $p(\vec{x}, t)$ is the pressure field, and $\boldsymbol{I}$ the unity tensor. The problem is defined completely when an appropriate constitutive equation is substituted for the extra-stress field $\boldsymbol{\tau}$. For Newtonian fluids the relation

$$\boldsymbol{\tau} = 2\eta \boldsymbol{D} \tag{1.4}$$

holds, with $\boldsymbol{D}$, the rate-of-deformation tensor $2\boldsymbol{D} = \boldsymbol{L} + \boldsymbol{L}^T, \boldsymbol{L} = (\vec{\nabla}\vec{v})^T$. Substitution of this simple constitutive equation in Equation 1.1 yields the *Navier-Stokes* equations.

Polymeric materials (solutions, melts, dispersions) have in general non-Newtonian flow behavior (see for example Tanner [106]) and require, therefore, more complicated constitutive equations. As stated already in the introductory Section (1.1), the search for appropriate constitutive equations for polymeric fluids is a major research challenge for rheologists. A detailed discussion of the models that have been proposed in the past can be found in the books of, for example, Bird et al. [13], Larson [70] or Tanner [106]. Generalized Newtonian models are the most simple class of non-Newtonian models. These models have a time-independent viscosity that depends on the second invariant of $\boldsymbol{D}$, II_D:

$$\boldsymbol{\tau} = 2\eta(II_D)\boldsymbol{D} \tag{1.5}$$

with

$$II_D = 2\boldsymbol{D} : \boldsymbol{D}. \tag{1.6}$$

In simple shear flow the shear rate $\dot{\gamma}$ equals $\sqrt{II_D}$. Many models have been proposed for $\eta(II_D)$. A generalized Newtonian model only describes the shear rate dependence of the viscosity; neither normal stresses in shear flows nor any other non-Newtonian effect are included.

Non-linear viscoelastic constitutive models attempt to model the rheological behavior of viscoelastic fluids in any flow. Two types of constitutive equations exist: equations of the integral type and of the differential type. In this thesis, only those constitutive equations of the differential type are considered that have the general form:

$$\overset{\square}{\boldsymbol{\tau}}_i + \frac{1}{\lambda_i}\boldsymbol{Y}_i \cdot \boldsymbol{\tau}_i = \frac{2\eta_i}{\lambda_i}\boldsymbol{D} \qquad i = 1, \ldots, N. \tag{1.7}$$

with

$$\overset{\square}{\boldsymbol{\tau}}_i = \frac{\partial \boldsymbol{\tau}_i}{\partial t} + \vec{u} \cdot \vec{\nabla}\boldsymbol{\tau}_i - (\boldsymbol{L} - \xi \boldsymbol{D}) \cdot \boldsymbol{\tau}_i - \boldsymbol{\tau}_i \cdot (\boldsymbol{L} - \xi \boldsymbol{D})^T \tag{1.8}$$

where i is the index for each mode and the tensor function $\boldsymbol{Y}$ is defined for some models in table 1.1. Note that the PTT and Giesekus equations have a non-linear term for τ_i through their function $\boldsymbol{Y}_i$. The UCM model is a special case of both of these models when the parameters ϵ and ξ (in the PTT models) or α (in the Giesekus model) are zero. Many other models can be found in for example Larson [70]. When $\xi = 0$ the (Gordon-

Constitutive equation	Y_i	ξ
PTT-a	$e^{\frac{\epsilon_i \lambda_i}{\eta_i}\mathrm{tr}(\boldsymbol{\tau}_i)}\boldsymbol{I}$	$-1 < \xi < 1$
PTT-b	$(1 + \frac{\epsilon_i \lambda_i}{\eta_i}\mathrm{tr}(\boldsymbol{\tau}_i))\boldsymbol{I}$	$-1 < \xi < 1$
Giesekus	$(\boldsymbol{I} + \frac{\alpha_i \lambda_i}{\eta_i}\boldsymbol{\tau}_i)$	0
UCM	$\boldsymbol{I}$	0

Table 1.1: *Definition Y_i and ξ in Equation 1.7, specifying several constitutive equations of the differential type. PTT= Phan-Thien Tanner , UCM= upper convected Maxwell.*

Showalter) convected derivative $\square$ is usually denoted as ∇, the upper convected derivative. The subscript i denotes a single mode. Often, a Newtonian ('solvent') term $2\eta_s\boldsymbol{D}$ is added to the viscoelastic extra stress tensor, and the total extra-stress tensor for a model with N modes is then found from

$$\boldsymbol{\tau} = 2\eta_s\boldsymbol{D} + \sum_i^N \boldsymbol{\tau}_i. \tag{1.9}$$

The PTT-a model is more suitable for polymer melts than the PTT-b model, because of its characteristic elongation rate dependence of the elongational viscosity. The PTT-a model predicts an elongational viscosity that is elongational thickening at lower elongation rates, reaches a maximum and then becomes elongational thinning at higher elongational rates. In case of the PTT-b model the elongational viscosity goes to a plateau at higher elongation rates. The first type of behavior agrees with the results of e.g. Laun [71] for LDPE melts.

Dimensionless numbers Dimensionless numbers are helpful to characterize flows. In the flows considered in this study the Deborah number and the Reynolds number are of importance.

The Deborah number evokes from non-dimensionalizing viscoelastic constitutive equations. In general two expressions for the Deborah number are found in literature:

$$De_1 = \lambda_f \dot{\gamma}_c \tag{1.10}$$

where λ_f is a characteristic relaxation time of the fluid (in this thesis the average Maxwell time is used defined in Equation 3.8 and $\dot{\gamma}_c$ is a characteristic shear rate. Another definition is

$$De_2 = \lambda_c(\dot{\gamma}_c)\dot{\gamma}_c, \tag{1.11}$$

with $\lambda_c(\dot{\gamma}_c) = \psi_1(\dot{\gamma}_c)/(2\eta(\dot{\gamma}_c))$, a shear rate dependent characteristic time constant. In literature, not all authors use the same definition for De, and therefore care should be taken when comparing results of different studies. The cited De numbers are denoted with De_1 when it is of the same type as Equation 1.10 and with De_2 when it is defined according with Equation 1.11. In this thesis the definition of De_1 is used because of its simplicity. Moreover, Boger et al. ([16]) advocate this definition instead of De_2. They argue that the latter definition does not reflect viscoelastic behavior that is often dominated by elongational properties, but merely the non-linear shear properties, because it leads to a Deborah number that has an asymptotic bound in elongational flows with increasing flow rate.

The Reynolds number Re_1 is defined as

$$Re_1 = Ud\rho/\eta_0 \tag{1.12}$$

with U a characteristic velocity of the flow, d a characteristic length of the geometry, ρ the density of the liquid, and η_0 the zero-shear viscosity.

Similar to De_2, also a definition of the Reynolds number can be made with a variable viscosity, Re_2 :

$$Re_2 = Ud\rho/\eta(\frac{U}{d}). \tag{1.13}$$

The first definition is adhered to in this thesis. The interpretation of the Reynolds number is not as straightforward as in the case of a Newtonian fluid, where it evokes by non-dimensionalizing the balance equation of momentum and represents the relative importance of inertia forces to viscous forces. In case of non-Newtonian fluids, it is not generally true that inertia terms can be neglected when $Re << 1$, because very different values can be present in different regions of a flow (see for example the discussion in Hulsen [55], p. 24).

1.3 A literature survey on combined experimental - numerical studies of viscoelastic complex flow fields

Several complex flows have been used to compare experiments with numerical simulations of viscoelastic polymer melts and solutions:

contraction flows: abrupt entry and exit flows, tapered dies;

flows with stagnation points: in particular planar flow past a confined cylinder, axisymmetric flow past a sphere falling in a tube and unbounded flow past an infinite cylinder or past a sphere;

flow between two rotating eccentric cylinders: the 'journal bearing';

and to a lesser extent free surface flows (e.g. 'die swell') and the 'wavy wall channel'. The contraction flows have received far most interest, and for reviews it is referred to Boger [14] and to Quinzani [93]. In this section, first an overview is given of work that combines experimental observations with computations of the complex flow field using viscoelastic constitutive equations. After that, a more detailed review is given for the stagnation flow past spherical objects, in particular for the planar flow past a cylinder.

In table 1.3 an incomplete list is shown of relevant, mostly recent, studies that have analyzed experimentally complex flows of viscoelastic polymeric fluids by means of a comparison of measurements of velocity and/or stress field with computed results. It appears that in case of polymer solutions the streakline photography and LDA measurements are the most commonly used experimental methods. The fact that only in a few cases birefringence measurements have been used is due to the low birefringence level in flows of solutions which makes fieldwise birefringence measurements impossible. An advanced experimental apparatus like the Rheo Optical Analyzer (ROA), developed by Fuller and Mikkelsen [38], is required instead. The use of such systems is not widespread yet.

In case of polymer melts, streakline photography and fieldwise birefringence are the most commonly used experimental methods. Both methods are relatively easy to use. Fieldwise birefringence studies are usually presented by means of birefringence patterns. Only Han and Drexler ([46],[48], [47]) used the (tedious) method of constructing off-axis stress patterns from fieldwise birefringence measurements. The work of Han and Drexler is classical, since they first measured both the velocity (from short-time streak photographs) and stress fields (constructed from birefringence patterns) experimentally in a complex flow. The lack of computational tools at that time prevented a comparison with viscoelastic computations.

A direct way to evaluate constitutive equations is integration of the constitutive equations along a particle path where the kinematics are known (from LDA) and comparing the results with measured stresses. Mostly, this has been done along lines of symmetry so only one velocity component needs to be measured and stresses can be calculated easily

Reference	Year	Geometry	Fluid	Exp. meth.	Comp. meth.	De_{max}
Solutions						
Raiford [95]	89	A4:1	PIB/C14	LDA	FEM-gn	61
Georgiou [43]	91	PPAC	XG, PAC	SP	FEM	1.29
Armstrong [4], [94]	92	P4:1	PIB/C14	LDA, FIB-p	IPP	4.15
Dhahir [112]	92	PPC	XG,PAC	SP	FEM	0.04
Rajagoplan [96]	92	EC	PS/TCP	FIB-p	FEM	1.40
Davidson [27],[28]	94	PWWC	PS/TCP	LDA, FIB-p	FEM, IPP	0.52
Becker [11]	94	FB	PIB/PB/C14	TSV	FEM	3.40
Melts						
Han [46],[48],[47]	73	P11:1	PP,HDPE,PS	SP, FIB-f	SOF	?
Isayev [58]	85	EF	PIB	FIB-f	FEM	19.1
Aldhouse [3], [76]	86	EF	HDPE	LDA,FIB-f	IPP	283
White [114],[115]	88	P4:1,P8:1	LDPE,PS	SP,FIB-f	FEM	7.6
Maders [77]	92	P3.5:1	LDPE	FIB-f	FEM	30.4
Galante [41]	93	4:1	PDMS	FIB-p	SOF	30
Kiriakidis [64]	93	P8:1	LLDPE	FIB-f	FEM	14.7
Kajiwara [62]	93	EF	LDPE	FIB-f	FEM	2.3

Table 1.2: *Studies that have analyzed complex flows of polymeric fluids by comparing measurements of the velocity and/or stress field(s) with computed results. De_{max}= maximum Deborah number (De defined in Equation 1.10, with $\dot{\gamma}_c = U/h$ (U = mean velocity , h=half height of downstream channel in contraction flows or radius cylinder in flows past cylinders)). (P,A)4:1 = planar, axisymmetric abrupt four-to-one contraction, PWWC= planar flow in a wavy walled channel, PPAC= planar flow past an array of cylinders, PPC= planar flow past cylinder, EC=two eccentric rotating cylinders, FB= falling ball in a circular tube, EF= (several) entry flow(s), PIB=polyisobutylene, C14=tetradecane, PS=polystyrene, TCP=tricresylphosphate, XG=aqueous solution of xanthan gum, PAC=aqueous polyacrylamide solution, PB=polybutene oil, PP=polypropylene, HDPE=high density polyethylene, (L)LDPE= (linear) low density polyethylene, PDMS=polydimethylsiloxane, LDA= laser Doppler anemometry, FIB-(p,f)= birefringence measurements: pointwise/fieldwise, SP= streakline photography, TSV=transient sphere velocity, FEM= finite element computations of the flow using viscoelastic constitutive equations, FEM-gn= FEM computations with generalized Newtonian model, IPP= integration of constitutive equation along particle path using measured velocity data, SOF= solution for second order fluid theory.*

from measured birefringence data (since the optical orientation is then known a priori). Armstrong et al. [4], who used a pointwise birefringence technique, tested in this way several constitutive equations and adapted model parameters to obtain the optimal fit. The agreement was reasonable. Fairly good agreement was found by Aldhouse et al. [3] (who, in fact, presented the birefringence instead of stresses).

Qualitative fieldwise agreement between experiments and viscoelastic FEM simulations was found in case of most references in table 1.3 that used FEM. Quantitative reasonable agreement was found by Rajagopalan et al. [96], who compared pointwise stress measurements, at most positions. However, agreement was lost on positions where relaxation of elongational stresses occurred, i.e. just after the gap between the two rotating cylinders. Kiriakidis et al. [64] found fairly good quantitative agreement for the stresses along the centerline of a contraction flow of a LLDPE melt. However, the stress relaxation in the die after the contraction was under-estimated by the computations. In general, agreement becomes less good with increasing Deborah numbers.

Combined pointwise stress and velocity measurements are rare, and in the above list (which is incomplete) only two such studies are mentioned, both for polymer solutions: Armstrong et al. [4] (which is based on the work of Quinzani [93],[94]) and Davidson et al. ([27], [28]). Only in the latter study also fieldwise, finite element computations were performed, although these were mostly Newtonian.

Most studies do not investigate the sensitivity of their computed results for the choice of constitutive models. Of those listed in table 1.3 only Armstrong et al., Rajagopalan et al. and Kajiwara et al. used more than one constitutive equation. Out of six models, Armstrong et al. found the PTT model to predict centerline stresses closest to measured stresses, and Rajagopalan et al. showed that a single mode Giesekus model was inferior to a four mode fit. The computed stress fields of Kajiwara et al., who measured birefringence patterns in entry flow in a tapered die, were only weakly sensitive for the two constitutive models used (PTT and Giesekus).

The studies of Raiford [95] and McKinley et al. ([80], [83], [82]) mapped pointwise with LDA the velocity field in complex flows of polymer *solutions* with elastic instabilities. McKinley et al. studied experimentally elastic instabilities in planar flow past a cylinder and the flow through an axisymmetrical contraction for a PIB/PB/C14 Boger fluid [2]. They showed the power of LDA and observed, for example, that under steady inflow conditions in the axisymmetric contraction a clear time-dependent flow became present at a certain flow rate in the LDA velocity signal, while the time-averaged streakline photographs indicated no change in the (apparent steady) flow field. Observations on elastic instabilities have also been reported by Chmielewski and Jayaraman [24], who studied with streak photography and LDA the cross flow of the M1 (PIB/K/C14) (K=kerosene) Boger fluid and the A1 (PIB/Decalin) shear thinning fluid through hexagonal and square arrays of cylinders.

[2] 'Boger' fluids are a special class of viscoelastic model fluids, introduced by Boger (e.g. [12]), that have a constant shear viscosity and a nearly quadratic dependence of the first normal stress difference on shear rate, like predicted by the UCM model.

To the authors knowledge, the stagnation flow of a polymer *melt* past circular objects has not been studied in detail yet [3]. In case of polymer solutions, there has also been no detailed pointwise, quantitative comparison of measured velocity and stress fields with FEM computations. The work of Georgiou et al. [43] merely focussed on the experimental observation of instability phenomena that are beyond the capability of current finite element methods. Dhahir and Walters showed only some tentative computational results of streamline patterns that did not have the same trends as the experiments.

Stagnation flows past circular bodies have two important characteristics: (i) material elements that move near the line of symmetry have a history of deformation with subsequently strong compression, high shearing and strong extension, and (ii) no corner singularities exist, like those that complicate numerical analysis of entry flows. This makes these flows good candidates for testing constitutive equations. The literature on complex flows past circular objects will be discussed next.

1.4 Viscoelastic flow past cylinders

Viscous flows past circular objects is a classical topic in Newtonian fluid mechanics, in particular at high Reynolds numbers where the Von-Karman vortex street is observed. These types of flows are beyond the scope of the present study. In the following, the Reynolds number is typically $\ll 1$, unless otherwise noted explicitly. Furthermore, attention will be focussed on planar flows, since these will be used in this study.

In literature, it is found for polymer solutions that the effect of viscoelasticity on the velocity field is influenced by (i) the position of the constraining walls, (ii) by the degree of elasticity in the flow (characterized by the Deborah number) and (iii) by the relative importance of inertia (characterized by the Reynolds number).

In case of the *unbounded* flow past a cylinder (in an uniform stream, i.e. with an uniform velocity field far away of the cylinder) experiments gave, as could be expected, only a small effect on the streamline pattern (Manero and Mena [78], Mena and Caswell [86], Ultman and Denn [109]). The results seemed contradictory: the streamlines shifted either a little upstream or downstream of the cylinder. From their experimental results, Manero and Mena [78] suggested that the direction depends on the value of the De number: a downstream shift at low elasticity ($De < 1$) and an upstream shift at high elasticity ($De > 1$) .

Several full numerical studies solving the planar flow past a cylinder in an uniform stream have been reported. Pilate and Crochet [92] applied a second order fluid model at low to moderate Deborah numbers ($0 < De < 1$) and low to high Reynolds numbers ($0.1 < Re < 100$). Townsend [108] considered two Oldroyd models (one representing a constant viscosity, elastic fluid, and one representing a viscoelastic fluid with shear thinning) at low Deborah numbers. Both studies revealed a small downstream displacement of the streamlines as observed experimentally by Manero and Mena [78]. Chilcott and Rallison

[3] Chilcott and Rallison [23] mentioned that Mead [84] had performed such experiments; however, his thesis proved to be not available anymore.

[23] used a constant-viscosity, elastic model (FENE-P) at zero Reynolds number and high Deborah number ($De = 8$). They did not report results of the streamline pattern.

The flow past a *symmetrically confined* cylinder has not been studied extensively yet. Dhahir and Walters [30] reported some experiments and calculations, but focused merely on the eccentric case which will be discussed below. McKinley [80] reported unique LDA measurements of the flow past a symmetrically confined cylinder of an organic Boger fluid. His observations alluded different flow regimes with a transition from steady two dimensional flow to a steady three dimensional, spatially-periodic cellular structure. The observed patterns were characterized as flow instabilities, which made numerical simulations impossible. The point past the cylinder where centerline axial velocity profiles reach fully developed flow shifted progressively downstream with increasing Deborah number until the flow instability occurred. Stress measurements using a FIB technique appeared to be impossible for this fluid (McKinley [81], for unknown reasons the laser beam was deflected in a peculiar way).

On the other hand, the related problem of a *falling sphere* along the centerline of a cylindrical tube has been studied rather intensively, both numerically and experimentally. In Newtonian fluid mechanics this flow is used to measure the viscosity of the fluid ('falling ball viscometer') by measuring the settling velocity of the ball. In non-Newtonian fluid mechanics attempts are made to use the transient motion of the falling ball as a measure for the rheological behavior of viscoelastic fluids in a non-homogeneous flow (e.g. Becker et al. [11]). The flow is also popular as a test problem for numerical techniques (e.g. Debae et al. [29], Lunsmann et al. [74], Zheng and Phan-Thien [117], Zheng [118]), after it was set as a benchmark problem (Hassager [49]). At the 'Cape Cod'-meeting (Brown and McKinley [17]) in 1993, the numericists showed with this problem that important progress has been made with respect to the numerical techniques for viscoelastic flow simulations. The drag coefficient for the falling sphere in a 'UCM'-fluid could be computed by widely varying methods up to four decimals. Some studies focussed on comparing the drag coefficient of the sphere, obtained from the measured steady state velocity of the falling sphere, with model predictions as a test for constitutive equations (e.g. Chhabra et al. [22], Mena et al. [87]). Observations of Sigli and Coutanceau [104] on the velocity field with streak-photography at low Deborah numbers around a sphere falling along the axis of a cylindrical tube filled with an aqueous polyox solution, showed that the wall proximity (expressed by the ratio sphere diameter - cylinder diameter) increased the effects due to the fluids elastic behavior: a steeper rise of the axial velocity profile along the centerline downstream of the sphere, together with an increase of the overshoot of that velocity. Zheng et al. [118] analyzed numerically the effects of inertia (Newtonian model), shear-thinning (Carreau model) and elasticity (PTT-b model) in the flow past a sphere in a cylindrical tube. They found also a similar effect on the axial velocity at the centerline downstream of the sphere, in contradiction with their previous result for the Maxwell model where a slower rise was found. They concluded that the direction of this shift depends on the exact form of the constitutive equation, and suggested that the effect is caused by the combined effect of shear thinning and elasticity.

In the case of the *asymmetrically confined*, cylinder the effect of viscoelasticity on the

velocity field is more pronounced which is explained by the influence of the stresses on the kinematics. This has been demonstrated experimentally by Walters and co-workers ([25], [61], [30], [43]). Cochrane et al [25] observed that the streaklines for a viscoelastic fluid were much more sensitive for a small asymmetry in the constraining of the cylinder then for a purely viscous fluid. Dhahir and Walters [30] visualized streamlines for the planar flow past an eccentric confined cylinder and observed that for a (elongational thickening) viscoelastic liquid more material flows through the broader gap compared with a Newtonian liquid. Jones and Walters [61] and Georgiou et al. [43] found the same effect in the flow of several types of liquids through an anti-symmetric array of confined cylinders. It is considered as a manifestation of the extensional viscosity: molecules entering the narrow gap must elongate more strongly than those entering the broad gap, which results in a locally higher flow resistance in the narrow gap. Interestingly, Olsson [88] simulated with the Giesekus model the start-up of flow past a cylinder that is located near one on the walls. He found unstable behavior of the fluid, that was more pronounced if the velocity was increased and/or the velocity rise time was shortened.

In this context, the work of Joseph et al. [72] is of interest, who performed experiments with spheres rolling in a viscoelastic fluid down an inclined wall. They observed that the sense of the rotation is in the other direction compared with a sphere rolling down an inclined plane in a Newtonian fluid (in which case it rotates like in air). Moreover, if a sphere was dropped on a small distance from a vertical wall in a viscoelastic fluid, the sphere moved to the wall and rotated in the 'counter' sense. If the same sphere was dropped in a Newtonian fluid, it moved away from the wall. These effects can be explained with the competition of inertia and viscoelasticity and is also more pronounced as the velocity of the sphere and thus the Deborah number is increased (for example by a larger inclination angle of the wall): the polymer molecules are reluctant to flow through the narrow gap between sphere and wall. The net force on the sphere causes it counter rotation compared with a Newtonian fluid.

1.5 Objectives and outline of this thesis

Since experimental observation of complex flows is the starting point of any improvement of constitutive equations, numerical simulations must be confronted with the results of a careful experimentally mapped, if possible, velocity and stress field. A rigorous comparison should be based on fieldwise, spatially resolved, quantitative data. The complex flows of polymer solutions and melts past a confined cylinder will be used to achieve these objectives. This problem is recommended as a benchmark problem for viscoelastic flow studies (Brown and McKinley [17]).

Several features make this type of complex flow geometry interesting. First, it has received far less interest than contraction flows. In particular, a detailed quantitative mapping of the stress and velocity field and a comparison with numerical simulation does not exist yet. Most studies act as tests of numerical codes, and the comparison with experiments is only qualitative or restricted to a single overall parameter as a drag coefficient.

Second, finite element computations are presently only feasible in two-dimensional flows. Planar flows have the advantage compared with axisymmetric flows, that stresses can be measured with birefringence techniques. In non-planar flows the interpretation of birefringence measurements in terms of stresses is far more complex if not impossible.

Third, the flow past a submerged circular object differs in a fundamental way from the, almost classical, 4 : 1 contraction flow. On the surface of the cylinder two stagnation points exist: one at the front where the material is compressed, and one at the aft, where the material is stretched after being sheared along the side of the surface of the object (e.g. Becker et al. [11], Chilcott and Rallison [23]). Polymer molecules in the vicinity of the cylinder will have large residence times, which will result in large molecular extensions and elastic stresses. Compared with the contraction flows, elongation rates are expected to be much higher since the material is accelerated from rest in the rear stagnation point. This complex flow field is expected to contain relevant information for testing constitutive equations.

Fourth, numerical simulations of abrupt contraction flows suffer from the complication of the presence of singular re-entry corner points. Such difficulties are absent in the flow past a cylinder, which is expected to facilitate the computations.

In the experiments the cylinder will be confined, since it has been observed that the effect of viscoelasticity on the velocity field is influenced by the relative position of the cylinder to the confining plates (see Dhahir and Walters [30]).

Velocities will be measured pointwise with laser Doppler anemometry (LDA), and stresses with a flow induced birefringence (FIB) technique. Only a few studies have used these two methods simultaneously (Armstrong et al. [4], Davidson et al. [28]). A 5%(w/w) polyisobutylene in tetradecane solution will be used as model fluif to enable a comparison with the study of Armstrong et al. [4]. They used also both LDA and FIB to analyze the flow of the same fluid in a four to one contraction. The fluid is viscoelastic and shear thinning, which behavior is preferred (instead of the (constant viscosity) elastic Boger liquids frequently used) when aiming at making progress towards 'melt-like' behavior (Brown and McKinley [17]). Polymer solutions are used as model fluids for melts to facilitate the analysis in both experimental and computational respect. Experimentally, polymer melts require high temperatures ($150 - 300\,^{\circ}C$), and problems can arise with temperature inhomogeneities due to viscous heating. This can disturb the optical measurements, for example by deflection of the laser beams due to refractive index differences. Also, the relatively low velocity range ($\leq 1\,cm/s$) in flows of polymer melts demands a LDA system capable of measuring the low frequencies of the Doppler bursts. Computationally, polymer melts require a broad spectrum of relaxation times with typically a large characteristic relaxation time ($\mathcal{O}(1)\,s$), and high extensional stresses. This all together severely hampers numerical simulations. Nevertheless, some preliminary results for a LDPE melt will be presented too.

Experimental methods used in the complex flow studies in Chapters 4 and 5 are described in detail in Chapter 2. Numerical methods are discussed shortly in Chapters 4 and 5. For details about these techniques it is referred to literature. Chapter 3 contains the rheological characterization in simple shear of the materials studied. These data are used

to fit constitutive equations that are applied in the computations of the complex flows. The Phan-Thien Tanner and Giesekus equation are fitted in a single and a four mode version. In Chapter 4, comparisons are made of velocity and stress measurements with numerical simulations for the flow past a cylinder for two model fluids (polyisobutylene in tetradecane solutions). In Chapter 5 the flow past a cylinder is analyzed in case of the LDPE melt, by comparing measured birefringence patterns with computed results. Finally, in Chapter 6 conclusions are made and a general discussion is given. In the present study, the ultimate aim of using experimental data in complex flows to adjust model parameters or to extend the constitutive models has not been reached yet. In case of the polymer solutions, the level of agreement between experiments and simulations was too satisfactory to perform such procedure. In case of the polymer melt, the numerical simulations were too time-consuming to attempt to improve the agreement by an iterative sequence of simulations for varying model parameters. Moreover, differences between computations and experiment are that large that it seems more meaningful to modify the models itself instead of making a parameter adjustment.

Chapter 2

Experimental methods and equipment

2.1 Introduction

As made clear in the introductory chapter, two different optical techniques have been used: laser Doppler anemometry (LDA) for velocity measurements, and flow induced birefringence techniques (FIB) for stress measurements. A basic introduction of the theory in optics can be found in for example Hecht and Zajac [50]. A profound monograph of electromagnetism is found in Jackson [59] (the fundamental equations that describe the propagation of electromagnetic waves are recapitulated in Appendix A). Propagation of polarized light through optical elements is treated in detail in Azzam and Bashara [5] (Appendix B contains a summary).

The principles of the LDA technique and the equipment used are summarized in Section 2.2. The theory of the FIB measurements and the equipment used are described in Section 2.3. In Section 2.4, limitations of the methods used and some alternative techniques are discussed.

2.2 Laser Doppler anemometry

2.2.1 Introduction

Fluid velocities can be measured accurately with high spatial resolution by means of the laser Doppler anemometry technique ([33]). This technique is based on the observation that the frequency of the light scattered by a moving particle depends on its velocity. The most commonly used measurement systems are the reference beam technique and the differential Doppler or dual beam technique. The differential Doppler technique, which uses two crossing laser beams of equal intensity, was used in the present study.

2.2.2 The differential Doppler technique

Doppler shift on scattering

The fundamental physical phenomenon in laser Doppler anemometry is the frequency shift of light that is scattered by moving small particles. This frequency shift, the Doppler shift, is proportional to the velocity of the particles. This will be shown below.

Consider a particle located at position $\vec{x}(t)$ (relative to an axis frame with its origin in the measurement volume) that scatters the light from an incident illuminating uniform plane wave that is linearly polarized, as described by Equation A.9. For an observer at position $\vec{r}$, the scattered light wave is a spherical wave, provided the distance $r(= |\vec{r}|)$ to the observer is much larger than both the wavelength of the light λ_0 and the mean diameter of the scattering particle (Kerker [63]):

$$\vec{E_s} = \frac{\sigma \vec{E_i}}{k|\vec{r} - \vec{x}|} e^{-ik|\vec{r}-\vec{x}|}, \tag{2.1}$$

where σ is the (complex) scattering coefficient that is a function of the scattering angle, the phase shift and of the polarization of the scattered wave relative to the illuminating wave $\vec{E_i}$.

Since the illuminated, scattering region (the measuring volume) is very small $|\vec{x}| \ll |\vec{r}|$, and $|\vec{r} - \vec{x}| \cong r - \vec{x} \cdot \vec{e_r}$, Equation 2.1 can be rewritten to (after substitution of Equation A.9 and replacing the frequency ω of the incident wave by ω_0)

$$\vec{E_s} = \frac{\sigma \vec{E_0}}{kr} e^{i(\omega_0 t - kr + k\vec{x}\cdot(\vec{e_r} - \vec{e_k}))}. \tag{2.2}$$

The factor $\vec{x} \cdot \vec{e_r}$ is neglected in the denominator, while it must be retained in the phase. The instantaneous frequency of (nearly) harmonic signals is the time derivative of their phase (which is the argument of the exponential in Equation 2.2). With $\vec{u}(t)$ denoting the velocity of the particle and using Equation A.9, the angular frequency from Equation 2.2 is written as

$$\omega_s = \omega_0 + k\vec{u}(t) \cdot (\vec{e_r} - \vec{e_k}), \tag{2.3}$$

or in units of frequency ([Hertz])

$$\nu_s = \nu_0 + \frac{\vec{u}(t) \cdot (\vec{e_r} - \vec{e_k})}{\lambda}. \tag{2.4}$$

The Doppler shift of the scattered light is the result of summing a frequency shift associated with the velocity component of the particle in the opposite direction of the wave vector of the incident wave $(= -\vec{u} \cdot \vec{e_k})$, and the velocity component towards the observer at $\vec{r}$ $(= \vec{u} \cdot \vec{e_r})$.

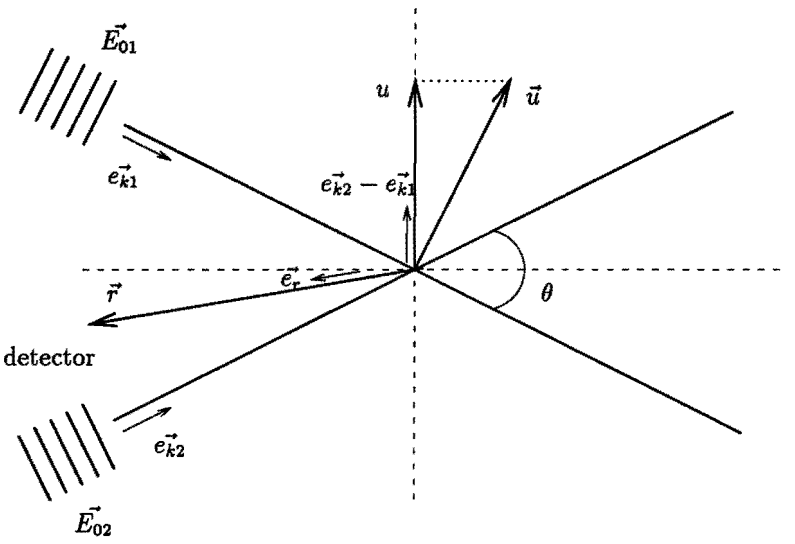

Figure 2.1: *The differential Doppler technique: moving particles with velocity $\vec{u}(t)$ scatter light when crossing the intersection of two beams of equal intensity ($\vec{E}_{01}, \vec{E}_{02}$). The velocity component normal at the bisector of the two beams (along $\vec{e}_{k1} - \vec{e}_{k2}$) is found from the frequency of the scattered light (see text).*

The differential Doppler technique

Consider two intersecting plane light waves $\vec{E}_{01}$ and $\vec{E}_{02}$ with frequencies ν_0 and $\nu_0 + \nu_{shift}$, propagating in two different directions $\vec{e}_{k1}$ and $\vec{e}_{k2}$ (Figure 2.1). The superposition to the frequency of wave $\vec{E}_{02}$ of a shift frequency ν_{shift} enables to distinguish between positive and negative velocities as will be shown below. The scattering volume is the intersection of the two focussed beams of similar intensity with inclination angle θ. The scattered light is observed in the direction of detector $\vec{e}_r$. A particle moving through the scattering volume scatters two waves ($\vec{E}_{s1}$ from $\vec{E}_{01}$ and $\vec{E}_{s2}$ from $\vec{E}_{02}$) with frequencies

$$\nu_{s1} = \nu_0 + \frac{\vec{u}(t) \cdot (\vec{e_r} - \vec{e}_{k1})}{\lambda}, \tag{2.5}$$

$$\nu_{s2} = \nu_0 + \nu_{shift} + \frac{\vec{u}(t) \cdot (\vec{e_r} - \vec{e}_{k2})}{\lambda}. \tag{2.6}$$

$$\tag{2.7}$$

The intensity of the scattered light (as function of time) is the only quantity of the scattered wave that is measured in a laser Doppler anemometry measurement. The intensity is measured with a photodetector, that can not resolve signal frequencies of the order of ν_0. Such frequencies will contribute to the stationary component of the intensity. Since the

two intersecting beams have a small frequency difference, the component of the wave that oscillates with the frequency difference ('beating' frequency)

$$\nu_{s1} - \nu_{s2} = \nu_{shift} + |\frac{\vec{u}(t) \cdot (\vec{e_{k2}} - \vec{e_{k1}})}{\lambda}|, \tag{2.8}$$

is the only component that can be resolved in time. It may be rewritten as (see Figure 2.1)

$$\nu_{s1} - \nu_{s2} = \nu_{shift} + \frac{2u}{\lambda} \sin \frac{\theta}{2}, \tag{2.9}$$

where $u = |\vec{u}| \cos \alpha$. Thus u is the velocity component normal to the bisector of the two beams. For negative velocities the frequency difference is smaller than ν_{shift}, whereas for positive velocities this difference is larger than ν_{shift}. In this way the sign of the velocities can be determined (provided that the negative velocities result in a frequency shift less than ν_{shift}).

The second term represents the frequency difference between the Doppler shifts caused by the two beams. It depends linearly on the velocity component of the scattering particle in the direction normal to the bisector of the two illuminating laser beams. It is independent of the scattering direction $\vec{e_r}$ and thus independent of the detector position. This implies that a large solid angle can be used to collect the scattered light. Only the intensity of the scattered light will be dependent on the scattering direction.

The result is that the detector generates an output signal which is linear dependent on u according to Equation 2.9. After processing of this signal the velocity of the moving particle is found.

2.2.3 Laser Doppler equipment

Figure 2.2 shows a schematic draw of the equipment used for the LDA measurements. A dual beam method was used in backscatter mode. The system, that is controlled by the Flow Velocity Analyzer (Dantec 58N20), is operated from a personal computer with the software Floware (Dantec). The incident light beams are generated by an 300 mW Argon-ion laser (Ion Laser Technology 5500A). The laser emits linearly polarized light and consists of three colors: green ($\lambda = 514.5\,nm$), blue ($\lambda = 488.0\,nm$) and cyan ($\lambda = 476.5\,nm$). In this study, the 1D configuration with only the green color has been used. A Bragg cell splits the single beam from the laser in two equally powerful beams, while the frequency of one of the beams has been shifted with a shift frequency $\nu_{shift} = 40\,MHz$. A color separator splits the colors and the two green laser beams are focussed into two separate glass fibers. Together with one fiber for the received scattered light, these fibers are bundled together and lead to the laser probe. In this probe a lens with focal length $f = 80\,mm$ focuses the two beams in the measuring volume. The backscattered light is received by the same lens that focused the intersecting beams. The received light is transmitted back through a fiber to a second color separator after which the signal is detected by the photomultiplier for green light. Here the optical signals are transformed into electrical signals, that are

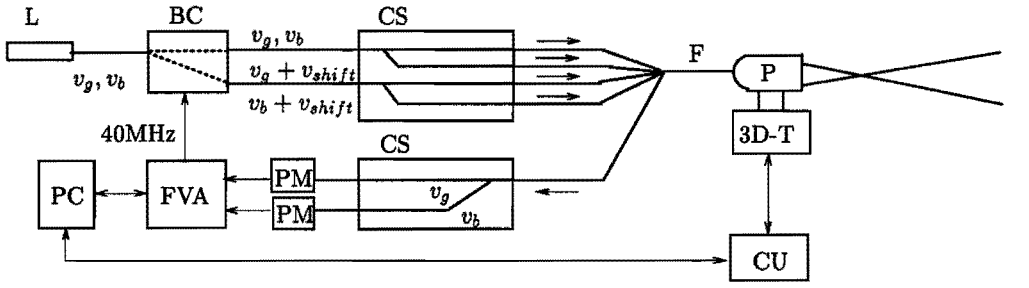

Figure 2.2: *Schematic drawing of the laser Doppler equipment. L: laser, BC: Bragg cell, CS: color separator, F: glass fiber, P: laser probe, PM: photomultiplier, FVA: Flow Velocity Analyzer, 3D-T: three axis traverse, CU: control unit for traverse, PC: personal computer, ν_g, ν_b: frequency of green and blue beams (only green used here), ν_{shift}: frequency (pre-)shift.*

processed by the Flow Velocity Analyzer. The laser probe is fixed on a XYZ-traverse (Dantec, Lightweight Traverse), that is controlled by Floware. It has a range of 540 mm along each axis, and has an accuracy of $0.05mm$.

The spatial resolution of the laser Doppler measurements is determined by the dimensions of the measuring volume. The measurement volume has an ellipsoidal shape, and its dimensions are determined by the angle θ between the two laser beams and the diameter of the laser beam in the measuring volume, provided that the waist of the beam is positioned in the measuring volume (Drain [33]). The distance between the two parallel beams emitted by the laser probe is $38\,mm$. This leads to a measuring volume with dimensions $50 \times 50 \times 200\,\mu m$.

The resolution of the velocity measurement is determined by the FVA hardware. The system has 6 different frequency ranges that can be used, all including zero. Each frequency range has 256 discrete frequency levels, or equivalently 256 discrete velocity levels. The resolution of the velocity measurement is thus 1/512 of the whole velocity range for the specific frequency band used. The smallest frequency band that can be used has a width of $0.12MHz$, and thus the smallest resolvable Doppler frequency is $0.12/512\,MHz = 234\,Hz$. In the situation above this implies a resolution of the velocity field of $0.13\,mm/s$.

2.3 Flow Induced Birefringence

2.3.1 Principle of birefringence

Consider a light wave of normal incidence at a birefringent medium. This medium has two principal directions along which the propagating light wave experiences two different refractive indices n_I and n_{II}. The first refractive index corresponds to the component of the electric field that is parallel to the optic axis (the 'extra-ordinary' ray), and the second

refractive index corresponds to a component of the electric field vector perpendicular to the optic axis (the 'ordinary ray'). This optical anisotropy is described by a refractive index tensor $\boldsymbol{n}$. In the simple (but common) case with both principle directions of the birefringence perpendicular to the propagation vector, this tensor is relative to a Cartesian principle frame given by

$$\boldsymbol{n} = \begin{bmatrix} n_I & 0 & 0 \\ 0 & n_{II} & 0 \\ 0 & 0 & n_{II} \end{bmatrix}. \tag{2.10}$$

where n_I corresponds to an electrical field vector polarized parallel to the optic axis and n_{II} to an electric field vector polarized perpendicular to the optic axis.

The single incident wave splits in the birefringent medium in two waves whose electric field vectors are mutually orthogonally polarized and that have each a different velocity. Since both principle directions of the refractive index tensor are perpendicular to the propagation direction of the incident wave, these two waves are coincident in space. The electric field component of the incident wave that has its electric field vector parallel to the optic axis propagates through the birefringent medium with a velocity $v_1 = \frac{c}{n_I}$, while the other component has a velocity $v_2 = \frac{c}{n_{II}}$. On exit of the birefringent medium, the two waves will have different phases: the slower wave lags the faster wave. When the birefringence is homogeneous along the wave propagation direction, the phase retardance δ is related to the principle refractive index difference, the birefringence Δn ($= n_I - n_{II}$), according to

$$\delta = \frac{2\pi d}{\lambda}\Delta n \tag{2.11}$$

where λ the wavelength of light in vacuum, and d the length of the light path in the birefringent medium [1].

2.3.2 Flow Induced Birefringence of polymers

Numerous studies (e.g. [60], [91],[111]) have shown that flowing polymer melts and solutions are birefringent: this phenomenon is called Flow Induced Birefringence (FIB). It is found that in general the linear stress optical rule applies. This rule can be deduced from molecular optics and polymer physics.

Stress optical rule

According to the stress optical rule, the deviatoric part of the refractive index tensor, $\hat{\boldsymbol{n}}$, $\hat{\boldsymbol{n}} = \boldsymbol{n} - \frac{1}{3}tr(\boldsymbol{n})\boldsymbol{I}$, and the deviatoric part of the Cauchy stress tensor $\boldsymbol{\sigma}$, $\hat{\boldsymbol{\sigma}} = \boldsymbol{\sigma} - \frac{1}{3}tr(\boldsymbol{\sigma})\boldsymbol{I}$, are proportional:

$$\hat{\boldsymbol{n}} = C\hat{\boldsymbol{\sigma}}, \tag{2.12}$$

[1] 'Retardance' is often used for $\frac{\delta}{2\pi}\lambda = d\Delta n$, which expresses the phase retardance as a number of wavelengths

where C is the stress optical coefficient, tr denotes the trace of a tensor, $\boldsymbol{I}$ is the unit tensor. The (intrinsic) birefringence is a result of the polymer molecular orientation and deformation only (see below). For polymer solutions the extra-stress tensor $\boldsymbol{\tau}$ ($\boldsymbol{\sigma} = -p\boldsymbol{I} + \boldsymbol{\tau}$, p: hydrostatic pressure) is splitted as

$$\boldsymbol{\tau} = \boldsymbol{\tau}_v + \boldsymbol{\tau}_p, \tag{2.13}$$

with $\boldsymbol{\tau}_v$ a viscous part (the 'solvent' contribution) and $\boldsymbol{\tau}_p$ a viscoelastic part (the 'polymer' contribution). Then the stress optical rule is assumed to be valid after subtraction of the viscous stress term $\boldsymbol{\tau}_v$ from the stress $\boldsymbol{\sigma}$ (giving $\boldsymbol{\sigma}_p$):

$$\hat{\boldsymbol{n}} = C\hat{\boldsymbol{\sigma}}_p. \tag{2.14}$$

In a planar complex flow of a birefringent polymer, the orientation of the (principle) axes frame relative to the fixed laboratory frame varies from point to point in the plane perpendicular to the direction of the wave propagation. This is illustrated by the diagram in Figure 2.3.

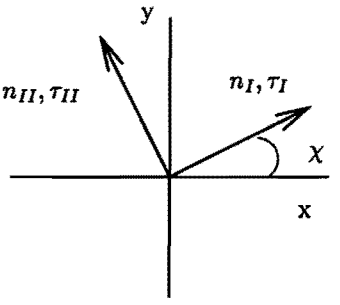

Figure 2.3: *Diagram illustrating the local orientation χ of the principle axes of the refractive index tensor (the principle values are denoted with n_I, n_{II}) and of the extra stress tensor (τ_I and τ_{II}) relative to the laboratory x, y-frame for a (flow induced) birefringent medium in case that the linear stress optic rule applies.*

The local principle axes frame of the birefringence is inclined at an angle χ relative to the fixed laboratory frame. The stress tensor in the fixed Cartesian laboratory frame $\boldsymbol{\tau}_p^{x,y}$ is related to the stress tensor $\boldsymbol{\tau}_p$ in the principle axis frame by

$$\boldsymbol{\tau}_p^{x,y} = R_{-\chi}\boldsymbol{\tau}_p R_\chi \tag{2.15}$$

where R_χ is the rotation matrix, i.e. the matrix that describes the coordinate transformation between two coordinate frames that have a relative orientation such that their positive x-axes make an angle χ:

$$R = \begin{bmatrix} \cos\chi & \sin\chi \\ -\sin\chi & \cos\chi \end{bmatrix}. \tag{2.16}$$

Thus for the components of the stress tensor τ_p it is found:

$$\tau_{xy} = \frac{\Delta n}{2C} \sin 2\chi \tag{2.17}$$

$$N_1 = \tau_{xx} - \tau_{yy} = \frac{\Delta n}{C} \cos 2\chi. \tag{2.18}$$

The calculation of stresses from a birefringence measurement involves the measurement of two observable physical parameters: the birefringence Δn and the local orientation angle χ. Since the birefringence is an integrated effect along a light beam, only birefringence data of two-dimensional fields without birefringence gradients in the propagation direction of the light wave can be translated into stresses by a simple calculation. In practice, a three-dimensional flow field will exist near the edges of a nominally two-dimensional flow, that is obtained in a planar channel with a high aspect ratio of the flow cell length along the 3-direction and the length along the 2-direction.

The validity of the stress optical rule has been proven for various polymeric materials in shear flows ([60], [91],[111]) for a wide range of shear rates. In viscometric shear flows it is fairly easy to compare optical measurements with mechanical experiments and check the linearity of the rule.

In the review of Mackay and Boger [75], several studies are listed that did attempt to validate the stress optical rule in elongational flows. However, despite many efforts, results of measurements of mechanical stresses in elongational flows are not reliable or impossible, due to inherent experimental difficulties (Walters [112]). Therefore, unfortunately, in such flows presently a reliable, direct validation of the stress optic rule by comparison with mechanical measurements is not feasible.

Nevertheless, it is generally agreed that the stress optical rule breaks down in case of large extensional deformation (Fuller [36], Mackay and Boger [75]). This is explained by saturation of the polymer orientation and stretching. However, complete orientation of polymer segments can not be achieved experimentally with polymer melts or concentrated solutions (Fuller [36] mentions several studies of *dilute* solutions that did observe saturation of segmental orientation in strong extensional flows).

The stress optical rule is predicted by molecular theories for the fluid dynamics of polymeric liquids. The basic theory is discussed next.

Birefringence and stress optical rule from molecular optics

The macroscopically observed birefringence of flowing polymeric materials can be explained from microscopical parameters. Two types of birefringence can be distinguished: intrinsic (or conservative) birefringence, and form (or consumptive) birefringence.

The intrinsic birefringence origins from the difference in polarizability of a polymer chain segment in two directions: along its backbone and perpendicular to that. The linear stress optical rule (2.12) applies to this effect. As will be shown below, this rule is explained by the proportionality of both the stress tensor and the refractive index tensor with $< \vec{R}_i \vec{R}_i >$,

where the brackets $< \cdot >$ represent the averaging over the distribution function describing molecular orientations and $\vec{R}_i$ the end-to-end vector of a polymer chain segment.

The form birefringence is due to a refractive index difference on a much larger length scale: it is related to the difference in refractive index between the solute and solvent, and to the anisotropy of the shape of the dissolved molecules in the solvent. The effect is proportional to the square of the difference in refractive index between dissolved molecules and solvent (Copic [26], Doi and Edwards [31]). Form birefringence is not proportional with $< \vec{R}_i \vec{R}_i >$, which causes the stress optical rule to break down. It also decreases steeply with increasing concentration, and for concentrated solutions the effect can be neglected (Doi and Edwards [31], Takahashi et al. [105]). Solutions are considered concentrated when their concentration exceeds the critical concentration c^* for polymer-coil overlapping as defined by (originally by de Gennes [42], see also Larson [70]):

$$c^* = 3M/(4 * \pi < s^2 >^{3/2} N_A), \tag{2.19}$$

where M is the molecular weight of the polymer, $< s^2 >$ is the mean square radius of gyration of the polymer and N_A is Avogadro's number. This definition is valid in both *theta* and *good* solvents. The critical concentration of a solution of the polyisobutylene that is used in this study is $c^* = 0.11\%(w/w)$ (Quinzani et al. [73]). The form birefringence can thus be neglected in the present study.

In the following the stress optic rule will be derived from molecular theory. The dielectric diplacement $\vec{D}$ is related, by definition, to $\vec{E}$ and $\vec{P}$, the electric field in vacuum and the polarization in the dielectric respectively (see Appendix A). Assume the dielectric to be isotropic, then the dielectric tensor $\boldsymbol{\epsilon}$ can be replaced by the scalar ε. The polarization is the macroscopically averaged induced dipole moment. It is proportional to the average dipole moment of the molecules $\langle \vec{p}_{mol} \rangle$:

$$\vec{P} = N \langle \vec{p}_{mol} \rangle \tag{2.20}$$

where N is the number of molecules per unit volume. In the dielectric the electric field is a summation of the external field $\vec{E}$ and the internal electric field $\vec{E}_{int}$, so that the molecular polarizability α is defined by:

$$\alpha(\vec{E} + \vec{E}_{int}) = N \langle \vec{p}_{mol} \rangle \tag{2.21}$$

The internal field $\vec{E}_{int}$ is assumed to be proportional to the polarization vector $\vec{P}$ (Jackson [59]):

$$\vec{E}_{int} = 1/3\varepsilon_0 \vec{P} \tag{2.22}$$

Equations 2.20, 2.21 and 2.22 can be combined to

$$\vec{P} = \chi_e \vec{E} \tag{2.23}$$

where χ_e is the electrical susceptability defined by

$$\chi_e = \frac{\alpha N}{1 - \alpha N/3\varepsilon_0}. \tag{2.24}$$

Realizing that $\varepsilon = \varepsilon_0 + \chi_e$, and that $\varepsilon/\varepsilon_0 \approx \varepsilon$ the Clausius-Mossotti relation is found:

$$\alpha = \frac{3\varepsilon_0}{N}\frac{\varepsilon - 1}{\varepsilon + 2}. \tag{2.25}$$

In the optical frequency range ε can be replaced by n^2, with n the refractive index (Equation 2.25 is then referred to as the Lorentz-Lorentz equation).

Assume that the Clausius-Mossotti relation is valid for each principle refractive index separately, each with its own principle molecular polarizability α_i, then $n_I - n_{II}$ is related to $\Delta\alpha = \alpha_1 - \alpha_2$ by

$$\frac{{n_I}^2 - 1}{{n_I}^2 + 2} - \frac{{n_{II}}^2 - 1}{{n_{II}}^2 + 2} = \frac{N}{3\varepsilon_0}(\alpha_1 - \alpha_2). \tag{2.26}$$

With $\frac{\Delta n}{\bar{n}} << \bar{n}$ ($\bar{n}$ is the mean refractive index) the result is

$$\Delta n = \frac{N}{18\varepsilon_0}\frac{(\bar{n}^2 + 2)^2}{\bar{n}}\Delta\alpha. \tag{2.27}$$

Kühn and Grun ([67]) introduced the description of the optical anisotropy of flexible polymer molecules by the use of a conformation distribution function describing orientation of chain segments. They assumed the model with freely rotating chain segments to represent the polymer molecule. The chain consists of N segments of length b that are linked by freely rotating joints. Each i-th chain segment has an end-to-end vector $\vec{R}_i$ with length R_i, while the deformation of each segment is assumed to be within the limit of a Gaussian coil (i.e. a Gaussian distribution function applies for the molecular orientations). It is further assumed that the polarizability of each segment is uniaxial with eigenvalues $(\alpha_1, \alpha_2, \alpha_2)$, and that the overall polarizability of the chain is the result of the addition of all segmental contributions. The (incremental) contribution $\boldsymbol{\alpha}_i$ of a chain segment to the anisotropic part of the overall polarizability of the chain is (Kühn and Grun [67], Janeschitz-Kriegl [60]):

$$\boldsymbol{\alpha}_i = \frac{3}{5}[\frac{(\alpha_1 - \alpha_2)}{n_k b^2}] < \vec{R}_i\vec{R}_i > . \tag{2.28}$$

where $n_k b^2$ is the mean square end-to-end distance of the chain segment. From Equation 2.27 it is found that the principle value difference of the overall refractive index tensor is

$$\Delta n = \frac{N}{18\epsilon_0}\frac{(\bar{n}^2 + 2)^2}{\bar{n}}\Delta\alpha_i. \tag{2.29}$$

where $\Delta\alpha_i$ is the principle value difference for the i-th chain segment in the $1,2$ plane of the increment in the polarizability tensor. Combining Equation 2.28 with the well-known expression for the stress tensor for a Gaussian chain segment (e.g. Larson [70])

$$\boldsymbol{\sigma}_i = \frac{3kT}{n_k b^2} < \vec{R}_i\vec{R}_i >, \tag{2.30}$$

it follows that

$$\boldsymbol{\sigma}_i = 5kT\frac{1}{(\alpha_1 - \alpha_2)}\boldsymbol{\alpha}_i, \tag{2.31}$$

and for the principle stress difference $\Delta\sigma_i$

$$\Delta\sigma_i = 5kT\frac{1}{(\alpha_1 - \alpha_2)}\Delta\alpha_i. \tag{2.32}$$

From Equations 2.29 and 2.32 the stress optic coefficient C, such that $\Delta n = C\Delta\sigma$, is found:

$$C = 5kT\frac{N}{18\epsilon_0}\frac{(n^2+2)^2}{n}(\alpha_1 - \alpha_2). \tag{2.33}$$

Note that C does not depend on molecular weight.

2.3.3 Fieldwise measurement of birefringence

Fieldwise measurement of birefringence is a classical method for studying birefringence distributions in solids (Kuske and Robertson [68]), polymer melts and highly birefringent solutions (Mackay and Boger [75]). The stress optical rule enables the interpretation of birefringence data in terms of stresses. Fuller [37] describes numerous systems for birefringence measurements. Details can also be found in the book of Azzam and Bashara [5]. The experimental set-up used for such measurements is called a polariscope. In the following, two polariscopes and the equipment used in the present study are described. The polariscopes, drawn schematically in Figure 2.4 are in the sequel referred to as polariscope (I) and (II). By combining (I) and (II) both χ and δ can be measured in a two-step procedure.

The polariscope (I) consists of two crossed polarizers that have a relative orientation of their transmission axes of 90°, with the birefringent sample placed in between. A light source illuminates the sample through the first polarizer and the transmitted light is photographed or video-recorded after the second polarizer (=analyzer). The light source can emit either white or (quasi) mono-chromatic light. The intensity of light transmitted through a cascade of optical devices that affect the polarization of the light can be calculated with Müller matrices. The intensity of the light in polariscope (I) after the second polarizer is described by

$$I = \frac{I_0}{2}\sin^2 2(\chi - \alpha)\sin^2\frac{\delta}{2}, \tag{2.34}$$

where I_0 is the intensity of the light source, α is the angle of the transmission axis of the polarizer with the positive $x-$axis of the fixed laboratory frame, χ is the (local) orientation of the optical axis of the birefringent sample relative to the fixed laboratory frame (often referred to as 'extinction angle'), and δ is the relative phase retardation between the extraordinary and ordinary ray. This type of polariscope is a 'dark field' polariscope: in the absence of flow the whole image is black.[2] In case of a white light source the image past the analyzer contains a pattern of black and colored fringes. These two types of fringes contain different information:

[2]In case of two parallel polarizers a 'white field' polariscope is obtained with $I = \frac{I_0}{2}(1 - \sin^2 2(\chi - \alpha)\sin^2\frac{\delta}{2})$.

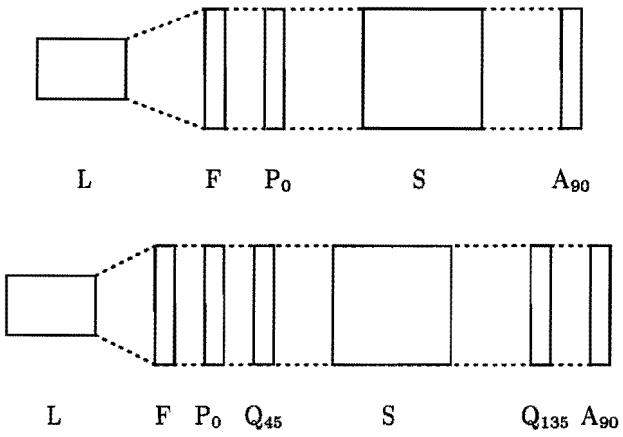

Figure 2.4: *Schema's of the polariscopes (referred to with (I) and (II) (from top to bottom)) used for whole field measurements of birefringence ('fringe method') with fixed elements. L: light source , F: monochromatic filter, P: polarizer, Q: quarter wave plate, S: birefringent sample, A: analyzer. The subscripts denote the angle of rotation between the principle axis frame of the element and the principle axis frame of the first polarizer. The dashed lines denote the fieldwise illumination of the optical train.*

Isoclinics: The black lines, the isoclinics, are due to the relative orientation of the optic axis of the birefringent sample to the orientation of the two polarizers at the position of the lines. Equation 2.34 shows that when this angle $\chi - \alpha$ is zero, the light is extinguished. When the two polarizers are rotated simultaneously the isoclinics will move too.

Isochromatics: The colored fringes, the isochromatics, mark the positions where the retardation $\delta = \pm k\,2\pi$, with $k = 0, 1, 2, \ldots$. Since according to Equation 2.11 the retardation is wavelength dependent, each color has its own position where it is extinguished in the polariscope. Extinction of a single wavelength results in a specific color of the transmitted light at that position, only the zero-order isochromatic line ($\delta = 0$) is black (extinction of all wavelengths at the same position). Simultaneously rotation of the polarizers will not affect the position of the isochromatics.

To calculate the stress levels, both the angle χ and the retardation δ have to be measured. This requires a two-step procedure: χ and δ can not be measured fieldwise simultaneously. For this purpose, usually the experiment is performed with mono-chromatic light such that a single frequency is involved. Both isoclinics and the isochromatics appear then as black lines on a single colored background.

In the first step, polariscope (I) is used to measure the extinction angle χ. The isoclinics and isochromatics can be distinguished from each other by rotating both polarizers simultaneously while retaining their crossed orientation: the isoclinics will move while the positions of the isochromatics remain stationary. The angle of rotation α determines the position of the isoclinics that are measured. The sign of the extinction angle is lost in this measurement.

The second step involves the measurement of the birefringence with polariscope (II). In this case only isochromatic fringes are observed and the intensity signal is

$$I = \frac{I_0}{4} \sin^2 \frac{\delta}{2}. \tag{2.35}$$

Instead of the laborious construction of the stresses from the measured distributions of χ and δ, the birefringence Δn itself can be used too for a comparison of experiment with computations. In the experiment, the birefringence is obtained using polariscope (II) by counting the fringe order (from a zero order fringe that is known by symmetry considerations or by counting fringes during start up of the flow). In the computations, the relation between Δn and the stresses τ and N_1 is according to the stress optical rule:

$$\Delta n = C\sqrt{4\tau^2 + {N_1}^2}. \tag{2.36}$$

The technique as described above has some limitations:

Minimum retardance level: to obtain a fringe pattern, multiple order transitions for the retardance are required. For each subsequent order transition the retardance must be increased with 2π, which implies an increment of the birefringence equal to $\frac{\lambda}{d}$ (Equation 2.11). Estimating $d = \mathcal{O}(10^{-2})\,m$ and $\lambda = \mathcal{O}(10^{-6})\,m$, the birefringence difference between two subsequent fringes is $\mathcal{O}(10^{-4})$. This is a typical resolution of a birefringence measurement based on measuring fringes. The birefringence in an experiment scales with λ, d and also with the stress optical coefficient C and the magnitude of the stresses. Since the order of magnitude of C is invariant for polymer melts and solutions (e.g. Funatsu and Kajiwara [39], Wales [111]), and λ and d can in practice be varied only in a limited range , the stress level in flowing polymeric materials determines the number of fringes. For solutions with relatively low viscosities it will be impossible to create stress levels such that the birefringence exceeds 10^{-4}. (A typical example is: stresses of $\mathcal{O}(10^2)\,Pa$, C of $\mathcal{O}(10^{-9})\,Pa^{-1}$ result in birefringence of $\mathcal{O}(10^{-7})$).

Maximum retardance level: In areas with very large stress gradients the number of fringes will be so large that subsequent fringes can not be resolved anymore. This limits the maximum birefringence level that can be resolved. The limit for the stress gradients can be estimated (with a minimal resolvable distance between two fringes of $\mathcal{O}(10^{-4})\,m$, $C = \mathcal{O}(10^{-9})\,Pa^{-1}$ and difference in birefringence between two fringes of $\mathcal{O}(10^{-4})$) to be $\mathcal{O}(10^9)\,Pa/m$.

Absolute measurement of birefringence: In any birefringence measurements a problem exists with the absolute measurement of the birefringence, since a sinusoidal relation exists between measured intensity and retardation δ. The inverse sine operation to calculate the retardance from Equation 2.35 yields a value for δ between $-\pi$ and π; there will be ambiguity in the value when multiple order transitions exist. By counting the fringes during start-up or cessation of flow the absolute value can be obtained without ambiguity.

The optical elements used in the experiments performed in the present study are listed in table 2.1. All elements were mounted in line on an optical rail (Melles Griot, 07ORN009) The fringe patterns were observed through a microscope (Olympus, SZ4045TR) with a $1.67 - 10$ magnification. Photographs through this microscope were made with a photocamera , while additionally video recordings were made with a videocamera (Panasonic, F15).

Device	Manufacturer	Part number
polarizer	Meadowlark Optics	DPM-1.5-HN38s
$\frac{\lambda}{4}$-plate	Meadowlark Optics	NQM-1.5-546
interference filter $546\,nm$	Spindler and Hoyer	37.1105
mercury lamp	Philips	

Table 2.1: *List of elements used in the polariscopes.*

2.3.4 Pointwise birefringence measurement with a polarization modulation method

Birefringence techniques that use polarization modulation of light enable simultaneous and pointwise measurement of both extinction angle χ and phase retardation δ. Fuller [36] reviewed this subject. In the present study, the polarization modulation technique is applied that uses a rotating half wave plate (as introduced by Fuller and Mikkelsen [38]). The measurement system, called Rheo Optical Analyzer (ROA), was provided by Fuller. In the following, the theory of the technique and the equipment used are described.

Theory

Figure 2.5 shows schematically the measurement system ROA. Neglecting system imperfections, the time-dependent intensity signal is described by (Fuller and Mikkelsen [38])

$$I = \frac{1}{4} I_0 (1 + R_1 \sin(4\omega t) + R_2 \cos(4\omega t)) \tag{2.37}$$

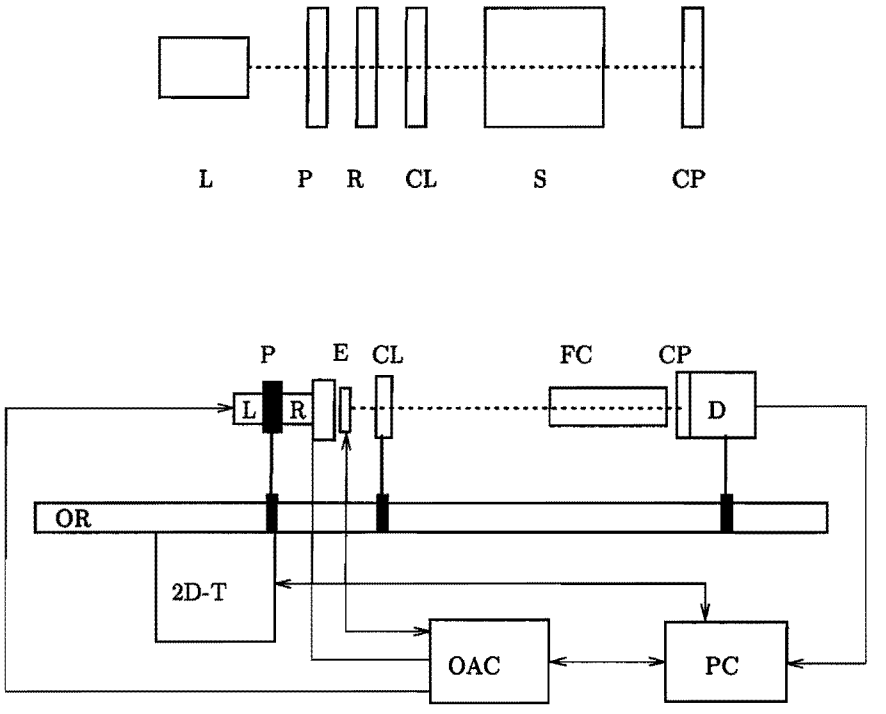

Figure 2.5: *The measurement system ROA for pointwise birefringence measurements. Top figure: scheme of the optical train, the dashed line illustrates the point-wise illumination of the sample. Bottom figure: scheme of the whole ROA system. The laser light emitted by a diode laser (L) passes successively a polarizer (P) , a rotating half wave plate (R) ($\omega \approx 100s^{-1}$), a collimating lens (CL), the birefringent sample (S, FC: flow cell) and a circular polarizer (CP) before its intensity is measured by a detector (D). From the intensity signal both the extinction angle χ and retardation δ are obtained simultaneously. A computer controlled XY-traverse table (2D-T), enables the positioning of the optical rail (OR). The Optical Analyzer Controller (OAC) supplies the laser and the electromotor with power, and registers the encoder disc (E) signal. This signal is the reference signal that is used in the data-acquisition and processing software. Data-acquisition and control of the experiment is performed by a personal computer (PC).*

where I_0 is the intensity at the exit of the diode laser, and R_1 and R_2 are

$$R_1 = -\sin\delta\cos 2\chi \tag{2.38}$$
$$R_2 = \sin\delta\sin 2\chi. \tag{2.39}$$

R_1 and R_2 are obtained from the measured intensity signal by means of a Fourier transformation (Equation 2.37 can be calculated with the Müller matrices listed in Appendix B). Assuming that $\chi \in [-\frac{\pi}{4}, \frac{\pi}{4}]$ the angles χ and δ follow directly from Equations 2.38 and 2.39:

$$\chi = \arctan(-R_2/R_1) \tag{2.40}$$
$$\delta = sign(R_1)\sqrt{R_1^2 + R_2^2}. \tag{2.41}$$

Stresses can now be found after substitution of Equations 2.40 and 2.41 (and using Equation 2.11) in Equations 2.18. The system is capable of measuring birefringence as low as $\mathcal{O}(10^{-8})$, which is orders of magnitudes lower than for the fieldwise method ($\mathcal{O}(10^{-4})$). This is, because the technique does not depend on the existence of fringes. In case of the flow of highly birefringent materials like polymer melts where high stress gradients can exist, the finite size of the cross section of the laser beam (measuring area) can be a serious limitation. When the measuring area is not small compared with the distance between two fringes (=order transitions for the retardance δ), the results will be inaccurate since averaging will take place over a large range of stresses. In case the measuring area contains two or more fringes the results become meaningless. Accurate results are obtained as long as stress gradients are of (in a flow cell with $d = \mathcal{O}(10^{-1}\,m)$ using a minimal distance between two fringes of $\mathcal{O}(10^{-2}\,m)$) $\mathcal{O}(10^{7})\,Pa/m$. Details about dimensions and formulas that describe the focusing of laser beams are presented in Appendix C.

Equipment

The diode laser (Power Technology Inc.) emits linear polarized light with a wavelength $\lambda = 672.4nm$ (at $25°C$, for diode lasers the temperature dependence is reflected in a wavelength shift of typically $\approx 0.4nm/(°C)$). The shape of the original laser beam, which was in general elliptical, was corrected by the manufacturer to produce a beam with circular cross section that is approximately Gaussian. The intensity of the laser beam can be adjusted by rotating the laser in its housing: the plane of polarization of the emitted light from the diode laser will change relatively to the fixed polarizer that is mounted in front of the rotating wave plate. The original rotating half wave plate (Meadowlark Optics, $AHM - 0.50 - 672$), is achromatic in the range $0.85 < \frac{\lambda}{\lambda_c} < 1.15$ around the central wavelength λ_c ($= 672.4nm$). We observed that the beam deviation of this plate did not meet our requirements. It was $\approx 1\,arcmin$ which resulted in a beam with a spot that traced a circle. Therefore, it was later replaced by a quartz first-order wave plate (Melles Griot, O2WRQ023-diameter 6.35 mm, $\lambda = 672.4\,nm$) with a tolerance for the beam deviation $< 1\,arcs$ (see Section 4.5), which functioned properly according to our specifications. The

wave plate is rotated by an electromotor at a frequency of $\approx 100\,s^{-1}$, the frequency of the polarization modulation being a four-fold of that (see Equation 2.37). The laser and electromotor are power supplied by a separate hardware unit (Optical Analyzer Controller, type 9304), that also transmits the rotation frequency of the wave plate that is registered by means of an encoder disc mounted externally on the waveplate device. The circular polarizer (Meadowlark Optics, $NHM-0.50-672$) is fixed in the housing of the detector. It is a true circular polarizer, with no optical axis in the plane perpendicular to the laser beam. It can be mounted with either side towards the incident beam.

The flow cell is fixed to the laboratory, while all optical components of the measurement system are mounted on an optical rail (Melles Griot, 07ORN009). This rail is fixed on a XY-traverse table (Parker Daedal, 106042 P-10E-LH) driven by two OEM $57-83$ stepper motors controlled by a 6200 microprocessor based two-axis indexer (Parker Compumotor), that can translate the optical rail in two directions, each over a distance of $100\,mm$ with an accuracy of $\approx 0.1\mu m$. The control of the traverse table was not part of the original system, and has been incorporated in ROA by ourselves (Kruijt [66]). Control of the experiment and data-acquisition are performed by the ROA software, that is implemented in the package LABView (National Instruments, LABView for Windows), with a personal computer (486DX-50 MHz, 8 Mb, 240 MB hard disk, 17" SVGA screen (Eizo F550i-W)) equiped with a data-acquisition board (National Instruments, AT-MIO-16L9).

Experimental procedures and the correction for a small imperfection in the half-wave plate on R_1 and R_2 are described in Kruijt [66]. Appendix E contains an analysis of the statistical error in the stresses that are obtained from measurements with ROA.

2.4 Discussion

End-effects in birefringence measurements in nominally two-dimensional fields
In the application of flow induced birefringence measurements described in the previous Section, a two-dimensional flow field is assumed that is invariant along the direction of the propagating light wave. However, in practice three-dimensional effects will be present along constraining walls perpendicular to this direction. A typical rectangular duct is plotted in Figure 2.6. Three orthogonal axes can be defined, labeled with 1, 2 and 3: the 1-axis defines the mean flow direction, the 2-axis defines the direction of the velocity gradients in the duct where the flow is two-dimensional, and the 3-axis defines the direction of the propagating lightwave ('neutral direction'). Early work of Wales [111] showed by variation of the aspect ratio that at aspect ratios W/h larger than 10 the effect is minimized and can be neglected. Rajagopalan et al. [96] compared mechanical and optical stress measurements in Couette flow, and found that the optically measured curve of N_1 as function of τ was 7% lower than the one which was mechanically measured.

Several studies have theoretically analyzed these effects in more detail (e.g. Burghardt and Fuller [19] and Galante [41]). The propagating light wave will experience two secondary-principle refractive indices, that are the projection of the principle axes of the three-dimensional refractive index ellipsoid on the plane perpendicular to the direction of the

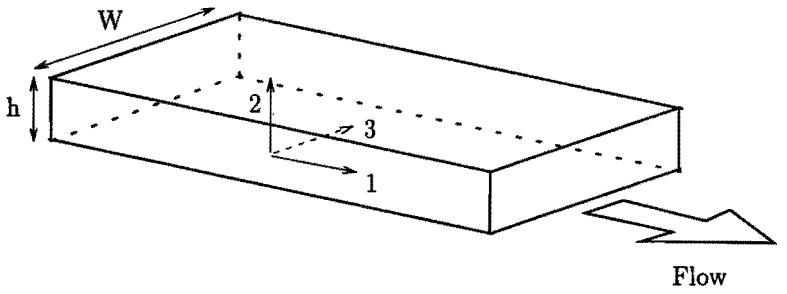

Figure 2.6: *A typical rectangular duct for creating a nominally two-dimensional flow. The labels 1, 2 and 3 denote an orthogonal frame. The aspect ratio W/h is chosen sufficiently large to assume nominally two-dimensional flow.*

light wave propagation. For a viscoelastic fluid the effect of a velocity-gradient in the $1-3$ plane is a contribution to the normal stress difference N_1 in the $1-2$ plane, that varies with position along the 3-axis in the edge-region of the confined flow. Also the projection of the optical axis on the $1-2$ plane, the extinction angle χ, varies along that axis. Galante [41] estimated the measured birefringence in the fully developed flow of an UCM fluid and a power-law fluid in a rectangular duct with an aspect ratio of $1:10$ are 7% too low, due to the variation of the shear in the $1-2$ plane along the 3-direction. He ignored however the contribution of shear in the $1-3$ plane to τ_{11}.

In conclusion, the effect of the three-dimensional flow in the edge regions of a rectangular duct are small if the aspect ratio W/h is approximately 10, but may be of roughly $\mathcal{O}(10\%)$.

Analysis of flow birefringence in three-dimensional fields The analysis of birefringence in terms of stresses in fully three-dimensional fields is still an open problem. The measured one-dimensional intensities along a grid of lines in a plane through the flow field might be inversely-transformed to obtain the two-dimensional distribution of χ and δ in that plane, using methods developed in imaging techniques. Cathey and Fuller [21] have applied such an inverse-transform method to calculate stresses in a non-planar birefringence measurement, assuming axisymmetry in the stress field. It seems that such calculation of stress distributions in non-planar flows could be an interesting topic for future research. However, the standard inverse-transformation techniques involve scalar instead of tensorial quantities. Therefore, Burghardt [18] advocates the use of optical quantities (i.e. R_1, R_2 in case of ROA), that can be calculated from the computed stress distribution, to compare with measured data.

Alternative techniques The two optical techniques described in this Chapter enable detailed quantitative measurements of velocity fields and stress fields in complex flows.

Since both techniques are optical, they require a transparent fluid, and a flow cell that is accessible for light.

In case of the velocity measurements with a laser Doppler anemometer information can only be obtained point-wise in space. Furthermore, to measure simultaneously more than one velocity component the light-paths of all laser beams must be symmetric. This implies in practice refractive index matching between flow cell and fluid. This is a major problem when studying the rheology of polymeric materials: how can refractive index matching be obtained without changing the fluid properties? The recent development of particle image velocimetry (PIV, see for example Adrian [2] for a review) surmounts partly these two limitations of the laser Doppler technique: it measures velocity vectors in a whole plane (thus two velocity components) without the need of refractive index matching (see Adrian [2]). But it is still an optical technique, which requires a transparent liquid. The latter limitation might be surmounted by the Magnetic Resonance Imaging (MRI) technique, as demonstrated in Couette flow by Rofe et al. [97] and in capillary flow by Lambert et al. [69].

The birefringence techniques have the limitation that only information of the *sine* of the retardance is measured. The only accurate way to obtain the retardance when multiple order transitions are present, is measuring the birefringence during start-up or cessation of flow and counting the number of order-transitions. This is a tedious procedure when using the pointwise ROA technique. Hongladarom et al. [53] have developed a white light system with crossed polarizers that can analyze samples with multiple orders in retardance without ambiguity. In that system, it is necessary to assume that the birefringence is invariant with wavelength or to measure its wavelength dependence (dispersion) separately. However, a white light source can not be collimated to an intense beam with a small cross section comparable with that of a laser beam. Therefore this method is not useful for pointwise mapping of stresses in a complex flow of highly-birefringent materials. The two-color rotary modulated birefringence method of Abetz and Fuller [1], that uses simultaneously two laser beams of different wavelengths, enables the measurement of birefringence without ambiguity up to approximately 10 order transitions.

Chapter 3

Rheological characterization in simple shear

3.1 Introduction

A rheological characterization in simple shear flow of three polyisobutylene solutions was performed. Two of these solutions will be used as model liquids in Chapter 4. Model liquids facilitate the analysis both numerically and experimentally (see Section 1.5). These characterizations are necessary to obtain parameters of the non-linear viscoelastic constitutive equations that will be used in the complex flow simulations in Chapters 4 and 5. For the LDPE melt, measured data and model parameters have been taken from an earlier study in our group and also some new fits have been made. Predictions in planar elongational flow will be presented too, to illustrate the sensitivity of the models for two dimensional elongational deformation.

Data for three shear thinning polyisobutylene solutions are presented: for a 5%(w/w) polyisobutylene (PIB) in tetradecane solution (C14), for a 9%(w/w) PIB/C14 solution and for the standard fluid S1 (Sections 3.4, 3.5 and 3.6 respectively). The first two fluids will be referred to as 5% PIB/C14 and 9% PIB/C14 solution respectively in the sequel, and will be used as model fluids in Chapter 4. The 5% PIB/C14 solution has also been used extensively by the group of Armstrong et al. (e.g. [4], [93]), which provides a reference for the present work. They also demonstrated pointwise stress and velocity measurements with this fluid. The 9% PIB/C14 solution is used to reach higher Deborah numbers at the same flow rate, thus to be closer to the behavior of polymer melts. The S1 fluid is used mainly to compare our viscometric data with reference data of Ferguson and Hudson [34] which demonstrates the accuracy of our measurements.

To illustrate their rheological differences, the material functions $\eta(\dot{\gamma})$ and $N_1(\dot{\gamma})$ in steady simple shear are plotted together for the three solutions in Figure 3.1. The steady shear viscosity function $\eta(\dot{\gamma})$ is fitted excellently with the Carreau-Yasuda equation (Equation 3.1) in all three cases. The parameter values for this viscosity function are tabulated in Table 3.1, and the fits are drawn in Figure 3.1 with dashed lines. It appears that the

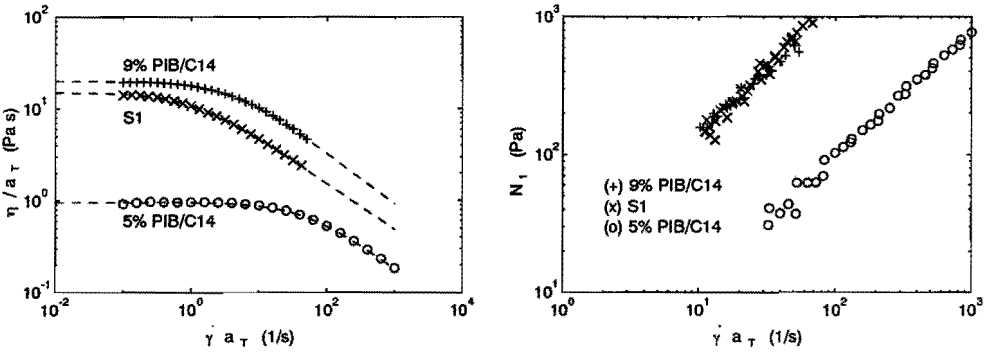

Figure 3.1: *Left: master curves for $\eta(\dot{\gamma})$ of the three solutions used (only data for $T = 25\,°C$ are shown to avoid congestion). The dashed lines represent the fits with the Carreau-Yasuda model. Right: master curves for the first normal stress difference $N1(\dot{\gamma})$ of the same solutions.*

steady shear behavior of the 9% PIB/C14 solution is close to that of the standard solution S1. The values for 5% PIB/C14 are at all shear rates roughly one order of magnitude smaller.

parameter	5% PIB/C14	9% PIB/C14	S1
η_{cy}	0.96	20	15
λ_{cy}	0.02	0.24	0.94
n	0.45	0.44	0.5

Table 3.1: *Parameter values of the Carreau-Yasuda equation (with $a = 1$) for the three polyisobutylene solutions used.*

3.2 Constitutive equations

In Chapter 1, the types of constitutive models that are studied in this study have been introduced. For a profound introduction in constitutive models for viscoelastic polymer melts and solutions, the reader is referred to, for example, the book of Larson [70].

A generalized Newtonian constitutive model and two non-linear viscoelastic constitutive equations have been used to fit the rheological data. As a generalized Newtonian model, the Carreau-Yasuda model has been used:

$$\eta = \eta_{cy}(1 + (\lambda_{cy}\sqrt{II_D})^a)^{(n-1)/a}. \tag{3.1}$$

The viscoelastic constitutive equations that have been used are of the differential type: the Phan-Thien Tanner model (Phan-Thien and Tanner [90], referred to with PTT), and the Giesekus model (Giesekus [44]). The definitions of these models have been given in Table 1.1 in Chapter 1. In literature, both PTT and Giesekus models have been applied to flows of various polymer solutions and melts, not only in simple shear flow but also in elongational and complex flows (see for example Larson [70]). They were most favored to model concentrated solutions and polymer melts at the 'VIIIth International Workshop on Numerical Methods in Viscoelastic Flows' in 1993 (Brown and McKinley [17]). These models meet the mininum requirements stated at that workshop: they have bounded extensional viscosities in straining flows, shear-thinning viscometric material functions, are capable of using a spectrum of relaxation times and can predict a non-zero second normal stress coefficient. Furthermore, Armstrong et al. [4], who compared six constitutive equations of the differential type, have shown that center line stresses in the flow of the 5% PIB/C14 solution through a four-to-one contraction were best described by a four mode PTT-B model, and second best by a four mode Giesekus model. Tas [107] applied the PTT-A model to uniaxial and biaxial elongation flow of LDPE and found excellent agreement with measured data, and also good agreement for the Giesekus model.

The two versions of the PTT model (PTT-A and PTT-B) differ most strongly in their prediction of the elongational viscosity: the elongational viscosity of the PTT-A model first reaches a maximum and then decreases with increasing elongational rates (elongational thinning). The PTT-B model predicts an elongational viscosity that increases with increasing elongational rate towards a plateau value at high rates. The first behavior is assumed to be valid for polymer melts, while the second type of behavior is more correct for polymer solutions (Larson [70]). However, the PTT-B model has also been found to predict stresses accurately in flows of LDPE melt through a converging channel by Kajiwara et al. [62].

Besides multimode also single mode models will be used too. This despite the fact that it has been found in literature that multimode versions of these constitutive equations not only improve fits of rheological data in one-dimensional flows such as simple shear (e.g Quinzani et al. [93]) but also give better predictions of the flow field in complex flows. This is shown by for example Rajagoplan et al. [96], who studied the flow of a polymer solution between two eccentric rotating cylinders, and by Becker et al. [11], who studied the unsteady motion of a sphere falling in a viscoelastic fluid in a tube. Single mode models, however, are attractive for numerical computations since they can reduce the required computer time and memory significantly compared with multimode models.

3.3 Definition of deformation types and material functions

Experiments have been performed in simple shear flows, both steady and small amplitude oscillatory shear flow, while predictions of the constitutive equations in planar elongation

have been analyzed too. These flows are homogeneous, thus the matrix representation D of the rate-of-deformation tensor $\boldsymbol{D}$ is known a priori. In case of simple shear

$$D = \frac{1}{2}\begin{bmatrix} 0 & \dot{\gamma} \\ \dot{\gamma} & 0 \end{bmatrix} \tag{3.2}$$

with $\dot{\gamma}$ the shear rate. In case of planar elongation:

$$D = \begin{bmatrix} \dot{\epsilon} & 0 \\ 0 & -\dot{\epsilon} \end{bmatrix} \tag{3.3}$$

where $\dot{\epsilon}$ is the elongational rate. The definitions of the material functions then are:

steady shear viscosity: $\eta = \tau_{12}/\dot{\gamma}$,

first normal stress difference: $N_1 = \tau_{11} - \tau_{22}$

complex viscosity: $\eta^* = \tau_{12}^*/\dot{\gamma}^* = \eta'(\omega) + i\eta(\omega)''$, $(i = \sqrt{-1})$

planar elongational viscosity: $\eta_e = (\tau_{11} - \tau_{22})/\dot{\epsilon}$.

3.4 5% PIB/C14 solution

3.4.1 Composition and preparation of fluid

The composition of the 5% PIB/C14 solution is the same as the solution used by the group of Armstrong and Brown ([4], [73], [93], [95]). The polyisobutylene (PIB) (Vistanex-L120, Exxon Chemical, $M_w \approx 1.0 \cdot 10^6$) is dissolved in tetradecane (C14) ($C_{14}H_{30}$, a linear hydrocarbon in an isomeric mixture of 95% purity). The fluid was prepared by cutting the polyisobutylene first in cubes of $\approx 0.5\,cm^3$, that were added in the appropriate amount to tetradecane in $1\,l$ bottles, while stirring with a magnetic stirrer at ambient temperature ($\approx 24\,°C$). After stirring during at least 5 days the bottles were rotated on a rolling machine for approximately one week to improve the homogeneity of the solution.

3.4.2 Determination of parameters of non-linear viscoelastic constitutive equations

An extensive rheological characterization of this fluid in simple shear has been presented by Quinzani et al. [73]. The solution used in the present study was prepared at our laboratory, and was tested in simple shear at the Rheometrics-RFS-II viscometer with a cone-plate geometry (diameter $50\,mm$, cone angle $0.0199\,rad$). Master curves at a reference temperature of $25\,°C$ were created after time-temperature superposition (Ferry [35]).

Shift factors a_T were determined from the plateau values of the steady shear viscosity $\eta(\dot{\gamma})$ at zero shear rate (η_0): $a_T = \eta_0(T)/\eta_0(T_{ref})$. Shift factors as function of $T^{-1} - T_0^{-1}$ could be fitted with an Arrhenius equation

$$log(a_T) = A(\frac{1}{T} - \frac{1}{T_0}) \tag{3.4}$$

with $A = \frac{\Delta H}{R}$, ΔH the 'flow activation energy', R the Boltzmann gas constant, and T_0 the reference temperature (in K). At the reference temperature the factor A was estimated with a least squares fit of Equation 3.4: $A = 2443K$ (see Figure 3.2).

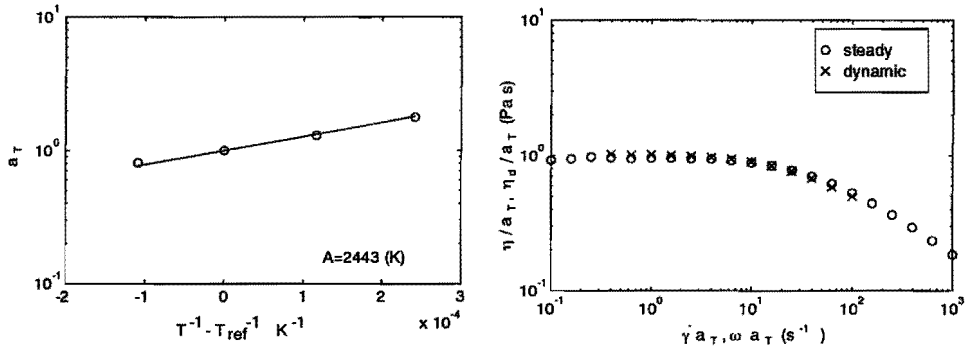

Figure 3.2: *Left: Arrhenius fit of the shift factors a_T. Right: comparison of steady shear viscosity $\eta(\dot{\gamma})$ (x) and dynamic viscosity $\eta_d(\omega)$ (o) to check the validity of the Cox-Merz rule for the 5%PIB/C14 solution.*

The empirical Cox-Merz rule is checked in Figure 3.2, where both steady shear viscosity as function of shear rate and the modulus of the complex viscosity η_d (the dynamic viscosity, $\eta_d = \sqrt{\eta'^2 + \eta''^2}$) have been plotted together. The rule is validated well in the measured range.

The upper four plots in Figure 3.3 show that the shifting procedure results in smooth master curves for both η and N_1 in steady shear, and η' and η'' in small amplitude oscillatory shear. The master curve for N_1 is shown for the range of shear rates where the data are not scattered too much. At shear rates lower than plotted the scatter was unacceptably large.

Two viscoelastic constitutive equations were fitted on these data: the Phan-Thien Tanner (PTT) equation with linear factor and the Giesekus equation. First, the Maxwell parameters $\{\eta_i, \lambda_i\}$ were determined by fitting the linear viscoelastic Maxwell model on the complex viscosity with a Levenbergh-Marquardt method ([119]). The components of the complex viscosity are for a single mode of a multi-mode Maxwell model:

$$\eta' = \sum_i^N \frac{\eta_i}{1 + \omega^2 {\lambda_i}^2} \tag{3.5}$$

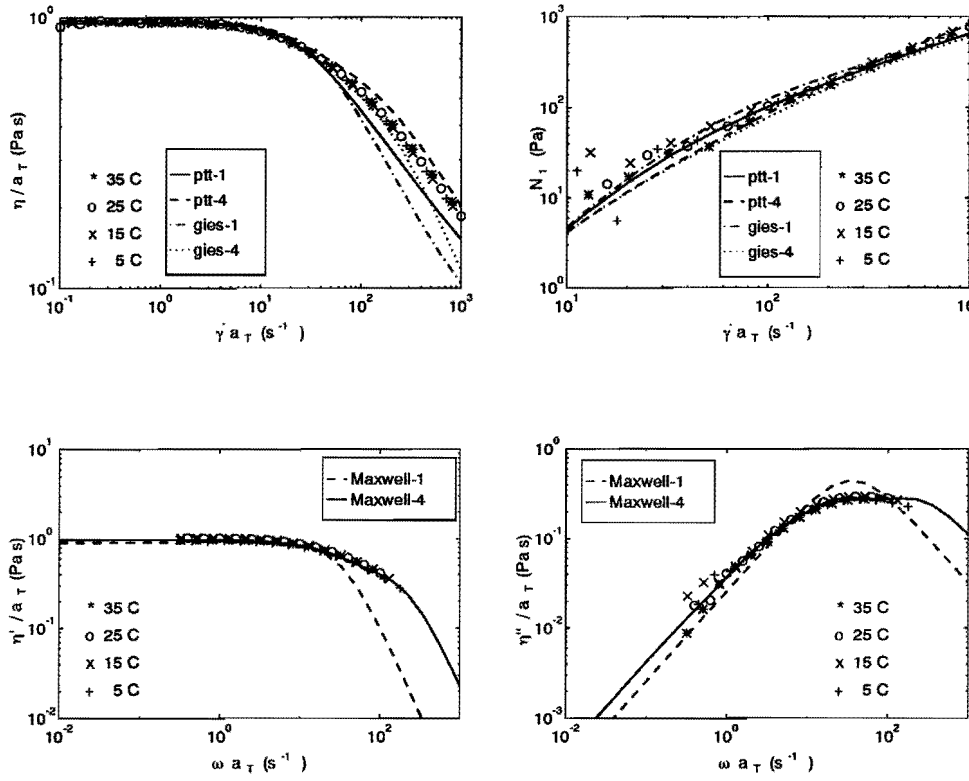

Figure 3.3: *Master curves at $T_{ref} = 25\,°C$ in simple shear flow for the 5% PIB/C14 solution. Top: steady shear viscosity $\eta(\dot{\gamma})$ and first normal stress difference $N_1(\dot{\gamma})$ together with four fitted constitutive equations. Bottom: complex viscosity with fitted Maxwell models.*

$$\eta'' = \sum_{i}^{N} \frac{\eta_i \lambda_i \omega^2}{1 + \omega^2 {\lambda_i}^2} \tag{3.6}$$

where i represents the number of the mode, and N is the number of modes. A one mode and a four mode model were fitted. Both results are plotted in Figure 3.3, and the parameter values are tabulated in Table 3.2.

Second, the non-linearity parameters in the non-linear viscoelastic PTT and Giesekus equations were determined by minimizing

$$q = \sum_j [(\frac{N_{1,j} - N_{1,j}^{exp}}{N_{1,j}^{exp}})^2 + (\frac{\eta_j - \eta_j^{exp}}{\eta_j^{exp}})^2] \tag{3.7}$$

where the index j denotes a shear rate value, $N_{1,j}$ denotes the first normal stress difference, η_j the shear viscosity and the superscript exp denotes the measured value. The residu q was

minimized with respect to the non-linearity parameters by variation of these parameters and evaluation of q. Stresses were calculated by solving numerically the non-linear system of equations for the constitutive equations in steady simple shear flow with a Gauss-Newton method as implemented in Matlab (The MathWorks Inc., function 'fsolve'). In case of the one mode fit, the solvent contribution to the extra-stress tensor ($2\eta_s \boldsymbol{D}$) was used to adjust the zero shear rate viscosity level (while the viscosity of tetradecane is $0.002\,Pa\,s$). In case of the four mode fit, the solvent viscosity was neglected ($\eta_s = 0$). All parameters of the non-linear viscoelastic equations used are tabulated in Table 3.2. For a multi-mode model the viscosity average value for the time constant, $\bar{\lambda}$, is defined by

$$\bar{\lambda} = \frac{\sum_i \eta_i \lambda_i}{\sum_i \eta_i}. \tag{3.8}$$

The four mode PTT model fits the measured viscosity best of all four fits that have been evaluated, see Figure 3.3, where the results for the two non-linear viscoelastic models are shown. The single mode models fit the steady shear viscosity equally well as the four mode models for shear rates up to $40\,s^{-1}$, i.e. until shear thinning has just started. For higher shear rates the single mode Giesekus model predicts a too strong shear thinning and its prediction of the viscosity is worst of all four fits. The two four mode fits are both more accurate than the one mode PTT model for shear rates in between 80 and $500\,s^{-1}$. At higher shear rates the four mode Giesekus model is again too shear thinning. Although the same holds for the one mode PTT model, the effect is less serious and its prediction of the viscosity still agrees fairly well with the measured data.

Although differences between the fits are small, the normal stress difference N_1 is fitted best by the one mode PTT model for shear rates below $200\,s^{-1}$, while for higher shear rates the prediction of the four mode PTT model is best. The differences between results for the Giesekus model are larger.

Quinzani [73] has characterized the rheology of this solution in simple shear flow, and our results can be compared with her results. In Figure 3.4 our steady shear viscosity and

	Maxwell parameters		PTT		Giesekus	
n	$\eta_i\,[Pa\,s]$	$\lambda_i\,[s]$	ξ	ϵ	α	$\eta_s\,[Pa\,s]$
1	$9.28 \cdot 10^{-1}$	$2.90 \cdot 10^{-2}$	0.0	0.39	0.21	0.05
4	$4.43 \cdot 10^{-1}$	$4.30 \cdot 10^{-3}$	0.0	0.39	0.40	0.0
	$4.40 \cdot 10^{-1}$	$3.70 \cdot 10^{-2}$				
	$9.20 \cdot 10^{-2}$	$2.03 \cdot 10^{-1}$				
	$1.70 \cdot 10^{-3}$	$3.00 \cdot 10^{0}$				

Table 3.2: *Parameter values for 1−mode and 4−mode (n: number of modes) non-linear viscoelastic constitutive models at the reference temperature of 25°C in case of the 5% PIB/C14 solution (zero-shear viscosity averaged time constant of 4 mode fit $\bar{\lambda} = 4.31 \cdot 10^{-2}\,s$).*

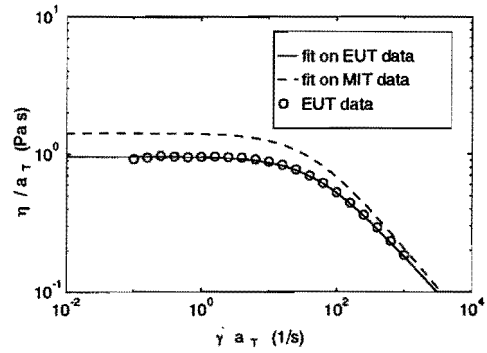

Figure 3.4: *Comparison of our measured steady shear viscosity and Carreau-Yasuda fit with the Carreau-Yasuda fit of Quinzani [93] for 5% PIB/C14.*

the Carreau-Yasuda fit of Quinzani ($n = 0.4, \eta_{cy} = 1.424\,Pa\,s, a = 1, \lambda_{cy} = 0.024\,s$) are plotted together. It clearly reveals differences between the fluids. The zero shear viscosity at $25°C$ is in our measurements $0.96\,Pa\,s$, while Quinzani's result is $1.424\,Pa\,s$. Our data proved to be reproducible with each new batch of fluid made, and the large difference between our zero shear viscosity and Quinzani's is probably caused by differences in the molecular weight distributions of the PIB used. Quinzani also used the Giesekus and PTT equations to describe the rheological data. The average time constant of the four mode Maxwell fit was $0.060\,s$ in that study, which is 40% larger than our value. Quinzani initially assumed that the parameter ϵ in the PTT equation was small: $\epsilon << 1$ (it could thus be neglected when fitting material functions in simple shear flow) and she obtained $\xi = 0.13$ to fit the steady shear viscosity and first normal stress coefficient with a four mode model. However, measurements of the stresses along the center line in a $4:1$ contraction made the use of a non-zero parameter ϵ necessary, the best fitting value (with $\xi = 0.13$) was 0.25. The effect of this non-zero value for ϵ on the fit of the material functions in steady simple shear is small .

In the present study, the parameter ξ in the PTT equation has not been used, since it did not improve any of the fits. Moreover, a non-zero ξ parameter is known to cause oscillations in stresses during start-up of steady shear (see Section 3.6.3). We also aimed to fit the data with as less parameters as possible. Therefore the four-mode equations were fitted with a single value for ϵ or α for all modes.

3.4.3 Start-up of simple shear flow

Shear stresses have been measured during start-up of simple shear flow, for four values of the final shear rate $\dot{\gamma}_0$: $10, 30, 60, 100\,(1/s)$ [1]. The transient viscosity function η^+ is defined

[1]Unfortunately, no reliable transient measurement of normal stress was possible, due to a too strong oscillation in the normal force that depended on the rotation frequency of the plate.

as

$$\eta^+ = \frac{\tau}{\dot{\gamma}_0}. \tag{3.9}$$

The measured data have been compared with model predictions with parameters from Table 3.2. Stresses were calculated with a fourth and fifth order Runge-Kutta integration, with automatic step size control (as implemented in Matlab, The MathWorks Inc.). To avoid the singularity in the stresses at $t = 0\,s$, a ramp of $0.02\,s$ has been used in the shear rate history during the calculations. To improve the agreement (on the double logarithmic plot) with measured data at times below $< 0.05\,s$, shearing was started in the computations at $t = 0.01\,s$. The results are shown in Figure 3.5 (single and four mode PTT model and single and four modes Giesekus model).

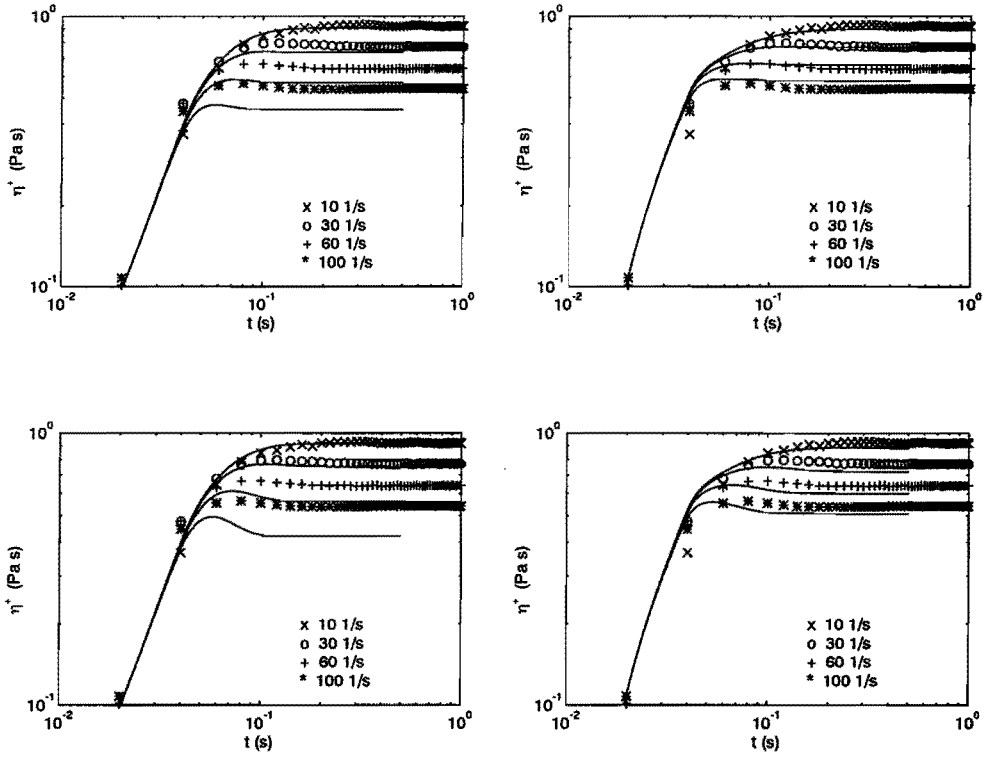

Figure 3.5: *Viscosity η^+ (during start-up of steady simple shear flow) at $T = 25°C$ for the 5% PIB/C14 solution. Top: single mode (left) and four modes (right) PTT model. Bottom: one mode (left) and four modes (right) Giesekus equation.*

Differences between computations and measurements are mainly due to differences in the steady state value for η. This steady state value is predicted accurately by all four

models at shear rates of 10 and $30\,s^{-1}$. At higher shear rates (60, $100\,s^{-1}$) , however, both four mode models proved to be more accurate than the single mode models. It also appears that for the two highest shear rates all models predict an overshoot, that is largest in case of the Giesekus models. A small overshoot is also present in the measured data and the PTT models have an overshoot that is closer to the measured data than in case of the Giesekus models.

3.4.4 Predictions in planar elongational flow

Model predictions in steady planar elongation are compared in Figure 3.6. Such experiments are practical impossible or unreliable for (relatively) low viscosity fluids like the solutions in this study (see Section 1.1). The model predictions show, however, the typical behavior of the models in elongational flows and the influence of the model parameters. All models show elongation thickening behavior, i.e. an increase in elongational viscosity with increasing elongation rate. The effect is controlled by the value of the non-linearity parameters ϵ and α in the PTT and Giesekus model respectively. The smaller these values, the stronger the elongation thickening (in the limit $\epsilon \rightarrow 0$ or $\alpha \rightarrow 0$ the models change into the UCM model that has infinite extensional stresses above a certain extension rate). The 1−mode Giesekus model possesses a higher elongational viscosity than the other models: this is due to the relatively low value of the parameter α, see Table 3.2.

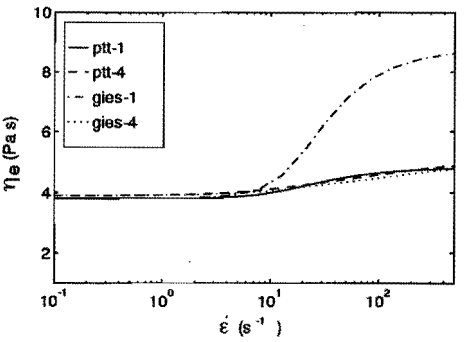

Figure 3.6: *Predictions in planar elongation of viscoelastic constitutive equations with parameter values fitted in simple shear flow for the* $5\%PIB/C14$ *solution.*

3.5 9% PIB/C14 solution

3.5.1 Preparation and composition of fluid

This fluid was prepared identically to the 5% PIB/C14 solution, with the same constituents, but now with a different PIB concentration of 9% (w/w).

3.5.2 Determination of parameters of non-linear viscoelastic constitutive equations

The fitting procedure has been described in Section 3.4. The same constitutive equations have been used, and the parameters found are tabulated in Table 3.3.

	Maxwell parameters		PTT		Giesekus	
n	$\eta_i\,[Pa\,s]$	$\lambda_i\,[s]$	ξ	ϵ	α	$\eta_s\,[Pa\,s]$
1	$1.63 \cdot 10^{1}$	$9.28 \cdot 10^{-2}$	0.0	0.75	0.55	0.0
4	$2.99 \cdot 10^{0}$	$7.20 \cdot 10^{-3}$	0.0	0.75	0.55	0.0
	$7.65 \cdot 10^{0}$	$6.40 \cdot 10^{-2}$				
	$7.62 \cdot 10^{0}$	$4.40 \cdot 10^{-1}$				
	$8.76 \cdot 10^{-1}$	$3.36 \cdot 10^{0}$				

Table 3.3: *Parameter values for 1−mode and 4−mode (n: number of modes) non-linear viscoelastic constitutive models at the reference temperature of 25°C in case of the 9% PIB/C14 solution*($\bar{\lambda} = 3.56 \cdot 10^{-1}\,s$).

Time-temperature superposition resulted in smooth master curves for $\eta(\dot{\gamma})$ and $N_1(\dot{\gamma})$ in steady simple shear and for the complex viscosity defined by $\eta'(\omega)$ and $\eta''(\omega)$ (see Figure 3.8). The Arrhenius fit of the shift factors a_T is plotted in Figure 3.7. The data for N_1 show relatively large scatter for shear rates below $10\,s^{-1}$, due to experimental difficulties of normal stress measurements. In Figure 3.7 also the Cox-Merz rule is checked, which is shown to be valid in the range of shear rates and angular frequencies measured.

The Giesekus model with four modes fits the steady shear material functions best over the whole shear rate range, the result is excellent (Figure 3.8). Differences are small between all models. As in case of the 5% PIB/C14 solution the PTT and Giesekus model have been fitted for both a one and a four mode version.

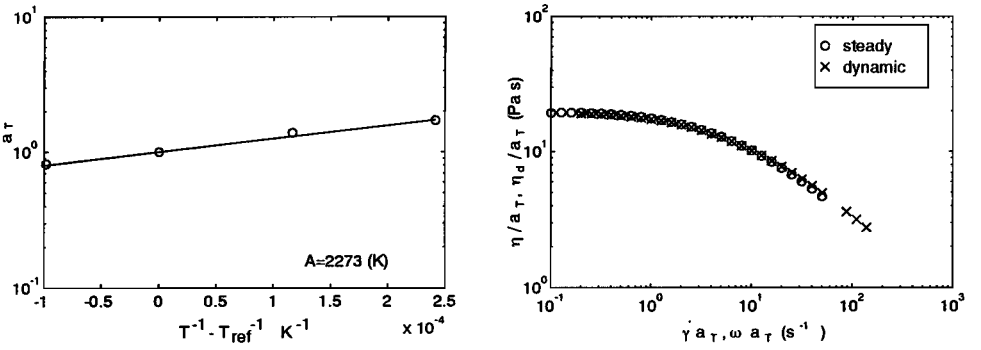

Figure 3.7: *Left: Arrhenius fit of the shift factors a_T. Right: comparison of steady shear viscosity $\eta(\dot{\gamma})$ (x) and dynamic viscosity $\eta_d(\omega)$ (o) to check the validity of the Cox-Merz rule for the 9%PIB/C14 solution.*

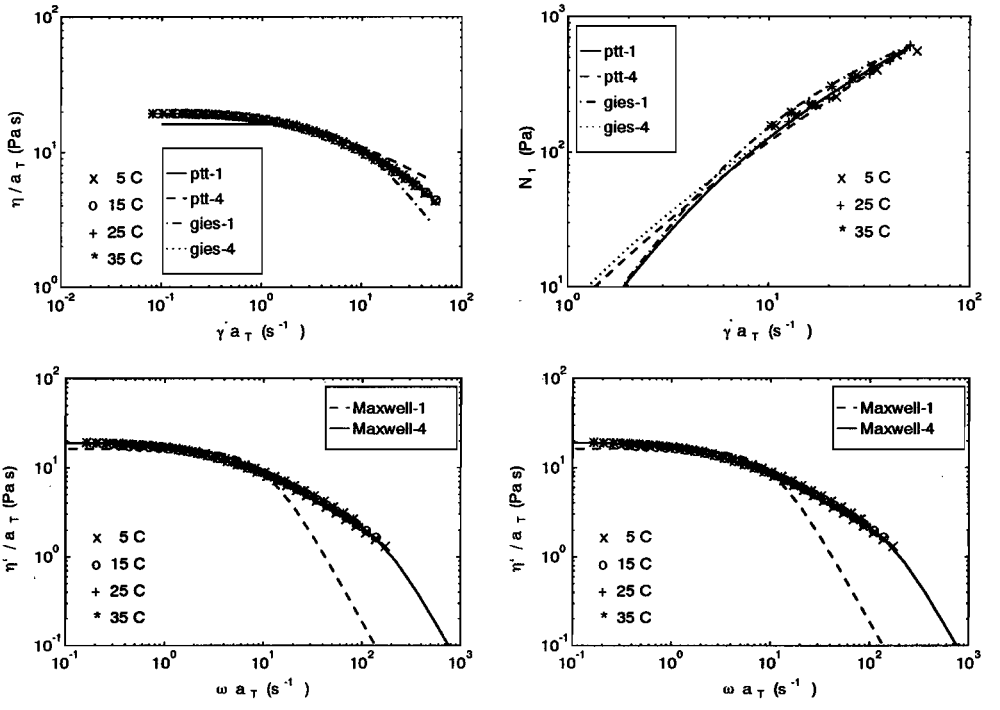

Figure 3.8: *Master curves at $T_{ref} = 25\,°C$ in simple shear flow for the 9% PIB/C14 solution. Top: steady shear viscosity $\eta(\dot{\gamma})$ and first normal stress difference $N_1(\dot{\gamma})$ together with four fitted models, Bottom: complex viscosity with fitted Maxwell models (n = number of modes).*

3.5.3 Start-up of simple shear flow

Shear stresses have been measured during start-up of simple shear flow, for three values of the final shear rate $\dot{\gamma}_0$: $10, 30, 100\,(1/s)$. The measured data for η^+ have been compared with the model predictions (computed as described in Subsection 3.4.3 with model parameters as in Table 3.3). The results are shown for all cases in Figure 3.9 (single and four mode PTT model and single and four modes Giesekus model).

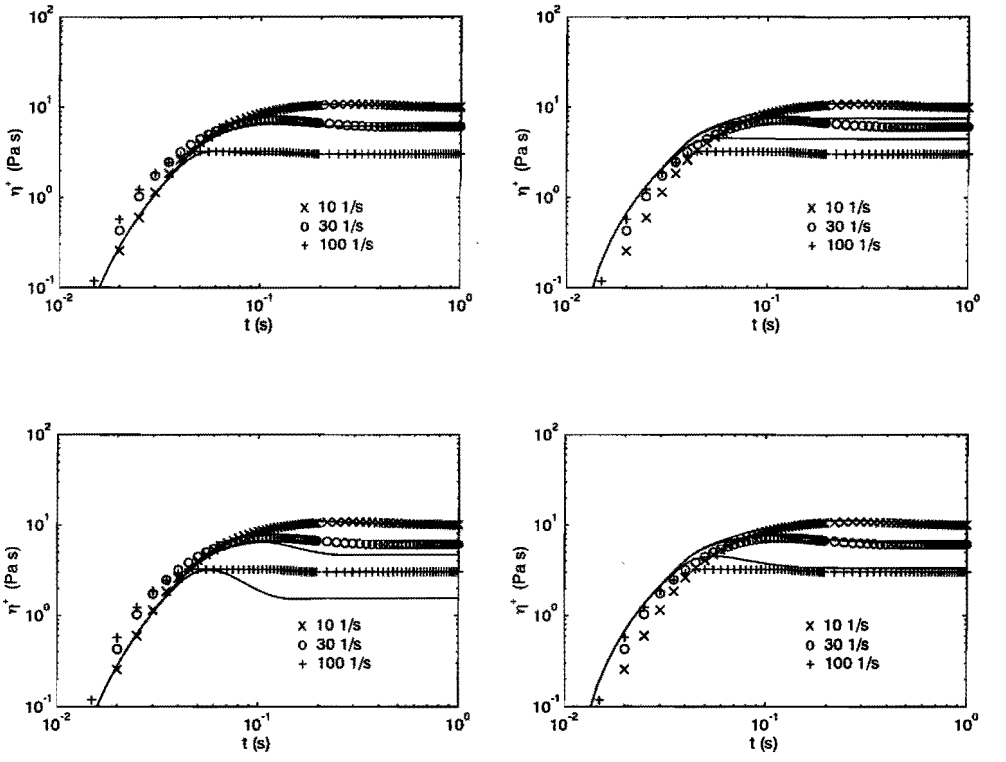

Figure 3.9: *Viscosity η^+ (during start-up of steady simple shear flow) at $T = 25°C$ for the 9% PIB/C14 solution. Top: single mode (left) and four modes (right) PTT model. Bottom: single mode (left) and four modes (right) Giesekus equation.*

The start-up viscosity η^+ is described excellently by the one mode PTT equation, including the small overshoot at $\dot{\gamma}_0 = 30\,s^{-1}$. The single mode PTT and the four mode Giesekus model both fit the steady shear viscosity accurately in the range of shear rates used in the start-up experiments, which is in agreement with the fits of the steady shear viscosity function. The Giesekus models have a too large overshoot compared to the measured data.

3.5.4 Predictions in planar elongational flow

The elongational viscosity in planar elongation is plotted for the four models in figure 3.10. The plateau at the lowest deformation rates differs for the one and four mode models, since the elongational viscosity then is determined by the zero shear viscosity. For the parameter values fitted above, both single and multi-mode versions of each model predict *elongation thinning* behavior. This is not in agreement with the elongational thickening behavior generally found for polymeric liquids. Fitting the PTT model with $\xi = 0.20, \epsilon = 0.35$ surmounts this (possibly) non-realistic feature because it predicts weak elongational thickening, while keeping good agreement in simple shear. However, it leads to unrealistic oscillations in the shear stress after start-up of steady shear (see Section 3.6.3) and computations in Chapter 4 proved to be impossible when the PTT model with $\xi \neq 0$ was used. Therefore, this fit has not been worked out here.

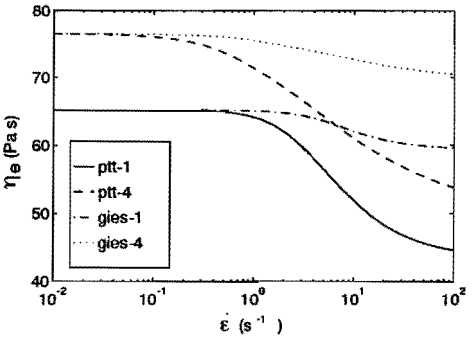

Figure 3.10: *Predictions in planar elongation of viscoelastic constitutive equations with parameter values fitted in simple shear flow for the 9%PIB/C14 solution.*

3.6 S1 solution

The standard fluid S1 ('S' of 'University of Strathclyde') was introduced in 1993 in the international project 'The rheometry of polymers: from the solution to the melt'. The aim of this project is to create a test fluid whose rheological behavior could be changed (by changing the concentration of its constituents) in a wide range ('from solution to the melt'). S1, a solution of PIB in Decalin and polybutene oil, should be the starting point of the project. Its composition was chosen such that the fluid could be used in (most of) the existing extensional viscometers. First results of the project were presented in 1993 at a meeting in Fontevraud ([113]).

In the present study only measurements in simple shear flow are reported since the toxicological, chemical and physical properties (mainly evaporation danger) of the Decalin

require adjustments of our complex flow system. The material functions in steady simple shear of the 9% PIB/C14 solution, as described in the previous Section, will appear to be close to those of the S1 fluid. The measurements on the S1 fluid will be compared with reference data to show the accuracy of our measurements.

3.6.1 Composition of fluid

S1 is a ternary solution of 2.5%(w/w) PIB in a mixed solvent of 47.5%(w/w) Decalin (decahydronaphtalene) and 50%(w/w) polybutene oil (PBO). The PIB in this solution is Vistanex-L140 (Exxon Chem.) with a weight average molecular weight $M_w \approx 1.2 \cdot 10^6$ (Hudson and Ferguson [54]). The PBO was Hyvis 10 (BP Chem.). The fluid used in the present study was a sample ($0.5\,l$) of the original batch for the Fontevraud-meeting, which was donated by Ferguson.

3.6.2 Determination of parameters of non-linear viscoelastic constitutive equations

Master curves of the material functions in steady and oscillatory simple shear are presented in Figure 3.13. The shift factors and their Arrhenius fit are plotted in Figure 3.11 (data at the lowest temperature ($T = 5\,°C$) did not fit well on the Arrhenius equation, as is seen in this figure).

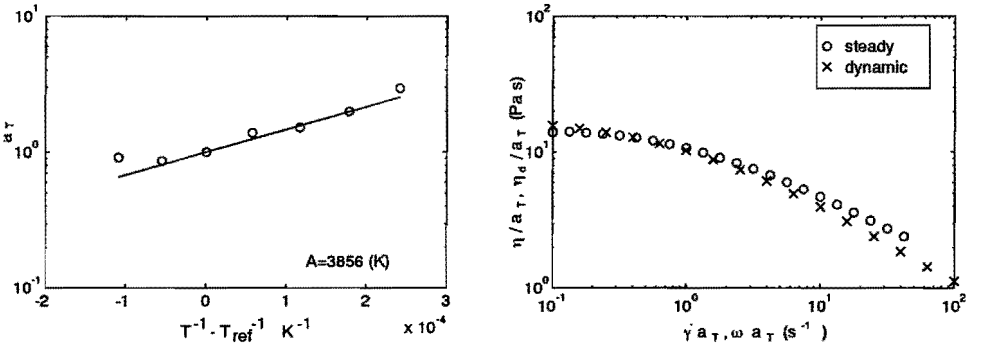

Figure 3.11: *Left: Arrhenius fit of the shift factors a_T. Right: comparison of steady shear viscosity $\eta(\dot{\gamma})$ (x) and dynamic viscosity $\eta_d(\omega)$ (o) to check the validity of the Cox-Merz rule for the S1 solution.*

The Cox-Merz rule has been checked in Figure 3.11: it shows that the rule is not validated. The modulus of the complex viscosity is lower than the steady shear viscosity as soon as the shear thinning starts. This effect is also reported by Ferguson and Hudson [34].

Good agreement is found between our data and those of Ferguson and Hudson [34], which have been published as reference data. Some differences exist, as is discussed next.

The fit of the Carreau-Yasuda equation made by Ferguson and Hudson on their data at $T = 25\,°C$ is shifted a little compared with our fit (parameters in Table 3.1), as shown in Figure 3.12. It does not represent the optimal fit for our measured data. Differences are small however.

Ferguson and Hudson fitted the relation between shear stress τ and first normal stress difference N_1 with $N_1 = a\tau^2$, and found $a = 0.0577\,Pa^{-1}$. For our data, with the factor 2 in the exponent of τ, the factor a was fitted: $a = 0.0580\,Pa^{-1}$, i.e. excellent agreement with the result of Ferguson and Hudson. The fit of our data is shown in Figure 3.12 (in the case that both the exponent and the factor a were fitted, the result was $N_1 = 0.0483\tau^{2.044}$). It is noted that the literature data for N_1 were obtained in a larger interval ($1 < N_1 < 10^4\,Pa$) than was possible in our experiments.

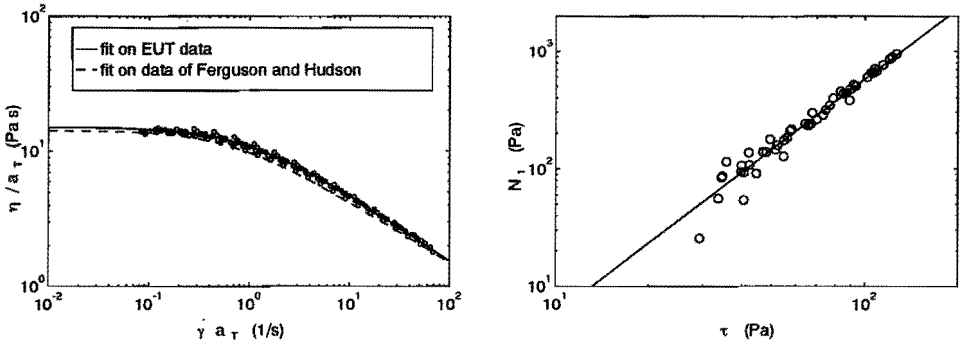

Figure 3.12: *Left: comparison of our Carreau-Yasuda fit of steady shear viscosity at $T = 25\,°C$ and the fit of Ferguson and Hudson, together with our measured data. Right: N_1 as function of shear stress (τ) together with fitted relation $N_1 = 0.058\tau^2$.*

The four mode Giesekus model fits best in steady simple shear, the agreement for the viscosity is excellent. Again, both PTT and Giesekus model have been fitted in a single mode and a multi-mode version. The single mode PTT model fits the steady shear material functions better than the single mode Giesekus model, while the four mode Giesekus model fits both functions better than the four mode PTT model. Parameters are tabulated in Table 3.4. It is noted that the four mode PTT fit was made with a small value for ϵ ($= 0.05$) and a non-zero value for ξ ($= 0.075$). In this way, the steady shear viscosity could be fit excellently (both ϵ and ξ control the shear thinning behavior). The fit of N_1 is poor for all models, however. The interesting aspect of this fit is its strong elongational thickening behavior (see Subsection 3.6.4) caused by the small value for ϵ. The disadvantage of $\xi \neq 0$ is the occurrence of oscillations in the stresses during start-up of simple shear, that are physically unrealistic since they have never been observed in experiments (Larson [70]) and also not for S1, as is shown in the next subsection.

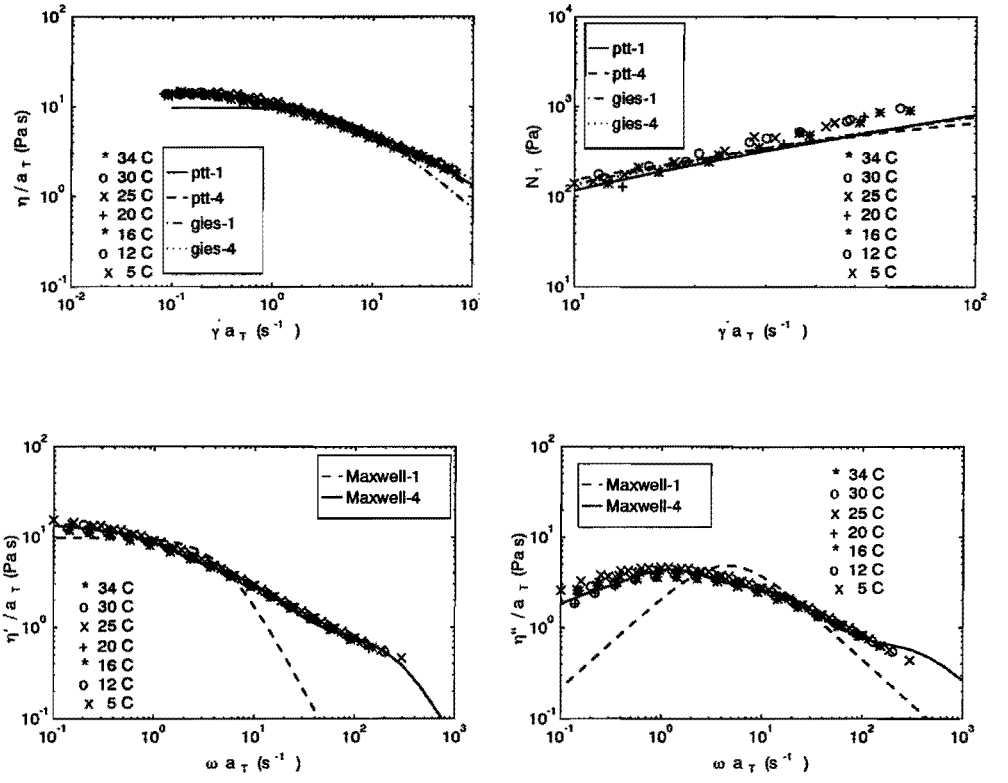

Figure 3.13: *Master curves at $T_{ref} = 25\,°C$ in simple shear flow for the S1 solution. Top: steady shear viscosity $\eta(\dot{\gamma})$ and first normal stress difference $N_1(\dot{\gamma})$ together with four fitted constitutive equations. Bottom: complex viscosity with fitted Maxwell models.*

	Maxwell parameters		PTT		Giesekus	
n	$\eta_i\,[Pa\,s]$	$\lambda_i\,[s]$	ξ	ϵ	α	$\eta_s\,[Pa\,s]$
1	$9.77 \cdot 10^0$	$2.19 \cdot 10^{-1}$	0.0	0.35	0.21	0.0
4	$0.81 \cdot 10^0$	$3.60 \cdot 10^{-3}$	0.075	0.05	0.21	0.0
	$3.33 \cdot 10^0$	$7.96 \cdot 10^{-2}$				
	$7.55 \cdot 10^0$	$8.19 \cdot 10^{-1}$				
	$2.51 \cdot 10^0$	$6.67 \cdot 10^0$				

Table 3.4: *Parameter values for 1−mode and 4−mode (n: number of modes) non-linear viscoelastic constitutive models at the reference temperature of 25°C in case of the standard fluid S1 ($\bar{\lambda} = 1.63\,s$).*

3.6.3 Start-up of simple shear flow

Shear stresses have been measured during start-up of simple shear flow for four values of the final shear rate: $10, 30, 60, 100\,1/s$. The measured data have been compared with the model predictions (computed as described in Subsection 3.4.3) with model parameters as in Table 3.4 (Figure 3.14). The four mode PTT equation with $\xi \neq 0$ results in strong oscillations in the stresses after start-up of steady shear.

The four modes Giesekus model describes the start-up viscosity η^+ well. The overshoot in the viscosity is described quantitatively well at the two lowest shear rates ($\dot{\gamma}_0 = 10, 30\,s^{-1}$), and qualitatively at the two highest shear rates ($\dot{\gamma}_0 = 60, 100\,s^{-1}$). The other models fail: the single mode PTT equation has a to small overshoot, and the single mode Giesekus model a too large one. Moreover, the steady state viscosity is, in both cases, too low and this effect is strongest for the single mode PTT (compared with the bottom left plot in Figure 3.13). The four mode PTT equation with $\xi = 0.075$ suggests strong oscillations after start-up of steady shear that are not present in any of the measured data.

3.6.4 Predictions in planar elongational flow

The elongational viscosity in steady planar elongation is plotted for the four model fits in Figure 3.15. The four mode PTT fit has the strongest elongational thickening behavior, again due to the small value for ϵ.

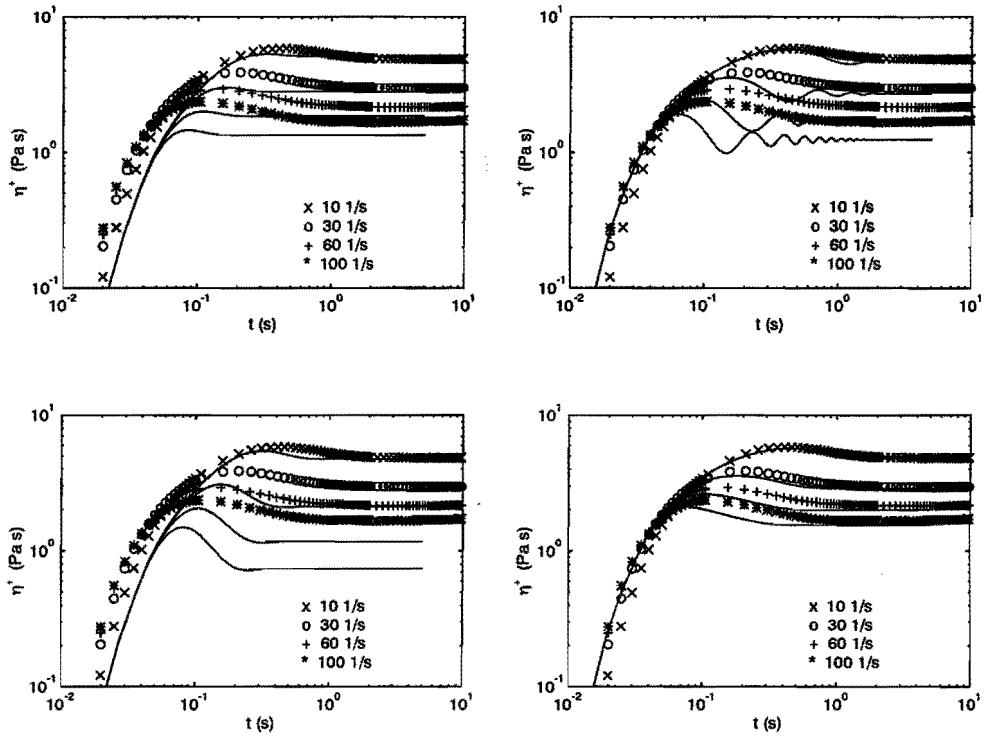

Figure 3.14: *Measured viscosity η^+ (during start-up of steady simple shear flow) at $T = 25°C$ for the S1 solution. Top: one mode (left) and four modes (right) PTT equation. Bottom: one mode (left) and four modes (right) Giesekus equation.*

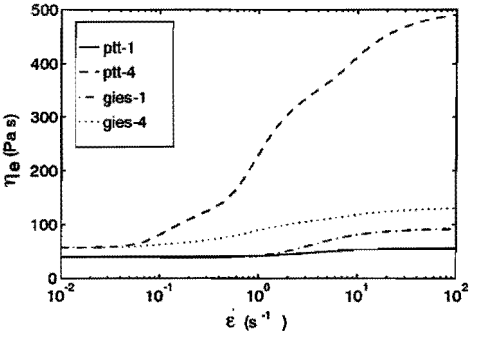

Figure 3.15: *Predictions in planar elongation of viscoelastic constitutive equations with parameter values fitted in simple shear flow for S1.*

3.7 LDPE melt

3.7.1 Characteristics of the LDPE

The LDPE is the same as used by Tas [107]: a commercial grade Stamylan LD 2008XC43 (DSM). Some of its characteristics are tabulated in Table 3.5.

Melt index (ISO 1133(A/4))	M_n	M_w	M_z	$\rho\,[kg/m^3]$ (ISO 1183(A))	$T_c\,[°C]$
8	$1.30 \cdot 10^4$	$1.55 \cdot 10^5$	$7.8 \cdot 10^5$	$9.2 \cdot 10^2$	98.6

Table 3.5: *Characteristics of LDPE used (Stamylan LD 2008XC43, (DSM Chem.)). M_n: number averaged molecular weight, M_w: weight average molecular weight, M_z: z-averaged molecular weight, ρ: density, T_c: cristallization temperature.*

3.7.2 Determination of parameters of non-linear viscoelastic constitutive equations

Tas [107] has performed an extensive rheological characterization in simple shear flow and in both uniaxial and biaxial extensional flow. Four non-linear viscoelastic constitutive equations were fitted (Leonov, Wagner, PTT-B and Giesekus) with eight modes. The result was that Giesekus and PTT models fitted the data both fairly well. Only the relaxation of first normal stress difference after cessation of steady shear flow distinguished between these two models: the PTT model agreed closer with the measured data. It appeared necessary to use the ξ parameter in the PTT model to obtain optimal agreement with data in simple shear and in extension simultaneously. The parameter values of the eight modes PTT and Giesekus fits are listed in Table 3.6.

Here, also a *four mode* fit was made for two models, PTT and Giesekus, to reduce the number of unknowns in the computations in Chapter 5. In Table 3.6 the model parameters are listed, and in Figures 3.16 the fits are plotted together with experimental data of Tas [107] [2]. The eight mode fit agrees excellently with both the complex modulus and the material functions in steady simple shear $\eta(\dot{\gamma})$ and $N_1(\dot{\gamma})$. The four mode fits are a little less accurate, but good agreement is kept. Unfortunately, data of steady shear measurements are available only in a relatively small shear rate interval.

[2] For melts usually the complex modulus $G^* = \frac{\tau^*}{\gamma^*}$ is shown instead of η^*.

	Maxwell parameters		PTT		Giesekus	
n	$\eta_i\,[Pa\,s]$	$\lambda_i\,[s]$	ξ	ϵ	α	$\eta_s\,[Pa\,s]$
4	$1.65 \cdot 10^3$	$1.00 \cdot 10^0$	0.1	0.1	0.25	0.0
	$6.60 \cdot 10^2$	$3.16 \cdot 10^{-2}$				
	$1.37 \cdot 10^2$	$1.00 \cdot 10^{-3}$				
	$8.50 \cdot 10^0$	$3.16 \cdot 10^{-5}$				
8	$9.28 \cdot 10^0$	$4.28 \cdot 10^{-5}$	0.15	0.05	0.38	0.0
	$1.90 \cdot 10^1$	$2.07 \cdot 10^{-4}$				
	$7.21 \cdot 10^1$	$1.30 \cdot 10^{-3}$				
	$2.20 \cdot 10^2$	$9.00 \cdot 10^{-3}$				
	$5.07 \cdot 10^2$	$5.69 \cdot 10^{-2}$				
	$8.25 \cdot 10^2$	$3.50 \cdot 10^{-1}$				
	$5.84 \cdot 10^2$	$1.82 \cdot 10^0$				
	$1.23 \cdot 10^2$	$9.94 \cdot 10^0$				

Table 3.6: *Parameter values for 4−mode and 8−mode (n: number of modes) non-linear viscoelastic constitutive models in case of the LDPE at $T = 190°C$ ($\bar{\lambda} = 1.10\,s$).*

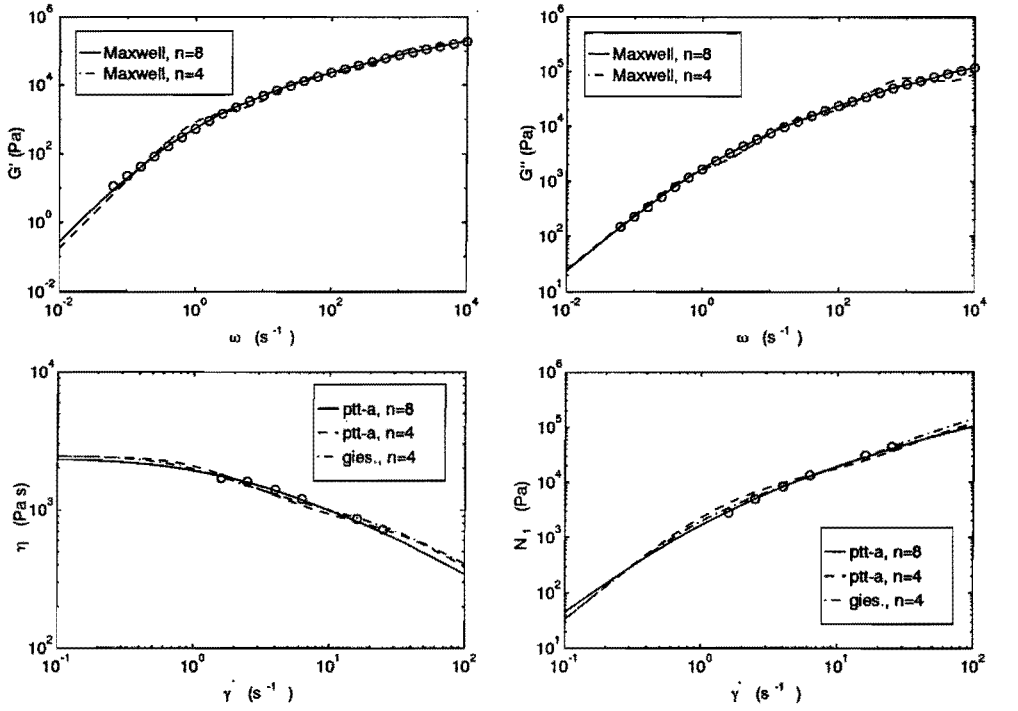

Figure 3.16: *Rheological data for LDPE melt at $T = 190°C$. Top: complex modulus with fitted Maxwell models. Bottom: steady shear viscosity $\eta(\dot{\gamma})$ and first normal stress difference $N_1(\dot{\gamma})$ with fitted curves of non-linear viscoelastic constitutive equations.*

3.7.3 Predictions in planar elongational flow

With the eight mode PTT, four mode PTT and four mode Giesekus model the elongational viscosity has been computed, the results are shown in Figure 3.17. The bumps in the curves are caused by the different modes. The typical behavior of the PTT model with exponential factor is found: the elongational viscosity shows a maximum.

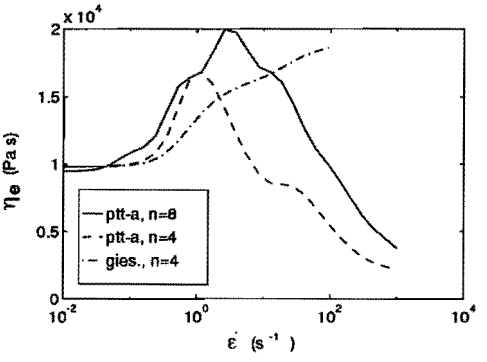

Figure 3.17: *Predictions with fitted non-linear viscoelastic constitutive models for the planar elongational viscosity for LDPE melt at* $T = 190°C$.

3.8 Conclusions and discussion

Three polyisobutylene solutions (referred to as 5% PIB/C14, 9% PIB/C14 and S1) have been rheologically characterized in steady simple shear flow and in small amplitude oscillatory shear flow. Master curves for the material functions $\eta(\dot{\gamma}), N_1(\dot{\gamma})$ and $\eta^*(\omega)$ were created using the principle of time-temperature superposition. The shift factors could be fitted with an Arrhenius equation (except data for the S1 solution at $T = 5\,°C$).

The steady shear viscosity could be fitted excellently for all three solutions with a Carreau-Yasuda equation. The material functions in steady simple shear of the 9% PIB/C14 and S1 solution are roughly similar, while the values for the stresses for the 5% PIB/C14 solution are approximately one order of magnitude lower at each shear rate compared to the other two fluids. The empirical Cox-Merz rule has been validated for the 5% PIB/C14 and 9% PIB/C14 solution, while in case of the S1 solution this was not the case: the modulus of the complex viscosity was lower than the steady shear viscosity as soon as the shear thinning started. This effect for S1 has also been reported in literature (Ferguson and Hudson [34]).

Two non-linear viscoelastic equations of the differential type, the PTT equation with linear factor and the Giesekus equation, were fitted on the master curves for both a single and a four mode version. The results are summarized in Table 3.7. Overall, the four mode

Material function	5% PIB/C14	9% PIB/C14	S1
$\eta(\dot{\gamma})$	PTT-4 Gies-4	Gies-4 PTT-1	Gies-4 PTT-1
$N_1(\dot{\gamma})$	PTT-4 PTT-1	Gies-4 PTT-1	-
$\eta^+(\dot{\gamma}_0, t)$	PTT-4 Gies-4	PTT-1 Gies-4	Gies-4

Table 3.7: *Evaluation of the non-linear viscoelastic constitutive equations that have been fitted for the three polyisobutylene solutions. For each material function and each solution the best fitting model is listed; in case two models were both accurate two models are listed, with the first listed model giving the most accurate fit (the difference can be small). If no accurate fit could be made,no model is listed. Abbreviations: PTT-1,4 = one, four mode PTT, and Gies-1,4 = one, four mode Giesekus model.*

Giesekus equation is the most satisfactory model, since it fits best the material functions in steady simple shear for all three solutions, except $N_1(\dot{\gamma})$ for 5% PIB/C14. The four mode PTT model and the single mode PTT model are often accurate too. The single mode Giesekus equation clearly fails, such that it is not even mentioned at all in Table 3.7.

The parameters of the best fitting models predict a planar elongational viscosity that is only moderately elongational thickening or even elongational thinning. This is due to the relatively large value for both α ($0.21 \leq \alpha \leq 0.55$) and ϵ ($0.35 \leq \epsilon \leq 0.75$).

In case of the S1 fluid a quantitative comparison with reference data from literature was possible, since we used a sample of the same batch as in the reference experiments (Ferguson and Hudson [34]). Good agreement is found for the steady shear viscosity, though the reference data are a little shifted compared with our data. The relation between steady shear stress and first normal stress difference in our measurements appeared to be described with exactly the same equation as in the reference experiments, which demonstrated the accuracy of our measurements.

In case of LDPE, both a four mode PTT and a four mode Giesekus equation fit well the complex modulus and the material functions in steady simple shear.

Chapter 4

Steady flow of polyisobutylene solutions past a cylinder

4.1 Introduction

The planar flow of two polyisobutylene solutions past a confined cylinder has been investigated by means of a comparison of finite element (FEM) computations with pointwise measurements of velocities (with LDA) and stresses (with FIB) (these experimental methods have been described in Chapter 2). The motivation for this choice has been given in Sections 1.1 and 1.5.

The model fluids used are the 5% PIB/C14 and 9% PIB/C14 solutions, that have been rheologically characterized in simple shear in Chapter 3.

In case of 5% PIB/C14, two types of geometric variants are studied: the cylinder placed symmetrically and asymmetrically between two parallel plates. In case of 9% PIB/C14 only the symmetrically confined cylinder has been considered.

The Phan-Thien Tanner (PTT) constitutive equation of type B (Section 1.2) has been used to describe the viscoelastic behavior of the model fluid since it fitted data in steady shear best (see Table 3.7). To analyze the sensitivity of the flow for the precise form of the viscoelastic model, both a single and a four mode fit have been used. For the same reason, at the highest Deborah number a four mode Giesekus model has been applied as well. The separate influence of shear thinning on the velocity field has been analyzed by means of a generalized Newtonian model (Carreau-Yasuda).

The flow loop and flow cell are described in Section 4.2. Subsequently, the results for the flow of 5% PIB/C14 past the symmetrically confined cylinder are presented (Section 4.3), followed by those for the asymmetrically confined cylinder (Section 4.4). The flow of 9% PIB/C14 past a symmetrically confined cylinder is analyzed in Section 4.5. Finally, Section 4.6 contains a discussion on the results and conclusions are made in Section 4.7.

4.2 Flow loop and flow cell

The flow loop is plotted in Figure 4.1 . In the closed flow loop, approximately 2.5 l PIB/C14 solution is pumped continuously from a (glass) reservoir by a sanitary rotary pump (Nakamura, *RO-10-VT*) that is driven by a frequency controlled motor (Elsto, *100-L6*) through flexible tubes (with inner walls made of Viton or NBR rubber) and the flow cell. The flow cell is made of PMMA with special, extremely low birefringent glass windows (Schott, SF-57) that enable accurate FIB measurements in the low range of stresses ($< 10^3\ Pa$) which exist in the PIB/C14 solution during flow. These windows were polished and coated with a single-λ antireflection coating (TiO_2) to prevent stain formation. During the experiments, samples of fluid were tested regularly on a Rheometrics-RFS-II viscometer and no significant changes were found.

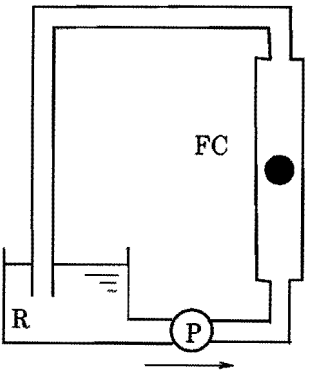

Figure 4.1: *Flow loop used in the LDA and FIB experiments: approximately 2.5 l of PIB/C14 solution is pumped through the flow cell. Connections between pump (P) , flow cell (F) and reservoir (R) are made by flexible tubes (for details see text).*

4.3 Flow of 5 % PIB/C14 solution past a symmetrically confined cylinder

4.3.1 Introduction

The flow of the 5% PIB/C14 solution past a symmetrically confined cylinder has been investigated most extensively. The geometry is defined as in Figure 4.2. In the sequel, the numerical method, details of the flow conditions, the measurement procedures and the results are discussed.

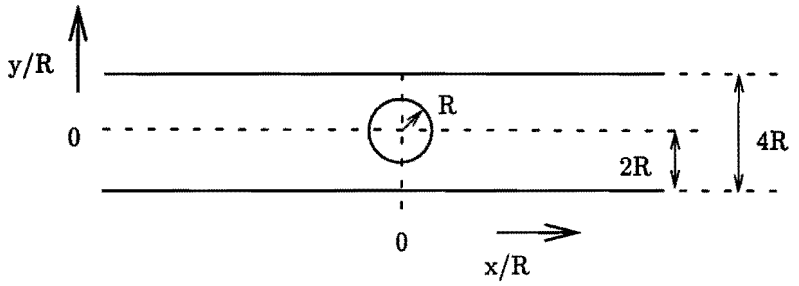

Figure 4.2: *Schematic cross sectional view of geometry with symmetrically confined cylinder. Radius R of the cylinder is 2 mm, height of the channel is $4R$, depth D (in the direction perpendicular to the plane of drawing) is $32R$ and total length in x direction is $200R$. Center of cylinder is at $x = 0, y = 0$. Mean flow is in positive x direction.*

4.3.2 Numerical method

The flow field has been computed with finite element methods (FEM) that are implemented in the package SEPRAN [101]. The definition of the mathematical problem to be solved (equations for conservation of mass and of momentum and the constitutive equations for the stress tensor) are described in Section 1.2. The full equation of conservation of momentum was used, since the Reynolds number ranged between 0.029 and 0.174, and test runs had shown that neglecting the convective term (Stokes flow approximation) influenced the solution of the velocity field up to approximately 5%.

Both the Carreau-Yasuda model and the PTT-B constitutive equation (definitions and parameter values as in Section 3.4) have been used at all flow rates in Table 4.2.

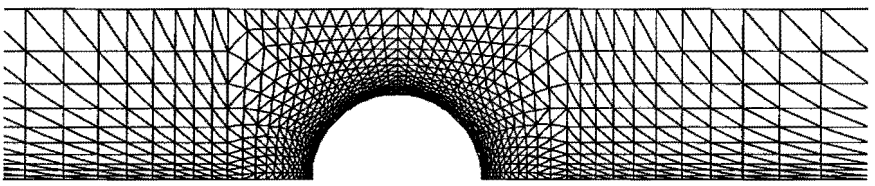

Figure 4.3: *Part of FEM mesh in case of geometry with symmetrically confined cylinder.*

Method for generalized Newtonian models Computations with the (generalized Newtonian) Carreau-Yasuda model are made with the Galerkin method (with a Picard linearization of the non-linear viscosity term), see Cuvelier et al. [20]. The velocity and pressure were discretized using the Crouzeix-Raviart $P_2{}^+ - P_1$ triangular element with extended quadratic basis functions for the velocity and a piecewise discontinuous linear basisfunction for the pressure. The pressure is eliminated with the penalty function method. Convergence of the iterative procedure was checked with

$$\frac{|u_k - u_{k-1}|_{max}}{|u_k|_{max}} < \epsilon_c \tag{4.1}$$

$$\hat{R}_k < \epsilon_c \tag{4.2}$$

$$\tag{4.3}$$

with u_k the velocity after the kth iteration, $\hat{R}_k = \frac{|Au_{k-1}|_{max}}{|u_{k-1}|_{max}}$ the relative residual of the discretized system after iteration $(k-1)$ and $\epsilon_c = 1 \cdot 10^{-4}$.

Method for viscoelastic models The viscoelastic computations have been performed with the method for stationary two dimensional flow of Hulsen and van der Zanden ([55], [56], [57]). It is an iterative, decoupled method. The balance equations of mass and momentum are discretized with the standard Galerkin method (with the same element as in case of the generalized Newtonian method). The extra-stress tensor is computed from the last computed velocity field by integration of the viscoelastic constitutive equation along the streamlines (that are computed from the velocity field via the streamfunction) with a fourth order Runge Kutta scheme. A Picard iteration scheme is used to solve the resulting set of non-linear equations. For details about the construction of the streamlines and the iterative procedure the reader is referred to Hulsen [55] and Hulsen and van der Zanden [57].

Convergence is tested after each iteration with

$$\frac{|u_{k+1} - u_k|_{max}}{|u_{k+1}|_{max}} < \epsilon_u \tag{4.4}$$

$$(\frac{R^T R}{\hat{R}^T \hat{R}})^{\frac{1}{2}} < \epsilon_r \tag{4.5}$$

$$\tag{4.6}$$

where u_k is the velocity after the k iteration, and R is the residual value of system of equations for the 'free' degrees of freedom (thus without the essential boundary conditions) for the discretized momentum equation and $\epsilon_u, \epsilon_r{}^2$ the convergence criteria (both usually $1 \cdot 10^{-3}$).

Part of the FEM mesh used in all computations is plotted in Figure 4.3, the complete mesh has 1900 elements and 3981 nodal points. The resulting problem has 7962 degrees of freedom (velocities only) in case of both the viscoelastic constitutive equation and the generalized Newtonian model. Mesh refinement in both x and y direction with a factor 1.5 did not influence the solution significantly.

Definition of boundary conditions Denote the velocity vector with $\vec{u}$, the outward normal on a boundary with $\vec{n}$, the tangential vector on the boundary with $\vec{t}$ and the Cauchy stress tensor with $\boldsymbol{\sigma}$. The boundary conditions are then defined by the symmetry condition

$$\vec{u} \cdot \vec{n} = 0 \tag{4.7}$$
$$\vec{t} \cdot (\boldsymbol{\sigma} \cdot \vec{n}) = 0 \tag{4.8}$$
$$\tag{4.9}$$

along the centerline at $y/R = 0$, and the no-slip condition

$$\vec{u} = \vec{0} \tag{4.10}$$

on the wall at $y/R = 2$ and on the cylinder wall. At the entrance and exit boundaries fully developed flow conditions were assumed in case of the viscoelastic computations, which were numerically calculated for the model used. In case of the generalized Newtonian model, for reasons of convenience a Newtonian velocity profile was assumed at entrance and exit boundaries. This may not be physically realistic, but sufficiently long entrance and exit lengths were used such that the discrepancy between these boundary conditions and the fully developed flow did not influence the solution in the flow region of interest (i.e. between $x/R = -5$ and $x/R = 15$).

$U\,[m/s]$	n_{iter} PTT-1	n_{iter} PTT-4
0.0424	29	13
0.0633	26	12
0.0700	22	6
0.0800	25	8
0.0868	22	6
0.1074	33	11
$\sum n_{iter}$	157	56

Table 4.1: *Mean velocity U and number of iterations n_{iter} for the computations with the 1 and 4 mode PTT equations, in case of the geometry with the symmetrically confined cylinder. The solution at each (except the lowest) flow rate was obtained by using the result of the previous (lower) flow rate.*

Model parameters Model parameters are used as fitted in Section 3.4 at a reference temperature of $25°C$. Because the experiments are performed at $T = 24 \pm 0.5°C$, it was checked that computations with parameters fitted at a reference temperature of $24°C$ showed no (significant) change compared to those for $25°C$.

The computations with the viscoelastic models were made by step-wise increasing the flow rate: first, at the lowest flow rate the solution was obtained with the iterative procedure and the result was used as the starting solution for the computation at a higher flow rate. The number of iterations for each flow rate is given in Table 4.1. Note that the use of the 4 mode model decreased the number of iterations.

4.3.3 Experimental aspects

Experimental set-up Figure 4.4 shows schematically the set-up used in the experiments with the position of the two measurement systems (for a detailed description of the equipment see Section 2.2.3). FIB and LDA measurements were performed simultaneously, but independently. Each system has its own computer controlled traverse: the LDA laser probe is mounted on a three axis traverse while the optical rail of the FIB system is connected to a two-axis traverse. To measure the centerline velocities near the cylinder, the LDA laser probe is positioned along the long side of the flow cell with the laser beams in the plane that is perpendicular to the axial (neutral) direction of the cylinder. This configuration also results in a fast data collection, since the light scattered in the whole solid-angle of the laser probe is useful for detection of Doppler bursts.

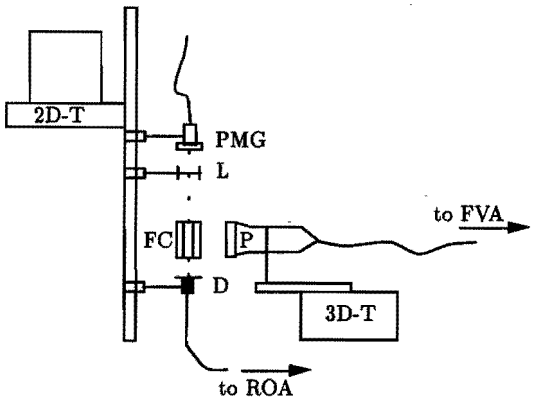

Figure 4.4: *Schematic drawing of the setup used during the experiments: the view is along the (vertical) mean flow direction through the flow cell (FC). The FIB rail (with PMG: polarization modulation generator (laser, polarizer, rotating halfwave plate), L: lens, D: detector with circular polarizer) is connected to a 2D-traverse (2D-T) and the LDA probe (P) to a 3D-traverse (3D-T). Both measurement systems, including the traverse tables, are controlled by a personal computer (FVA: hardware LDA system, ROA: hardware FIB system). Details of all equipment are given in Chapter 2.*

During the LDA experiments the velocity was averaged from 100 acquired samples that satisfied the strongest validation criterion ($+3\,dB$). Increasing the number of validated

samples did not change the average velocity. A seeding of small particles (Merck Iriodine 111, coated rutile crystals, density $\rho \approx 2.5 \cdot 10^3\, kg/m^3$, diameter particles $d_p \leq 15\, \mu m$) was added in a concentration of approximately $0.01\, g/l$ to increase the data rate. The effective data rate (= number of validated samples per unit of time) was between 50 and $400\, Hz$. The seeding did not affect the birefringence measurements. The laser was operated at a power level of $70\, mW$, and the high voltage of the photomultiplier was between 1000 and $1096\, V$.
The laser beam of the birefringence measurements is collimated by a lens with focal length $400\, mm$, which gave a maximum beam radius of $0.35\, mm$ at the exit and entrance windows of the flow cell (see Section 4.6 and Appendix C). From the measured birefringence parameters χ and Δn, the stresses were found using the stress optical rule (Section 2.3.2). The stress optical coefficient as determined by Quinzani [93] in a Couette flow cell was used: $C = 1.87 \cdot 10^{-9}\, Pa^{-1}$. In a later experiment, we measured the stress optical coefficient ourselves in a Couette cell for simultaneous mechanical and optical (with ROA) measurements on the Rheometrics-RFS-II (Figure 4.6 and Appendix D): $C = 1.86 \cdot 10^{-9}\, Pa^{-1}$.

Demonstration of the measurement accuracy of the LDA and FIB systems
Figures 4.5 and 4.9 show that at $x/R = -5.0$ the flow is fully developed. The agreement between calculated velocities (with the Carreau-Yasuda equation) and the measured velocities at this position is good. It also shows the accuracy of the LDA experiments at all flow rates. The measured velocities have a maximum error bound of approximately 3% of the mean value, but at most positions it is approximately 1%. In case of the lowest Deborah number these values are a factor two larger.

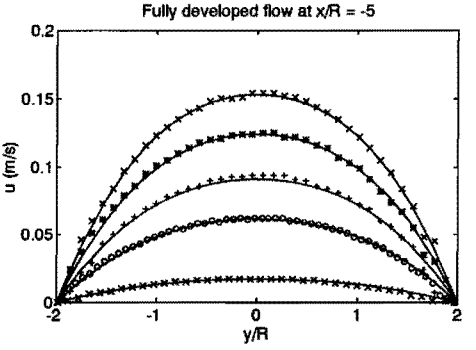

Figure 4.5: *Velocities in the fully developed flow region: measured and computed values (Carreau-Yasuda model (solid line)) at several De_1 numbers, $De_1 = 0.25, 0.93, 1.36, 1.87, 2.31$.*

Though Mackay and Boger [75] warned that a deviation of 15 to 20% in the value for the stress optical coefficient is possible between different batches of any polymeric fluid, the

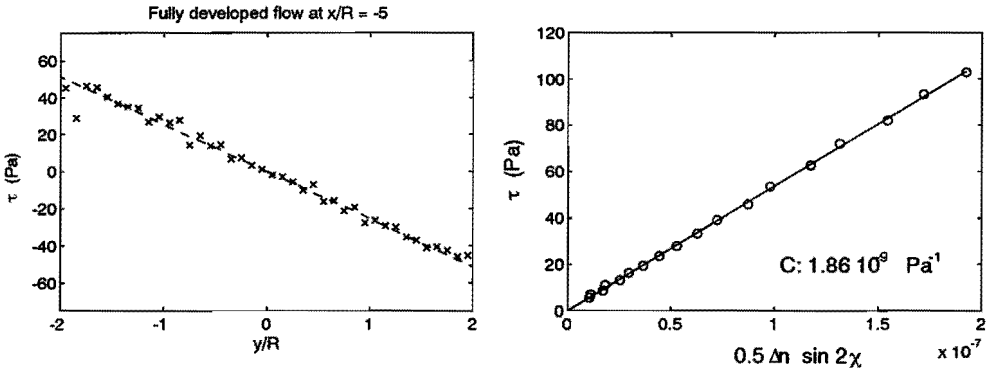

Figure 4.6: *Left: shear stress along a cross sectional line in the fully developed flow region: (x) measured using literature value* $C = 1.87 \cdot 10^{-9} Pa^{-1}$*, and (– –) computed with Carreau-Yasuda model at* $De_1 = 2.31$*. Right: validation of linearity of stress optical rule in a Couette cell with simultaneous mechanical and optical measurements (see Appendix D). The mechanical stress* τ *is plotted as function of the simultaneously measured optical signal* $\frac{\Delta n}{2} \sin 2\chi$*:* $C = 1.86 \cdot 10^{-9} Pa^{-1}$*.*

literature value used here proved to be accurate. This is shown at the highest flow rate in Figure 4.6, where the measured shear stress, along the cross sectional line at $x/R = -5.0$ in the region with developed flow, is plotted together with the result for the FEM computations with the generalized Carreau-Yasuda equation. The agreement is excellent.
To demonstrate further the accuracy of the optical stress measurements, the stresses measured in simple shear with the Rheometrics-RFS-2 (cone and plate geometry) in Chapter 3 are plotted together with the stresses as measured in the fully developed flow, which is also a simple shear flow. Figure 4.7 shows N_1 as function of τ. The measured curve of $N_1(\tau)$ on the RFS-2 has been fitted with the relation $N_1 = a\tau^b$ with $a = 0.13\, Pa^{(1-b)}$ and $b = 1.66$. A good agreement is found, and the scatter in the optically measured data is of the same magnitude as in the mechanically measured data.

Section 4.6 discusses in more detail the accuracy of the measurements.

4.3.4 Comparison of computations with experiments

Experimental conditions and dimensionless parameters Experiments were carried out at ambient temperature of $24 \pm 0.5\,°C$. Stresses and velocities were measured along five cross sectional lines (center of the cylinder at $(x = 0, y = 0)$, negative x-coordinates are upstream of this center): $x/R = -5, -2.0, -1.5, 1.5$ and 2.0, and along the centerline: $y/R = 0$ (see Figure 4.2).

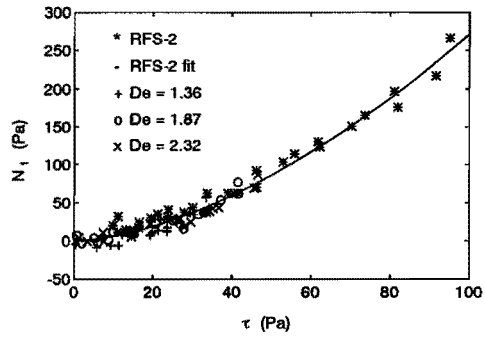

Figure 4.7: *Normal stress as function of shear stress for 5% PIB/C14. Data of measurements in simple shear ('RFS-2') and their fit ('RFS-2 fit', with $N_1 = a\tau^b$ see text) together with stresses measured with FIB along a cross section in the fully developed flow region in the planar flow cell at three De numbers.*

$U\,[m/s]$	$U/R\,[s^{-1}]$	$\tau_0\,[Pa]$	De_1	De_2	Re_1	Re_2
0.0115	5.750	16.865	0.248	0.268	0.019	0.019
0.0424	21.200	62.179	0.931	0.667	0.069	0.082
0.0633	31.650	92.828	1.364	0.699	0.102	0.133
0.0868	43.400	127.291	1.871	0.737	0.140	0.195
0.1074	53.700	157.500	2.315	0.769	0.174	0.256

Table 4.2: *Mean velocity U, typical shear rate U/R, scaling stress τ_0, and dimensionless numbers De_1, De_2, Re_1, and Re_2 for the cases studied in the geometry with the symmetrically confined cylinder (definition of τ_0 see text, definitions of De_1, De_2, Re_1 and Re_2 in Chapter 1).*

Velocities are non-dimensionalized with the mean velocity U, and stresses with

$$\tau_0 = 3\eta_0 U/R, \tag{4.11}$$

where η_0 is the zero shear viscosity. The factor 3 in this definition of τ_0 is arbitrary and is added only to obtain a scaling that fitted nicely in the plots of Figures 4.10 to 4.14. Table 4.2 shows the values for the non-dimensionalizing parameters U and τ_0, together with the dimensionless numbers De_1, De_2, Re_1 and Re_2 as defined in Section 1.2. The De_2 numbers are calculated from fits of $N_1(\dot{\gamma})$ and $\eta(\dot{\gamma})$ measured in steady shear. The lowest flow rate in Table 4.2 is also the lowest flow rate that can be used in the system.

Two dimensionality of the flow LDA measurements along the third, 'neutral' direction at two positions (at $x/R = -5$ and $x/R = 1.5$) show the assumption of a nominally

two-dimensional flow field is good, see Figure 4.8.

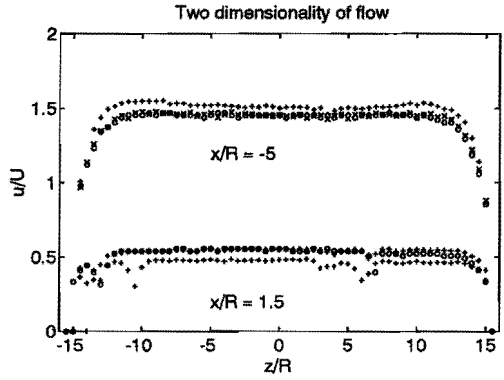

Figure 4.8: *Measurement of the axial velocity along the neutral (z-)direction at two positions ($x/R = -5.0, 1.5$) and three flow rates ('+': $U = 0.0118\,[m/s]$, 'x': $U = 0.0424\,[m/s]$ and 'o': $U = 0.0633\,[m/s]$), showing that the flow is nominally two-dimensional.*

Axial velocity field

Centerline elongation rate The measured velocities along the center line have been fitted with polynomials to calculate the elongational velocity gradient (elongation rate) along this line. The results are plotted in Figure 4.9. It appears that the elongation rate is minimal $\approx -65\,s^{-1}$ upstream of the cylinder, and maximal $\approx 70 s^{-1}$ downstream of the cylinder at the highest flow rate. This magnitude is an order higher than in the study of Armstrong et al. [4], where the maximum elongation rate was $\approx 10 s^{-1}$.

Axial velocities along cross sections At all Deborah numbers excellent pointwise agreement is found between the measured axial velocities and those computed with the Carreau-Yasuda model (Figures 4.10 - 4.14).

The results for the single and four mode PTT model agree excellently with measured data at the two lowest Deborah numbers ($De_1 = 0.25, 0.93$). The good agreement between computed and measured axial velocities at $De_1 = 0.25$ for all models (Figure 4.10) was expected, since the flow at this low Deborah number approximates Newtonian flow, thus the velocities of both the Carreau-Yasuda model and the PTT models should coincide.

At the higher Deborah numbers the agreement is well for the four mode model and fairly well for the single mode model. Largest differences between measured and computed data are found downstream near the center line. In case of the single mode model the differences are quantitatively and qualitatively most pronounced (this is most evident in the plots along the center line, see below).

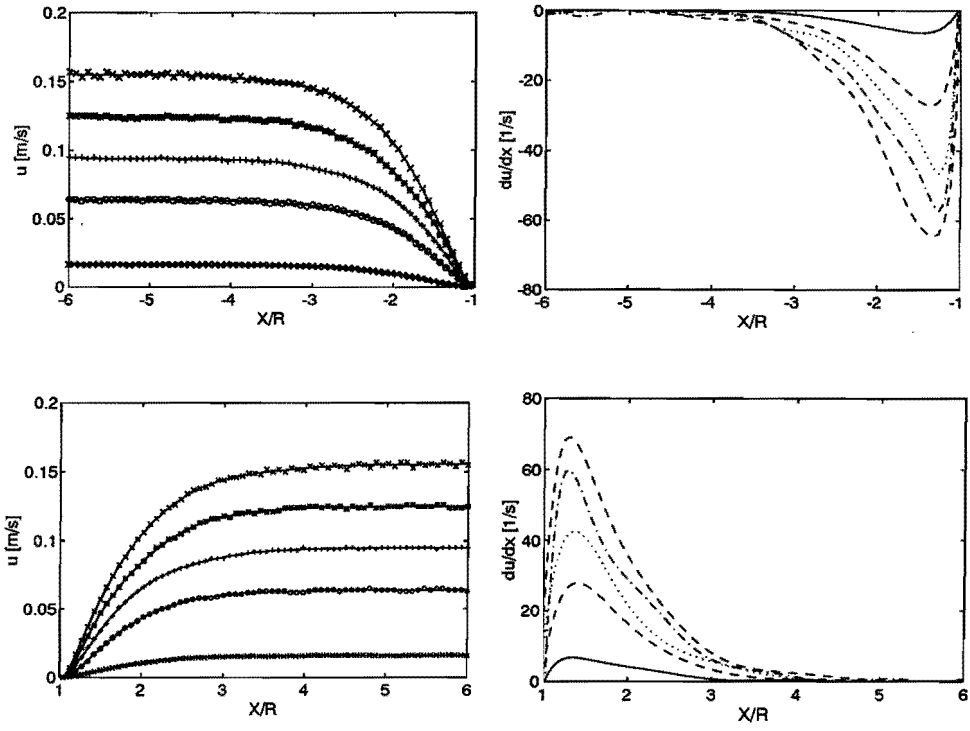

Figure 4.9: *Polynomial fit of measured velocities along centerline past the symmetrically confined cylinder (left) and the derivative of fitted polynom (right) at the five Deborah numbers investigated (see Table 4.2). Top row: upstream of cylinder, bottom row: downstream of cylinder.* $De_1 = 0.25, 0.93, 1.36, 1.87, 2.31$.

Axial velocities along centerline Along the center line upstream of the cylinder, the computed axial velocities agree excellently with measured data for both PTT models at all Deborah numbers.

At Deborah numbers larger than 1, most pronounced differences exist in the wake of the cylinder at the centerline between the computed results for both PTT models and the measured velocities. Just downstream of the cylinder, the calculated axial velocities rise more steeply for the PTT models. The effect is strongest for the single mode PTT model. For this model, at De_1 equal to 1.87 and 2.31, an overshoot in the velocity profile is observed, which is (almost) not present in case of the four mode PTT model. The overshoot is completely absent in the measured velocities and in the results for the Carreau-Yasuda model. This difference between computed and measured velocities indicates a model error of the PTT model, which is most severe in case of the single mode model. The results for

the four mode model show a remarkable improvement, but a difference with the measured velocities remains.

Stress field

Good agreement is found between computed and measured stresses at all flow rates with both PTT models, and sometimes the agreement is excellent (Figures 4.10 - 4.12 and 4.15 - 4.16). The comparison is discussed in detail below. In the plots along cross lines, the profiles of N_1 at $x/R = 2.0, -2.0$ are left out to improve the lay-out of the plots.

Computed values of the stress field are only presented for the viscoelastic constitutive equation (PTT model), since the measured stresses were determined using the stress optical rule which is only supported by theory for (visco-)elastic materials (see Section 2.3.2). Moreover, such model can not describe normal stresses in shear flow, which gives non-realistic predictions. A comparison with data for the Carreau-Yasuda equation is nevertheless made in Section 4.6.

Stresses along cross sections The stress measurement at the lowest Deborah number (0.25) were not accurate, since the birefringence of the fluid was of the same magnitude as the (small) spatial variation in the background signal (see Section 4.6.2). However, fairly well agreement is still observed (Figure 4.10).

At $De_1 = 0.93$ and 1.36 excellent agreement is found between computed and measured stresses along all cross sections in Figures 4.11 and 4.12. Differences between the two PTT models are negligible at these two Deborah numbers, except for the maximum value of N_1 at $x/R = 1.5$. At that position the single mode PTT model has a higher maximum than the four mode model.

At $De_1 = 1.87$ and 2.31 more differences are found. As will also be shown below for the center line stresses, the presence of the cylinder is manifest further upstream of the cylinder than in the computations. The minimum normal stress difference at $x/R = -1.5$ is lower for the measured data than for both PTT models. The differences between the two models are largest in the extrema of the profiles of the normal stress difference: upstream of the cylinder the four mode model is closer to the measured data, while downstream the agreement is excellent in case of the single mode model and somewhat less for the four mode model. Both models predict the shear stress profiles well downstream of the cylinder, but upstream of the cylinder the agreement is only qualitative.

Stresses along center line Figures 4.15 - 4.16 show along the centerline for $De_1 = 0.93$ and 1.36 good pointwise agreement between measured and computed stresses with both models. Small differences can be seen between the single and the four mode PTT model: the maximum value of the downstream stress profile is somewhat larger for the single mode model. Note the excellent agreement for the measured and computed normal stress differences upstream of the cylinder.

At the two highest Deborah numbers ($De_1 = 1.87$, and 2.31) pronounced differences are observed between measured and computed normal stress differences. Also, the two model

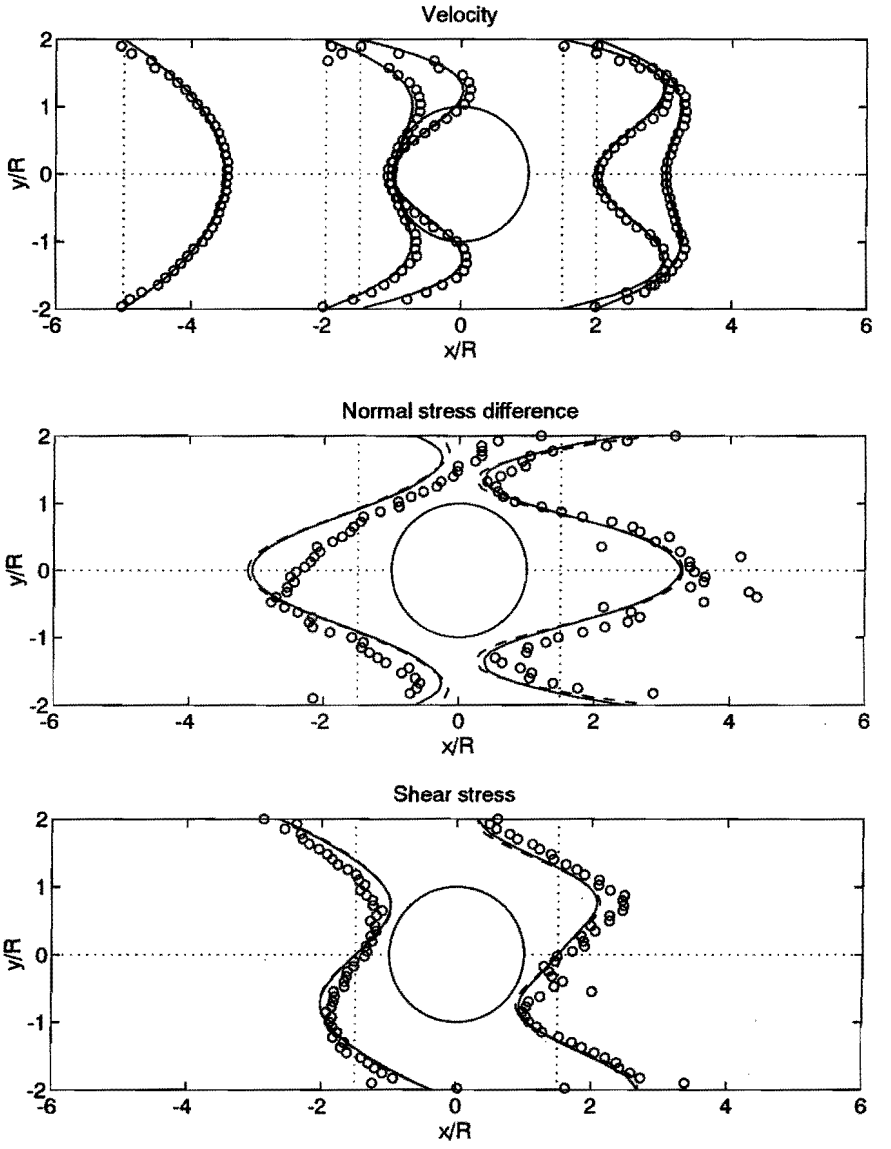

Figure 4.10: *Measured (o) and computed (—: 4−mode PTT model, − −: 1− mode PTT model, − · −: Carreau Yasuda model (velocities only)) results for the planar flow of the 5% PIB/C14 solution at* $De_1 = 0.25$ *past a cylinder confined symmetrically between two parallel plates: velocity (top), first normal stress difference (middle) , shear stress (bottom). Velocities are non-dimensionalized with the mean velocity* U*, and the stresses with* τ_0 *(see text).*

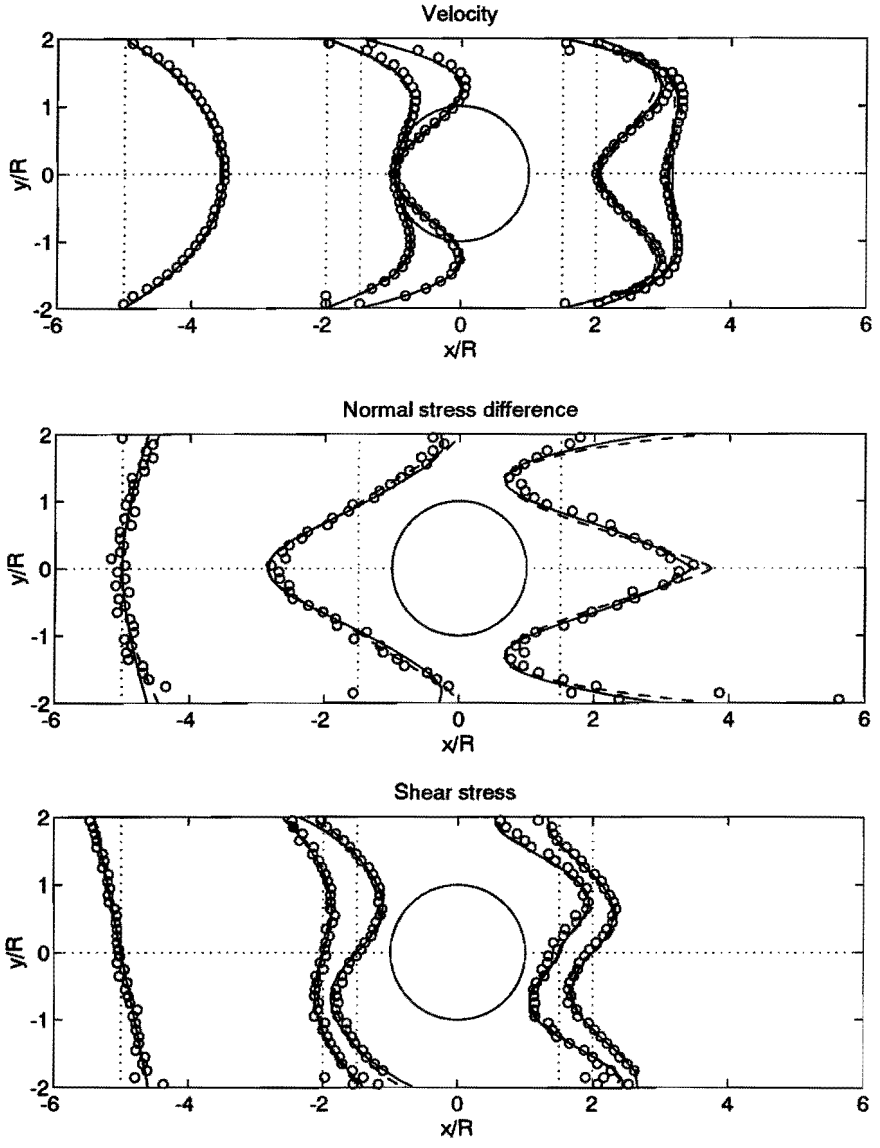

Figure 4.11: *As in Figure 4.10, now with* $De_1 = 0.93$.

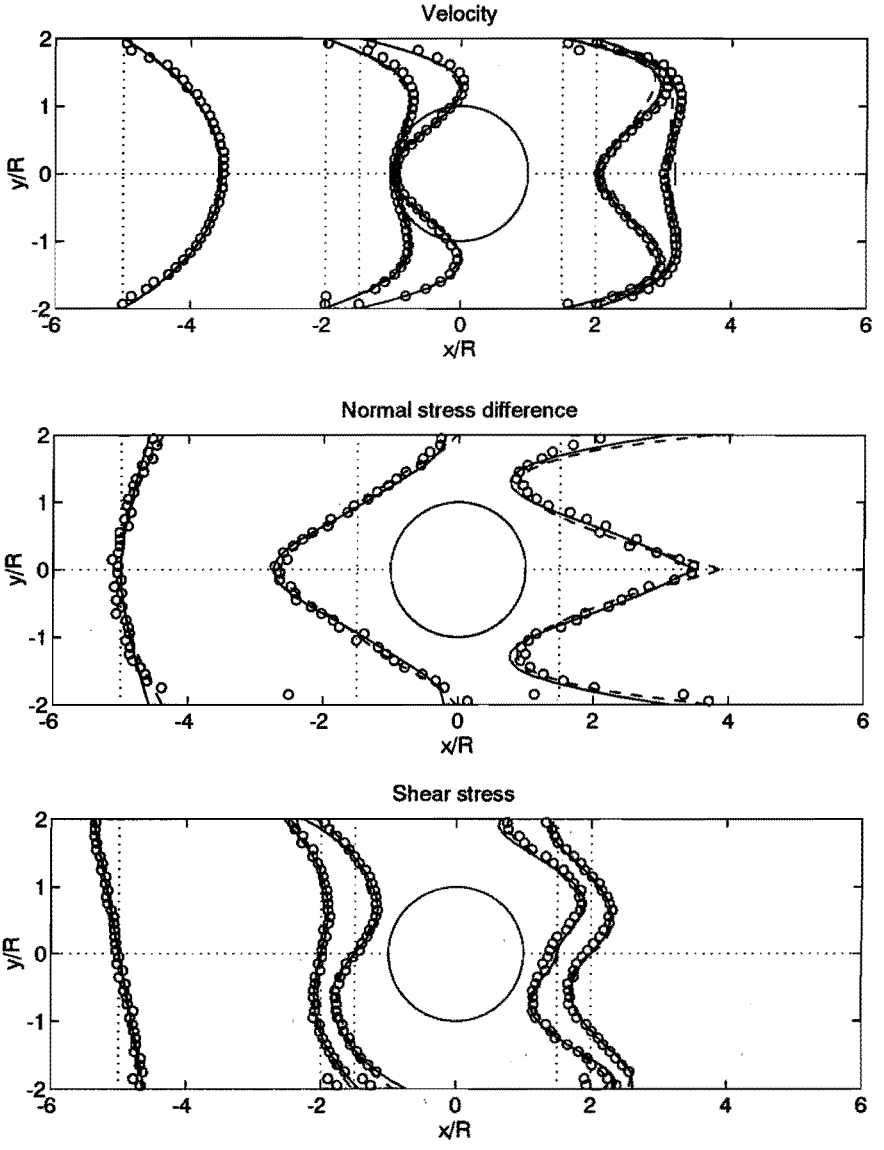

Figure 4.12: *As in Figure 4.10, now with* $De_1 = 1.36$.

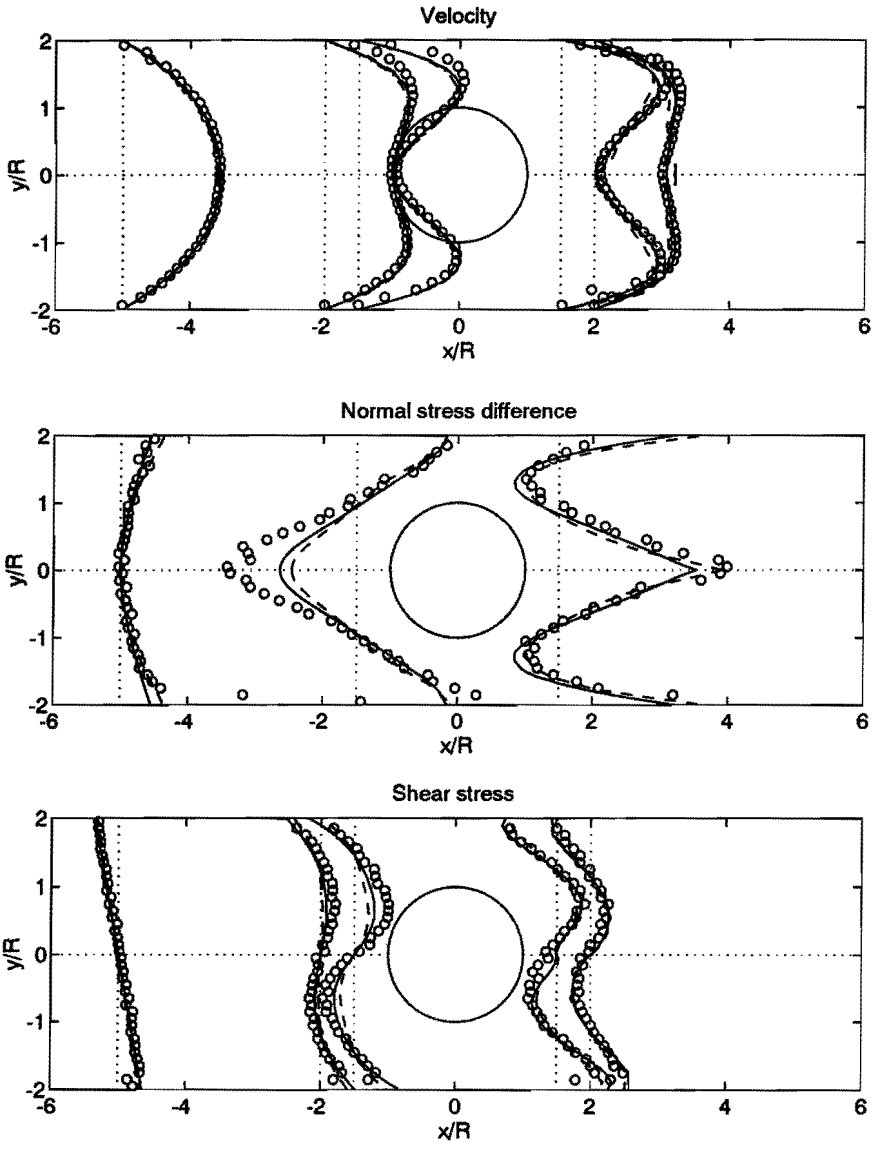

Figure 4.13: *As in Figure 4.10, now with* $De_1 = 1.87$.

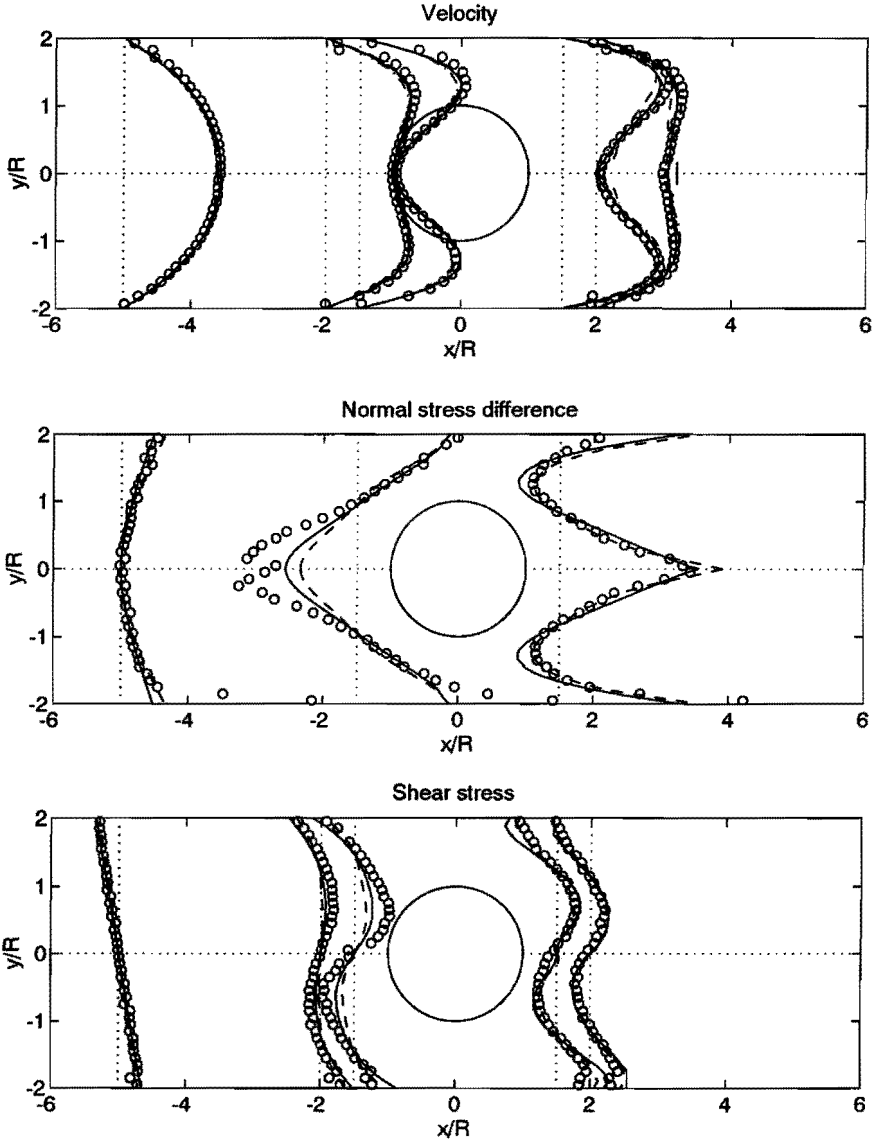

Figure 4.14: *As in Figure 4.10, now with* $De_1 = 2.31$.

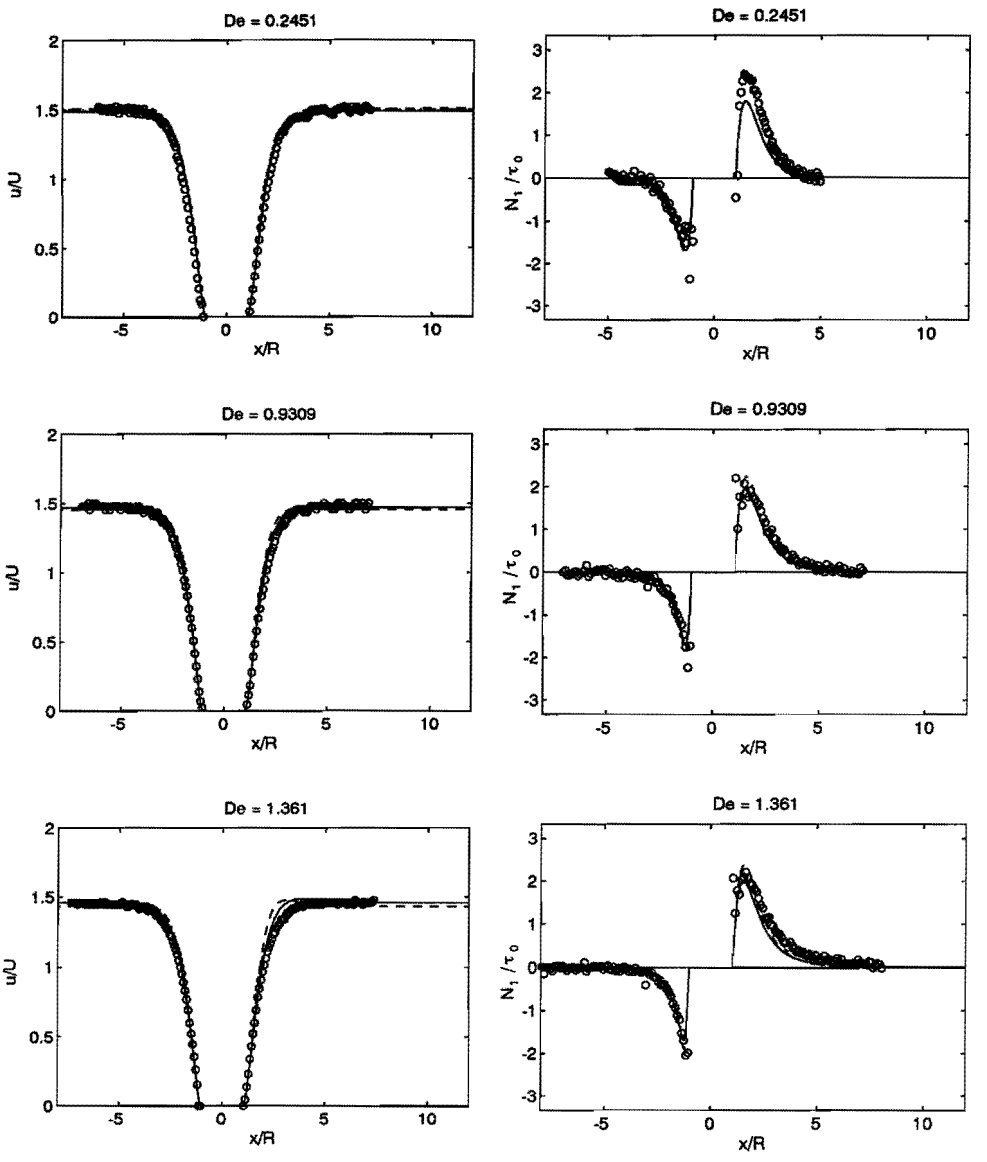

Figure 4.15: *Measured (o) and computed (—: 4-mode PTT model, – –: 1-mode PTT , – · –: Carreau-Yasuda (velocity only)) velocity (left) and first normal stress difference (non-dimensionalized with stress τ_0 (see text)) (right) along the centerline for the flow of the 5% PIB/C14 solution past a symmetrically confined cylinder, for $De_1 = 0.25, 0.93, 1.36$.*

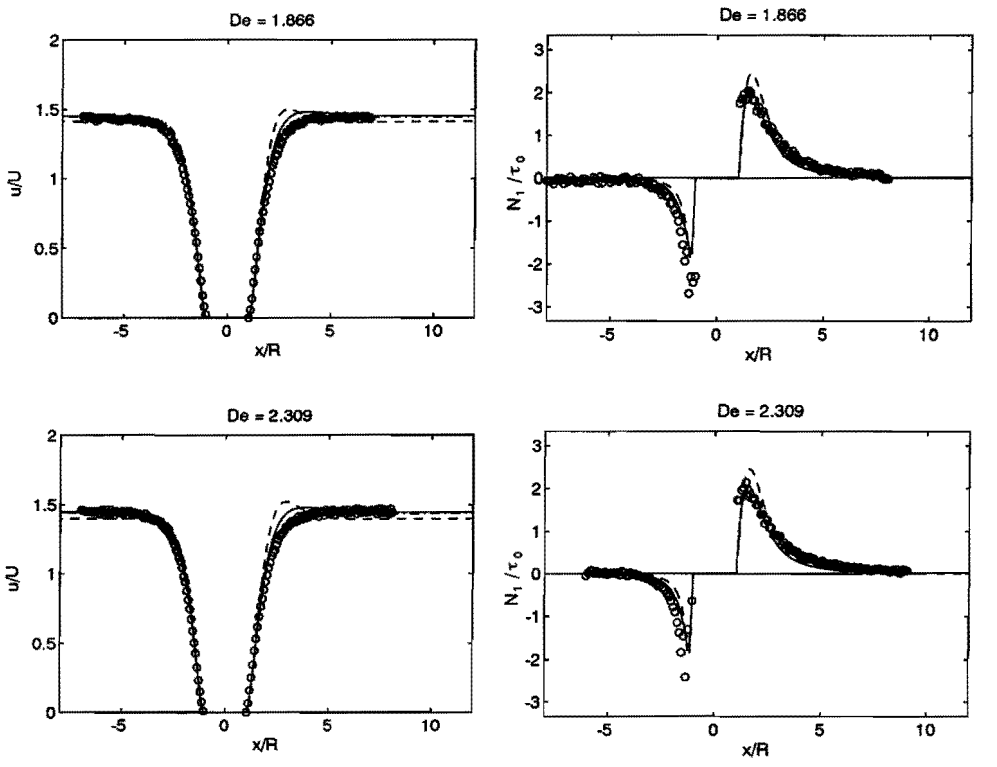

Figure 4.16: *As in Figure 4.15, now with* $De_1 = 1.87, 2.31$.

predictions are quantitatively different. Upstream of the cylinder, the measured profile of the normal stress difference is shifted upstream compared with the computations, and the four mode model is closer to the measured data than the single mode model. Downstream of the cylinder, the agreement with measurements is for the four mode PTT model excellent. Fairly well agreement is found for the single mode model, it has however a maximum that is too high compared with measured data.

Comparison with results of Baaijens et al. [9] The above results for the stresses are not in accordance with those presented in our earlier study Baaijens et al. [9] (see also *Note added in proof* in [9]). In that paper, we presented for the same fluid in the same geometry normal stress measurements at $De = 0.22$, that were much higher (a factor 2 for the maximum value along the centerline) and, more important, relaxed much slower: after 7 cylinder radii, the stresses on the center line downstream of the cylinder were still about 50% of their maximum value (that was located at about 3 radii past the cylinder). We

now argue that the discrepancy between the results in [9] and those in this thesis can only be explained by a change in the rheological behavior during the older experiments.
In [9], we have discussed all possible systematic errors (influence of the subtraction procedure to account for the parasitic birefringence in the glass windows, failure of stress optical rule) that might have affected the stress measurements. All these effects were expected to be of minor relevance. However, we felt uncomfortable with the procedure we had to use to eliminate the influence of the parasitic stresses in the flow cell windows. Therefore, the SF-57 glass has been used in the present study.
Other changes were made as well in the experimental setup used in this thesis: a flow cell with smaller dimensions (factor 2), other tubing and a different type of pump. Also, the stress measurements have been performed with our own, new ROA system.
After replacing in the present experimental setup the new flow cell with the older one (used in [9]), we measured along the centerline (using the measurement procedure as in [9]) essentially the same stress distribution at $De \approx 0.22$ as shown above in this section at $De = 0.25$ (Figure 4.15). This proves, that there was no influence of the flow cell or measurement procedure in the older experiments. Only a change of the rheological properties can have caused the observed effects. The question how this has occurred is under investigation.

4.4 Flow of 5 % PIB/C14 past an asymmetrically confined cylinder

4.4.1 Introduction

Next, the influence of viscoelasticity on the flow in a channel with an asymmetrically confined cylinder has been investigated, since it was expected that this asymmetrical flow would be more sensitive for viscoelastic effects such that the velocities upstream of the cylinder are changed (see also Section 1.4). Since in the previous section the four mode PTT model was found to be superior to the one mode fit, here only the four mode fit will be used in the viscoelastic computations.

In the experiments the cylinder has been moved $1\,mm$ towards one of the walls, which resulted in a narrower gap between the wall and the cylinder of $1\,mm$ at that side of the cylinder and a wider gap of $3\,mm$ on the other side (see Figure 4.17).

4.4.2 Experimental and numerical aspects

Keeping $x/R = y/R = 0$ in the center of the cylinder, the wall that is closest to the cylinder is at $y/R = 1.5$, and the other wall at $y/R = -2.5$. Measurements of the axial velocities and the stresses have been performed along cross sectional lines at $x/R = -5.0, \pm 2.5, \pm 2.0, \pm 1.5, 0.0$ and along axial lines at $y/R = 0, -1.5$. The flow rate was set such that the mean velocity was $0.0868\,m/s$, and thus $De_1 = 1.87$. The stress measurements were performed with a lens with a focal length $f = 200\,mm$, which resulted in

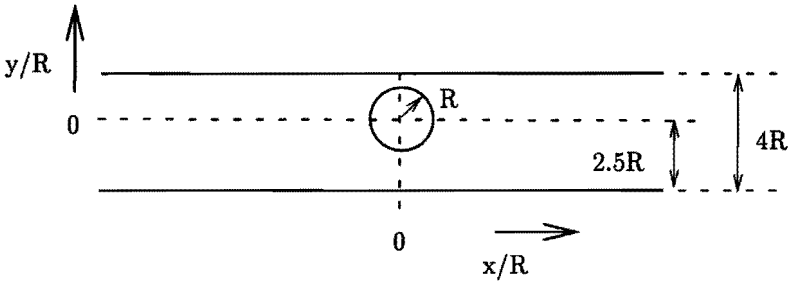

Figure 4.17: *Geometry with asymmetrically confined cylinder. Radius R of the cylinder is $2\,mm$, height of the channel is $4R$, depth D (in the direction perpendicular to the plane of drawing) is $32R$ and total length in x direction is $200R$. Center of cylinder is at $x = 0, y = 0$. Mean flow is in positive x direction.*

a maximum beam radius at the exit and entrance planes of the flow cell of $\approx 0.25\,mm$ (Section 4.6.2).

The same numerical method was used as in the previous Section. Part of the mesh is shown in Figure 4.18: it has 5364 elements and 11014 nodal points and 22028 degrees of freedom (velocities only).

Both the generalized Newtonian Carreau-Yasuda model and the four-mode PTT equation were used, with parameter values as in Subsection 4.3.2. Convergence was obtained with the convergence criteria as in Section 4.3. In case of the PTT equation, computations were performed by increasing the flow rate stepwise using each result as a starting value for the new computation (Table 4.3).

$U\,[m/s]$	n_{iter}
0.0212	13
0.0415	15
0.0562	12
0.0868	21
Σn_{iter}	61

Table 4.3: *Mean velocity U and number of iterations n_{iter} for the computations with the 4 mode PTT equation, in case of the geometry with the asymmetrically confined cylinder. The solution with $U = 0.0868\,m/s$ was obtained by increasing the flow rate stepwise, which resulted in total 61 iterations.*

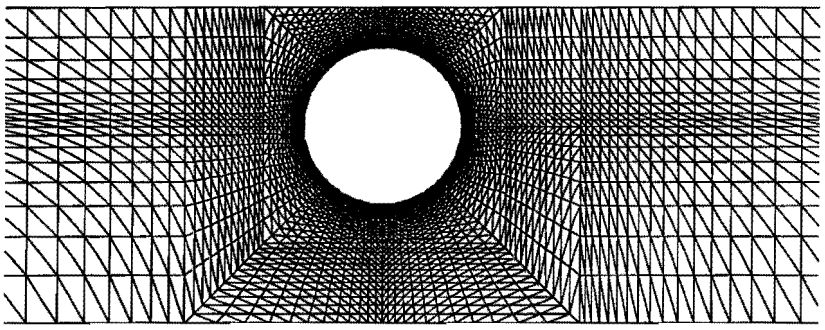

Figure 4.18: *Part of mesh used for the geometry with asymmetrically confined cylinder.*

4.4.3 Comparison of computations with experiments

Axial velocity field

Axial velocities along cross sectional lines Figures 4.19 shows the results for the asymmetrically confined cylinder geometry. For both constitutive equations, the computed velocity profiles upstream of the cylinder agree well with those that were measured. This is not in accordance with the expectations (as discussed in Section 1.4) that the elongation thickening of the viscoelastic material causes a significantly larger flow through the broader gap compared with inelastic fluids.
Comparison of the computed velocity profiles with the velocity measurements along line $x/R = 0$ in the broader gap shows that both models describe the measured velocity well (Figure 4.20). Near the top of the profile, the Carreau-Yasuda model is closer to the measured data than the PTT model, which predicts a higher maximum . This might be due to the too less shear thinning behavior of the PTT model for shear rates above $100s^{-1}$, since at this site high shear rates are present with a maximum value $\approx 250\,s^{-1}$ (compare Figure 3.3).

Axial velocities along axial lines The measured velocity profile along line $y/R = -1.5$ is closer described by the Carreau-Yasuda model than by the PTT model: the latter has a too high maximum (Figure 4.20). For both models, the rising and descending parts of the computed velocity profile agree well with the measured data.

Along line $y/R = 0$ (upstream and downstream of the cylinder), excellent agreement is observed between both computed and measured velocities. No overshoot of the velocity downstream of the cylinder exists here.

Downstream of the cylinder, the computed velocity profiles for the PTT model agree

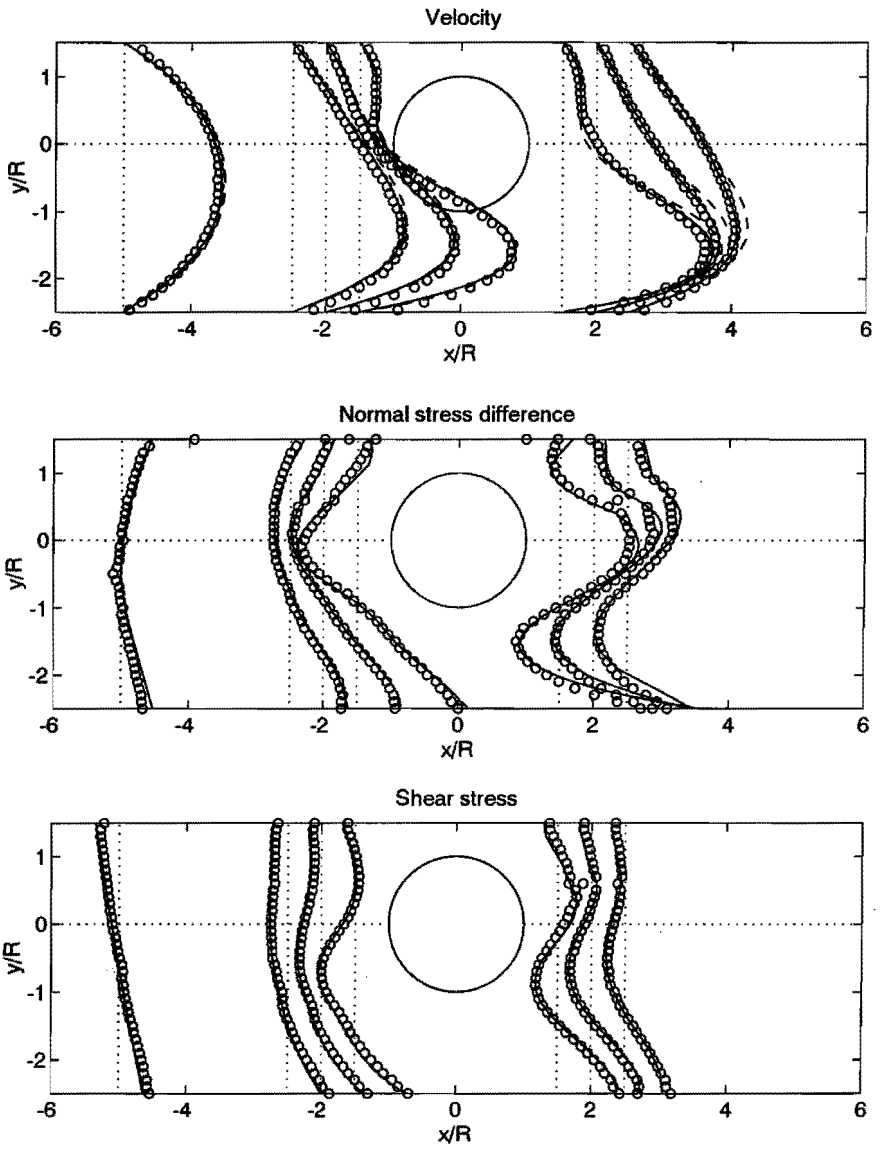

Figure 4.19: *Measured (o) and computed (— : 4-mode PTT, −−: Carreau-Yasuda (velocities only)) quantities for the planar flow of the 5% PIB/C14 solution at* $De_1 = 1.87$ *past an asymmetrically confined cylinder: velocity (top), first normal stress difference (middle), shear stress (bottom). Velocities are non-dimensionalized with the mean velocity* U*, and the stresses with* τ_0 *(see text).*

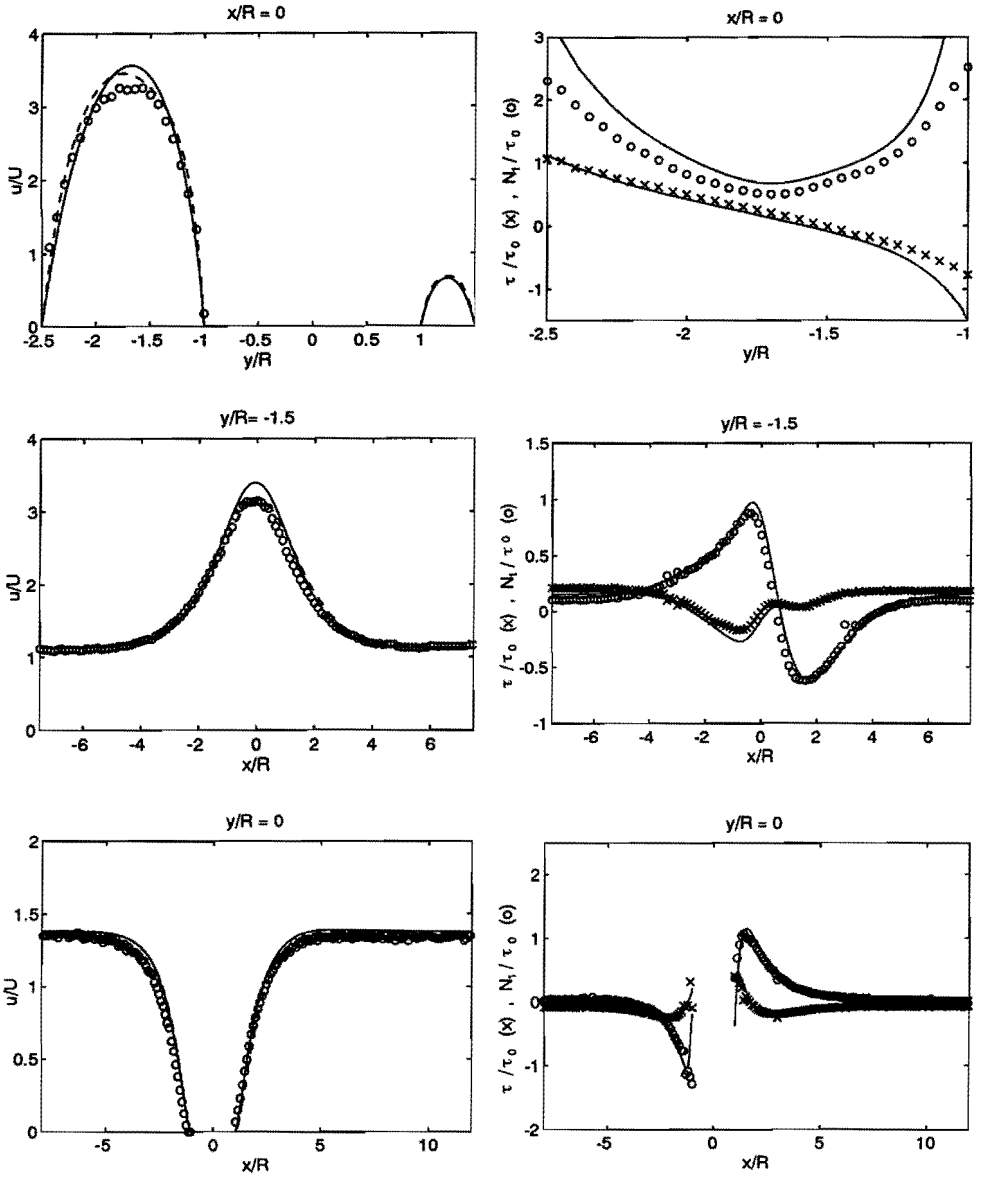

Figure 4.20: *Left column: measured (o) and computed velocities (—: 4-mode PTT, – –: Carreau-Yasuda) along several lines in the flow of the 5% PIB/C14 solution past an asymmetrically confined cylinder. Right column: measured (x: τ, o: N_1) and computed stresses (4 mode PTT only) along the same lines as the velocities in the left column. $De_1 = 1.87$.*

excellently with the measured velocities and better than those for the Carreau-Yasuda equation (Figure 4.19).

Stress field

As in the previous case, stresses are non-dimensionalized with $\tau_0 = 3\eta_0 U/R$ ($= 127.3\,Pa$ at the present flow rate).

Stresses along cross sectional lines The normal stress difference along cross sectional lines upstream of the cylinder that is computed with the PTT model agree excellently with measured data.

Downstream of the cylinder some small differences between computed and measured normal stress differences are found near the line $y/R = 0$, but the agreement is still impressive.

Excellent pointwise agreement is found between measured and computed shear stresses at all sites (Figure 4.19).

Stresses along axial lines Excellent agreement of computed and measured stresses exists along line $y/R = 0$.

4.5 Flow past a cylinder for a 9 % PIB/C14 solution

4.5.1 Introduction

In the process towards the investigation and characterization of the rheological behavior of polymer melts in complex flows, now a model fluid is used with a viscosity and elasticity closer to those of a polymer melt than the 5% PIB/C14 solution. The same PIB and tetradecane as in the previous section of this chapter are used, but now in a 9%(w/w) PIB/C14 solution. The rheology in simple shear flow has been described in Section 3.5. To account for changes in rheology during the experiments, the characterization of fluid, after being used in the experiments, is described below in Section 4.5.2. Only results are presented for the flow past a symmetrically confined cylinder, and show qualitatively similar flow phenomena as in case of the 5% PIB/C14 solution at the highest flow rate (Section 4.3).

4.5.2 Rheological parameters during the experiments

During the experiments with the 9% PIB/C14 solution changes in the rheology of the fluid occurred. After two days of experiments, for example the zero-shear viscosity was 0.75 times the value for fresh fluid. Most probably, these changes are caused by polymer degradation, which may be caused by high shear and elongation rates in the flow loop.

The present solution appears to be more sensitive for that than the 5% PIB/C14 solution used in the previous part of this chapter, where no changes were found.

The changes have been quantified by measuring the steady shear viscosity and the complex viscosity. Three samples were studied: the original (fresh) sample, a sample after one day of experiments, and a sample after two days of experiments. The results are shown in Figure 4.21. The effect was strongest during the first day of the experiments. Relatively little changes occurred during the second day (a change of approximately 5%), which justifies the use of the experimental data acquired on the second day. However, it is emphasized that such rheological changes are undesirable in the experiments. The question how to avoid this must be dealt with in future research.

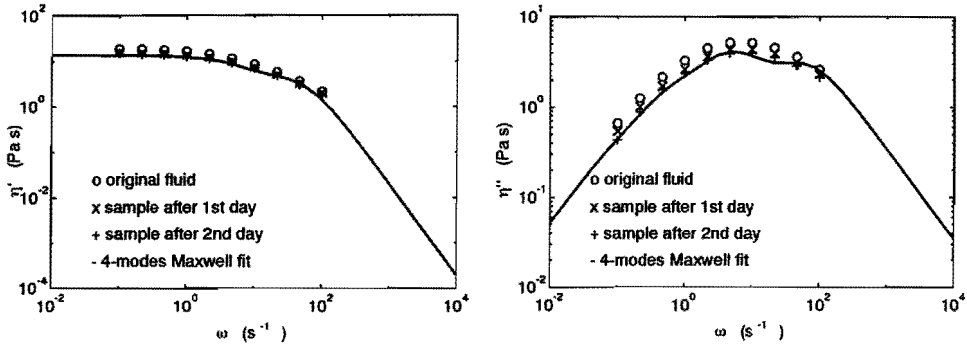

Figure 4.21: *Components of the complex viscosity measured at three moments in time during the experiments with the 9% PIB/C14 solution together with a four mode Maxwell fit on the data measured after the second day. Large changes are observed between data for a fresh sample and after the first day of the experiments. Only little differences exist between data of the sample taken after the first day of the experiments and the sample taken after the second day.*

The material functions in steady shear of the sample taken after the second day of the experiments have been used to fit the PTT and Giesekus models (following the procedure as described in Section 3.5.2). The results are plotted in Figure 4.22, and the fitted model parameters are listed in Table 4.4. The steady shear viscosity has been fitted with a Carreau-Yasuda equation with parameters $\{a, n, \lambda_{cy}, \eta_{cy}\} = \{1, 0.46, 0.18\,[s], 14.9\,[Pa\,s]\}$. The four mode models agree excellently with the data, for both the Giesekus and the PTT model, the Giesekus model being a little better. The one mode versions suffer of too large normal stresses combined with a too strong shear thinning.

4.5.3 Experimental and computational aspects

For details of the experimental set-up and measurement technique it is referred to Section 4.3.3. As already stated in Section 2.3.4, one change was made in the hardware of the FIB measurement system: the rotating halfwave plate was replaced by a quartz halfwave

	Maxwell parameters		PTT		Giesekus
n	$\eta_i\,[Pa\,s]$	$\lambda_i\,[s]$	ξ	ϵ	α
1	13.1	$1.06 \cdot 10^{-1}$	0.0	0.65	0.43
4	$4.91 \cdot 10^{0}$	$1.61 \cdot 10^{-2}$	0.0	0.75	0.50
	$7.10 \cdot 10^{0}$	$2.01 \cdot 10^{-1}$			
	$1.60 \cdot 10^{0}$	$1.41 \cdot 10^{0}$			
	$1.43 \cdot 10^{0}$	$9.90 \cdot 10^{0}$			

Table 4.4: *Model parameters of the non-linear viscoelastic constitutive equations for the 9% PIB/C14 solution during the experiments (n: number of modes).*

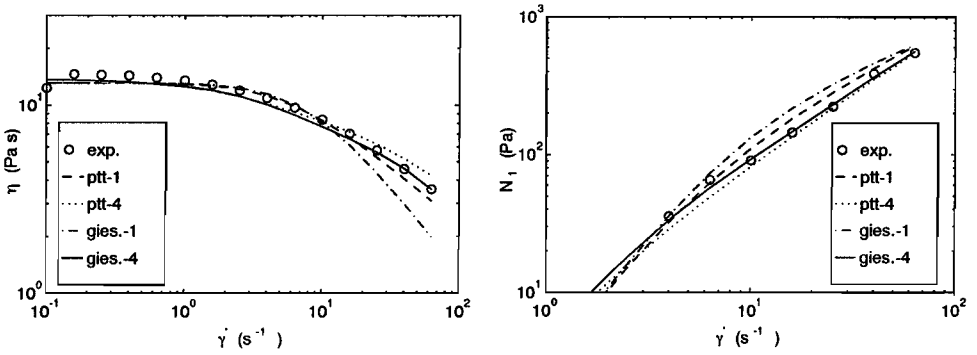

Figure 4.22: *Fits of the steady shear viscosity (left) and first normal stress difference (right) for the degraded 9% PIB/C14 solution. The number n is the number of modes.*

plate with a beam deviation less than $1 arc s$. This increased the spatial resolution: the beam radius at the entrance and exit planes of the flow cell was now $0.15\,mm$ with a lens with focal length $800\,mm$, which is in good agreement with the theoretically expected value ($0.12\,mm$, Appendix C).

Flow conditions The steady flow conditions during the measurements are characterized by the Deborah number De_1 and Reynolds number Re_1 listed in Table 4.5. Temperature was $26 \pm 0.5°C$.

Demonstration of the FIB measurements Figure 4.23 shows the accuracy of the FIB measurements with the current measurement system and model fluid. Stresses measured in simple shear (on the Rheometrics-RFS-2) and the fit with $N_1 = a\tau^b, a = 0.19([Pa^{1-1.46}]), b = 1.46[-]$) are compared with stresses measured with FIB in the fully developed flow region in the planar flow cell. The scatter in the optically measured data is now smaller than

$U\,[m/s]$	$U/R\,[s^{-1}]$	$\tau_0\,[Pa]$	De_1	Re_1
$3.15 \cdot 10^{-2}$	$1.58 \cdot 10^{1}$	$2.36 \cdot 10^{2}$	$5.61 \cdot 10^{0}$	$3.36 \cdot 10^{-3}$

Table 4.5: *Mean velocity U, typical shear rate U/R, scaling stress τ_0, and dimensionless numbers De_1 and Re_1 for the cases studied in the geometry with the symmetrically confined cylinder (definition of $\tau_0 = 3\eta_0 U/R$ (see Section 4.3.4), definitions of De_1 and Re_1: see Section 1.2).*

the scatter in the mechanically measured data. The accuracy of the stresses measured with FIB are increased compared with the data in Figure 4.7. This is probably due to the increased spatial resolution of the FIB laser beam using the new halfwave plate combined with the higher birefringence level in the 9% PIB/C14 solution.

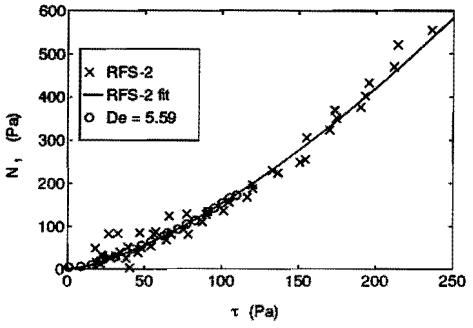

Figure 4.23: *Normal stress as function of shear stress for 9% PIB/C14. Data of measurements in simple shear ('RFS-2') and their fit ('RFS fit', $N_1 = a\tau^b$, see text) together with stresses measured with FIB along a cross section in the fully developed flow region in the planar flow cell.*

Computational method The same computational method (including boundary conditions and mesh) has been used as in case of the 5% PIB/C14 solution (Section 4.3), together with a four mode PTT equation, a four mode Giesekus equation, and a Carreau-Yasuda (CY) equation. Single mode models were not used, since the fits of the rheological data in steady simple shear of the four mode models were much better, as illustrated in Figure 4.22.

4.5.4 Comparison of computations with experiments

Fully developed flow The measured and computed velocity profiles and stress profiles along a cross section in the fully developed flow region agree excellently (Figure 4.24).

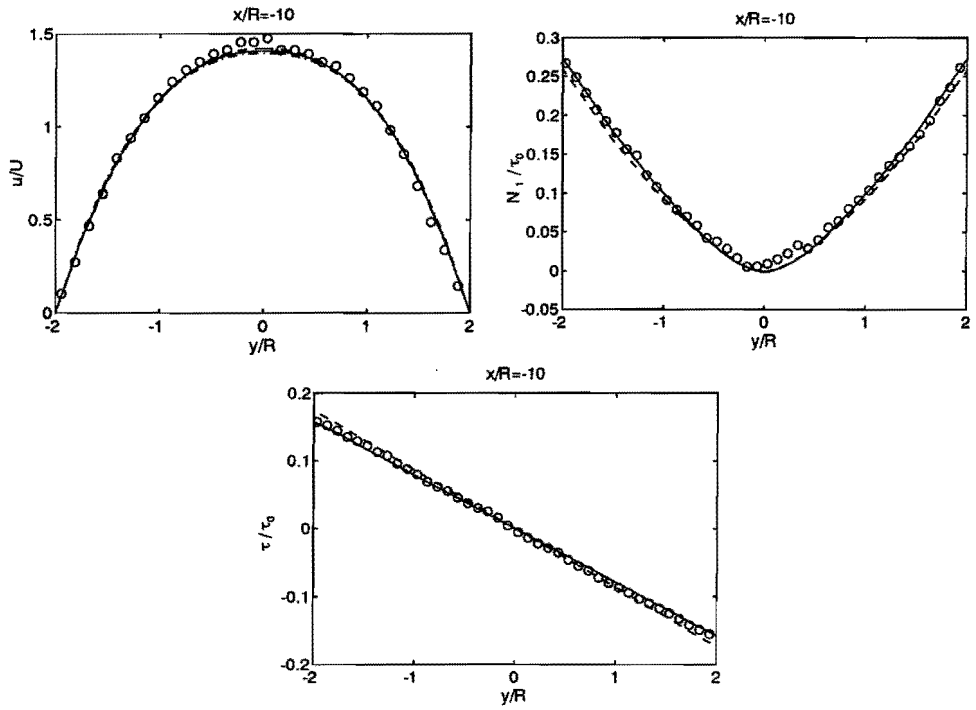

Figure 4.24: *Velocities (left) and stresses (right) along cross section $x/R = -10$ in the fully developed flow region for the 9% PIB/C14 solution. Lines are results of computations, —: 4−mode Giesekus equation, − · −: (in velocity plot only): Carreau-Yasuda equation, − −: 4−mode PTT. Velocities non-dimensionalized with mean velocity U, stresses with $\tau_0 = 3\eta_0 U/R = 236$ (see Table 4.5).*

The stress optical coefficient was determined by fitting the measured 'optical' shear stress ($\Delta n \sin 2\chi$) on the shear stress for the Carreau-Yasuda computation: $C = 1.47 \cdot 10^{-9}\, Pa^{-1}$. This value is surprising, in the sense that it is lower than for the 5% PIB/C14 solution, while molecular theories predict an increase in the stress optical coefficient with increasing concentration (Equation 2.33). We have tried to use our Couette cell as described in Appendix D, but had difficulties with the experiment due to the high stresses (Schoonen [98]).

Axial velocities along cross sections Good agreement is found between measured and computed axial velocities along cross sectional lines in case of all three models (Figure 4.25). Some differences exist near the downstream centerline, which will be discussed next.

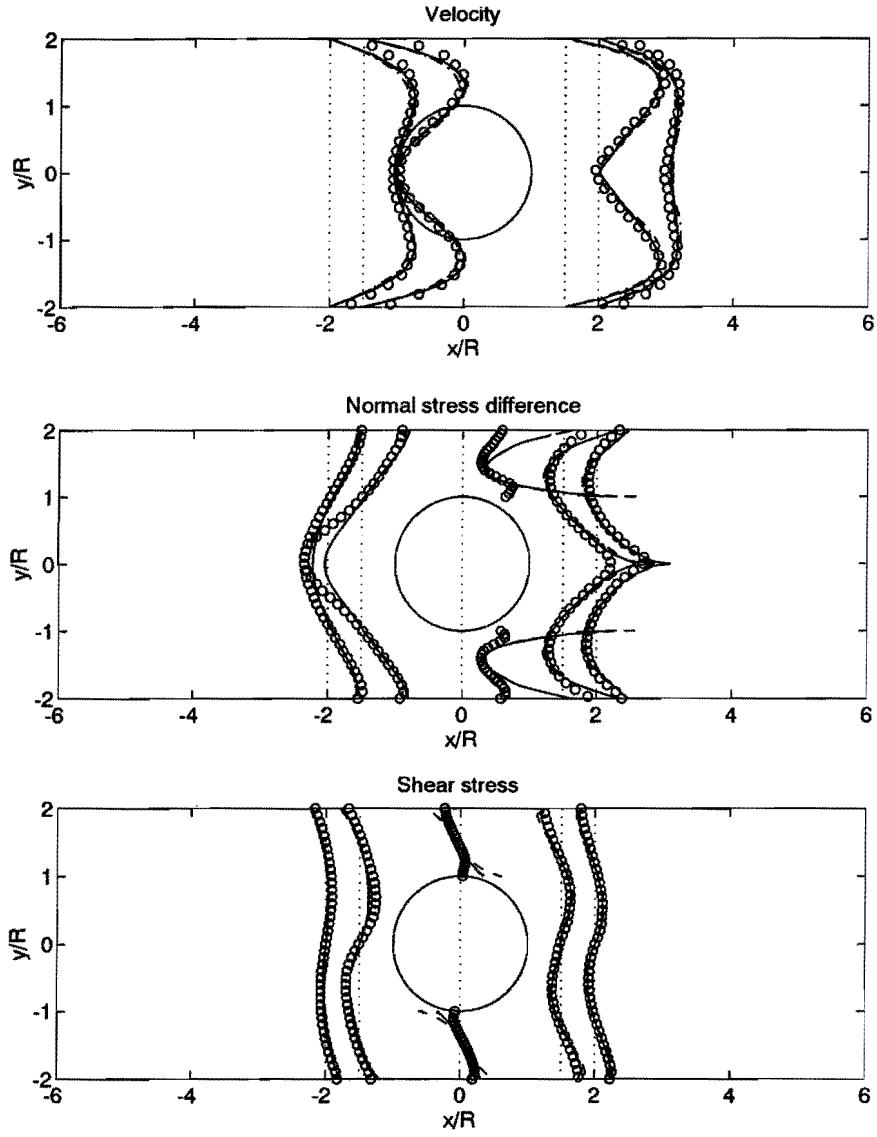

Figure 4.25: *Measured (o) and computed velocity (top), first normal stress difference (middle) , shear stress (bottom) (—: 4−mode Giesekus model, − · −: Carreau-Yasuda model (velocities only), − −: 4−mode PTT) for 9% PIB/C14 solution. Velocities are non-dimensionalized with the mean velocity U, and the stresses with* $\tau_0 = 3\eta_0 U/R = 236$ *(see Table 4.5).*

Axial velocity along axial lines The upper left plot in Figure 4.26 shows measured and computed axial center line velocities. Upstream of the cylinder, the viscoelastic computations agree well with the measured data and better than the Carreau-Yasuda equation. Downstream of the cylinder, the reverse situation is observed: here the Carreau-Yasuda equation agrees excellently with the measured data, while the viscoelastic models have a small overshoot that is not present in the measured axial velocities. However, differences are small.

The lower left plot in Figure 4.26 shows the results along the line at $y/R = 1.5$. Only small differences exist between the model predictions, and fairly good agreement exist between those data and the measured velocities. It appears that the computed data is somewhat shifted compared with the measured data.

Stresses along cross sections Along both upstream and downstream cross sections, the computed normal stress difference for the PTT and the Giesekus model agree well with measured normal stress differences, except near the centerline (Figure 4.25). Upstream of the cylinder, the predicted normal stress differences near the centerline are smaller than the measured stresses, while downstream of the cylinder they are larger in a small region along the centerline. Only small differences exists between the two viscoelastic computations at any position.

The most pronounced differences between computations and measurements are found along the cross sections at $x/R = 0$: the predicted normal stress differences near both the confining walls and the cylinder walls are much larger than for the measured data. In particular near the cylinder wall the differences are remarkable: the measured stress is then decreasing towards the wall while the computations predict a strong rise. One should be careful with the interpretation this discrepancy is an error of the viscoelastic models. Some marginal notes must be made with respect to the measurements here. The measured stresses near the cylinder wall might be less accurate due to the averaging of the large stress gradients over the measuring area. This area has a dimensionless diameter $0.30/2 = 0.15$, which corresponds precisely with the region near the cylinder where stresses are decreasing towards the wall. Possibly, the birefringence measurements have been influenced by reflections on the dielectric surface of the cylinder, that caused phase disturbances of the measured light. Also, partial occlusion of the laser by a wall (either the cylinder or the confining wall) can have influenced the measurement. The computed result seems to be physically more realistic since the high shear rates near the cylinder surface would give high normal and shear stresses. However, the computations may suffer from an inadequacy of the model parameters in the viscoelastic models. From the computed velocity field at $x/R = 0$, the shear rate at the cylinder wall was determined here at $300\,s^{-1}$ and at the confining wall it was $200\,s^{-1}$. These values are far beyond the range in which the non-linearity parameters have been fitted (there $\dot{\gamma} < 70\,s^{-1}$, see Figure 4.22).

The differences near the confining wall at $x/R = 0$ are probably at least partly due to the high stress gradient at this position relative to the size of the measuring area of the laser beam.

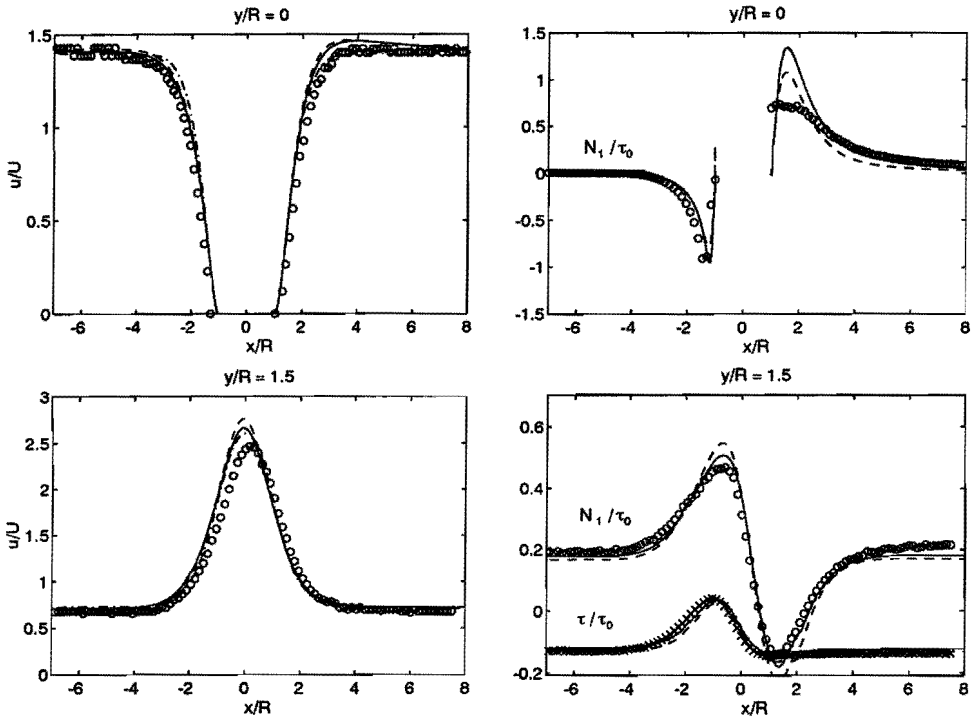

Figure 4.26: *Velocities (left) and stresses (right) along line of symmetry $y/R = 0$ (top row) and along line $y/R = 1.5$ (bottom row) for the 9% PIB/C14 solution. Lines are results of computations, —: 4−mode Giesekus equation, − · −: Carreau-Yasuda equation (velocity only), − − : 4− mode PTT. Velocities non-dimensionalized with mean velocity U, stresses with $\tau_0 = 3U/R$.*

The computed and measured shear stresses agree excellently downstream of the cylinder. Upstream of the cylinder some small differences are found, but agreement is still good. Along the line at $x/R = 0$ differences exist near the walls, as was also the case for the normal stress differences.

Stresses along axial lines Along the centerline upstream of the cylinder, good agreement between both computations and measured data is observed (right upper plot in Figure 4.26). Downstream of the cylinder, both models predict a too large maximum of the normal stress difference. Here, the difference between the two models is evident: the Giesekus model shows larger stresses than the PTT model. The plots along the cross sectional lines have shown that this large difference between experiment and models is local.

Both shear stress and normal stress difference as computed with the viscoelastic models along the line $y/R = 1.5$ agree excellently with the measured data. Between the two models only small differences are found, the PTT model is now closer to the measured data.

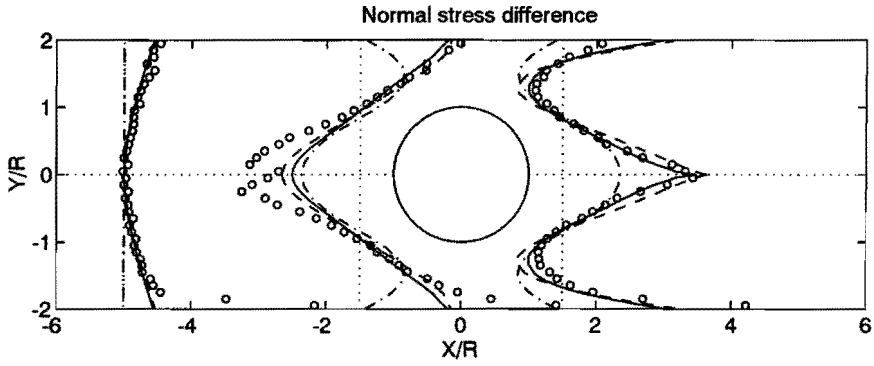

Figure 4.27: *Measured (o) and computed first normal stress difference (—: 4−mode Giesekus, − · −: Carreau Yasuda, − −: 4−mode PTT) . Stress is non-dimensionalized with* $\tau_0 = 3\eta_0 U/R = 158\,Pa$.

4.6 Discussion

This section consists of two parts: first some additional results for the flow of 5% PIB/C14 past a symmetrically confined cylinder are presented (Subsection 4.6.1). Second, a measurement analysis is given in Subsection 4.6.2.

4.6.1 Additional results for the flow of 5% PIB/C14 past a symmetrically confined cylinder

Stresses for four mode Giesekus model and Carreau-Yasuda model In Section 4.3, in case of the four mode PTT model the differences between computed and measured flow fields were most pronounced and $De_1 > 1.36$. In Figures 4.27 and 4.28 results of two additional computations are presented.

First, to investigate further the sensitivity for the choice of the constitutive equation, the four mode Giesekus equation has been applied (with parameters as in Table 3.2) at the highest Deborah number ($De_1 = 2.31$). Only the results for the stress field are shown in Figures 4.27 and 4.28: the results for the velocity field could not been distinguished from those of the four mode PTT model (Figure 4.14) and are not presented here.

Second, to illustrate the typical stress patterns as predicted by the Carreau-Yasuda model these have been plotted too in Figures 4.27 and 4.28, although the stress optical rule can only be understood by viscoelastic theory (see Section 2.3.2). The plotted stresses are the results of the same computation for which the velocities have been presented in Figure 4.14.

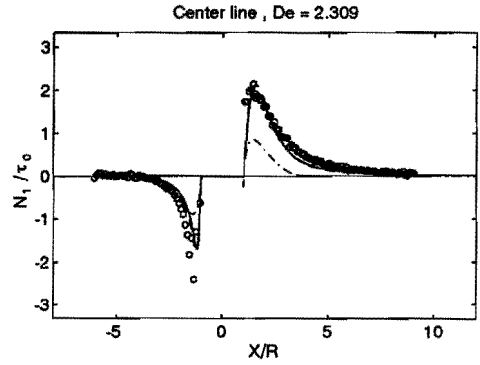

Figure 4.28: *Measured (o) and computed first normal stress difference along the center line in the geometry with the symmetrical confined cylinder (—: 4−mode Giesekus, − · −: Carreau Yasuda, − −: 4−mode PTT) (non-dimensionalized with* $\tau_0 = 3\eta_0 U/R = 158\,Pa$*).*

Both Figure 4.27 and 4.28 show that the differences between the four mode versions of the PTT and Giesekus models are small. Downstream of the cylinder, the four mode Giesekus model improves the agreement somewhat for the first normal stress difference.

The profiles for the normal stress difference of the Carreau-Yasuda model differ in two ways from the viscoelastic models. First, in regions with simple shear deformation (i.e. in the fully developed flow region and near a wall with a no-slip condition) the model predicts zero normal stress difference, as expected.

Second, the maximum of the normal stress difference along the center line downstream of the cylinder is approximately 40% of the value measured and also predicted by the viscoelastic computations. This confirms the expectation that higher normal stresses are found in elongational flows in the presence of viscoelasticity.

Influence of a small asymmetry The measured velocities show a small asymmetry in the velocity profiles downstream of the cylinder. This is explained by an asymmetry in the geometry, i.e. the center of the cylinder is closer to one of the side walls. To investigate this in detail, a simulation has been carried out with the center of the cylinder shifted $0.1\,mm$ towards one of the side walls. The four mode PTT model has been used for the 5% PIB/C14 solution with the same parameters as before ($De_1 = 2.31$). The mesh used has 2407 elements with 5108 nodes. The results are compared with measured data in Figure 4.29.

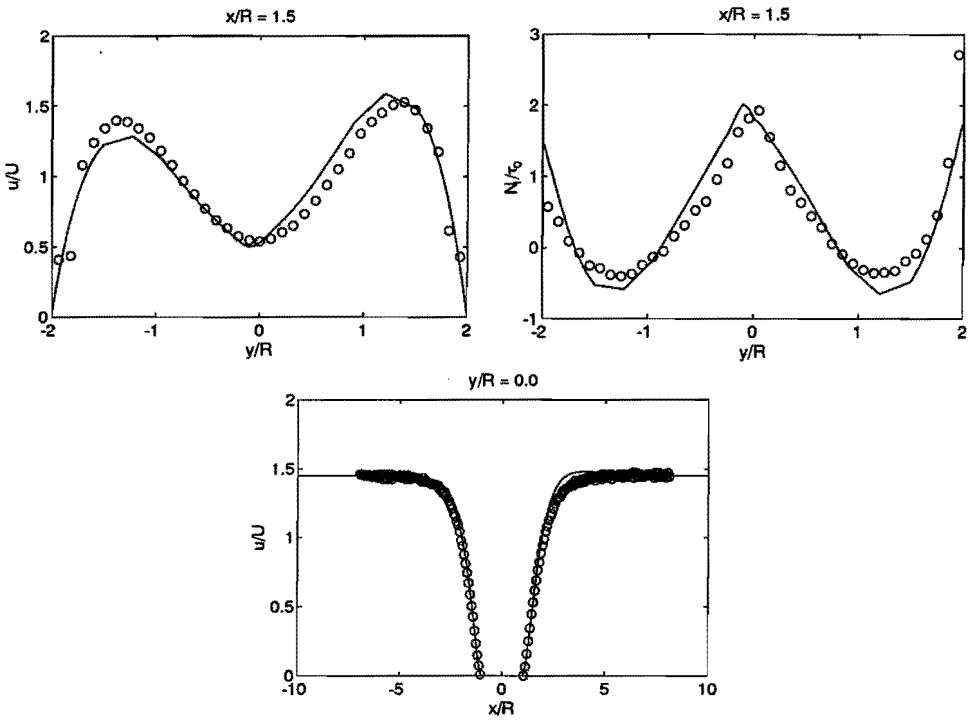

Figure 4.29: *Influence of a small asymmetry in the numerical simulation (5% PIB/C14 solution, $De_1 = 2.31$, (o): experiment, —: 4 mode PTT): (top left) velocity at $x/R = 1.5$, (top right) first normal stress difference along the same line, (bottom) velocity along center line.*

Evidently, the asymmetry in the computed velocity profile at $x/R = 1.5$ is larger than in the measured data. The velocity appears to be very sensitive for the asymmetry. It is concluded that a cylinder displacement of less than 0.1 *mm* relative to the exact symmetric case causes a larger asymmetry in the flow field than observed in the measured velocity profiles. Such a small error is within the tolerance of the construction of the flow cell. The computation also shows that the first normal stress difference along the cross sectional line $x/R = 1.5$ is less sensitive for the asymmetry (figure 4.29) than the axial velocity profile.

Influence of numerical method The results of the finite element computations for the viscoelastic models can be affected by the accuracy of the numerical method (see for example Debae et al. [29]). Therefore, a comparison has been made for three different numerical techniques in case of the flow of a 5% PIB/C14 solution past a symmetrically confined cylinder at $De_1 = 2.31$. The four mode PTT fit was used.
Some of the results are shown in Figure 4.30. The method used in the previous sections of

of this chapter is referred to with 'SI' ('Streamline Integration') , one technique is referred to with 'DG' ('Discontinous Galerkin'), and the third technique is referred to with 'OS' ('Operator Splitting'). Details of the definition and implementation of these latter two methods can be found in Baaijens [6] and Baaijens [9] respectively. The results with 'DG' presented here are from Selen [102]. The 'OS' method will also be used in Chapter 5, where it will be described in more detail.
From Figure 4.30 it is concluded that excellent agreement is found between all three methods. This gives confidence that the viscoelastic finite element simulations are accurate.

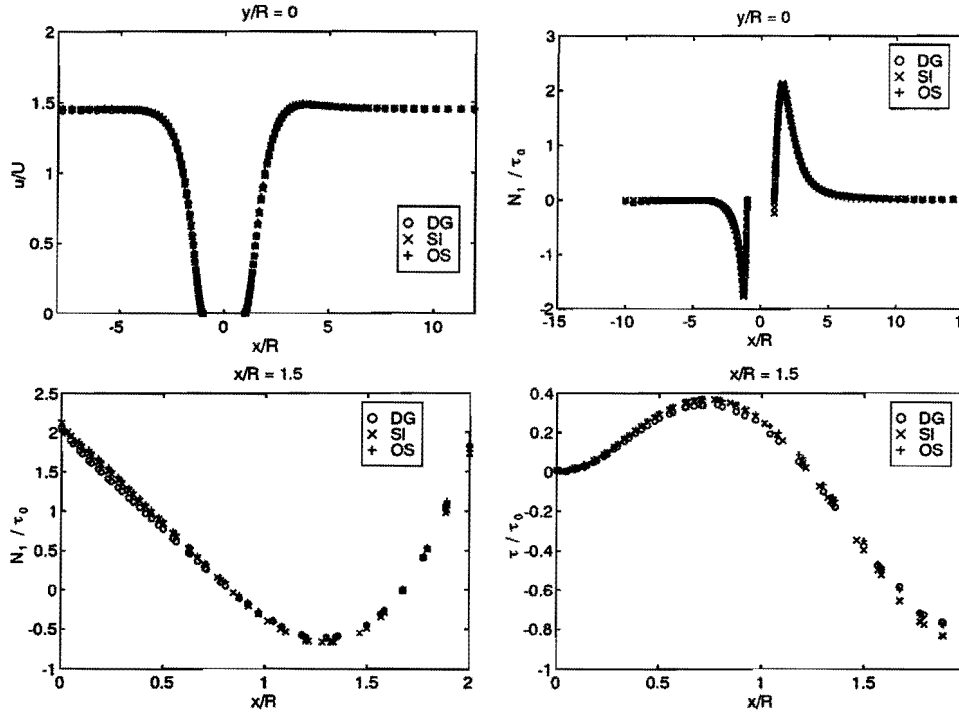

Figure 4.30: *Results for three different numerical methods (DG: Discontinuous Galerkin, SI: stream line integration, OS: operator splitting, see text), in case of flow of 5% PIB/C14 solution past a symmetrically confined cylinder at* $De_1 = 2.31$. *Velocity and stresses are non-dimensionalized with mean velocity* U *and* $\tau_0 = 3\eta_0 U/R$ *respectively.*

4.6.2 Measurement-error analysis

Spatial resolution of FIB measurements Stresses were measured with the pointwise FIB technique described in Section 2.3. Measurements were done with a lens with focal length $400\,mm$, which would (according to Gaussian theory) result in a beam radius of $\approx 0.16\,mm$ at the entrance and exit planes of the flow cell (see Appendix C). In the first experiments (Sections 4.3 and 4.4), this resolution was not achieved, and with a 'knife-edge' experiment (see also Galante [40]) the maximum beam radius was found to be $\approx 0.35\,mm$ in case of the lens with $f = 400\,mm$ (Section 4.3) and $\approx 0.25\,mm$ in case of the lens with $f = 200\,mm$ (Section 4.4). This large deviation from theory is partly due to the non-Gaussian behavior of the beam of the diode laser (i.e. the intensity distribution over a cross section is not Gaussian), as was measured with the Optical Beam Profiler (Melles Griot). However, the primary cause was a too large beam deviation of the rotating halfwave plate. The beam deviation is defined as the angle between the direction of the beam after passing through the optical element with the direction of an incident beam that is normal to the plane of the element. Nevertheless, the accuracy of the measurements was still good, as has been demonstrated in the fully developed flow region.
In later experiments (Section 4.5) this problem was solved by replacing the rotating halfwave plate with one that had a much smaller beam deviation (see Section 2.3.4). The result was, in combination with a lens with $f = 800\,mm$, a beam with a cross sectional radius of $\approx 0.15\,mm$ at the exit and entrance planes, close to the expected value ($0.12\,mm$, Appendix C); note that the beam radius decreases along the axial direction of the laser beam towards the center of the flow cell with a factor $\frac{1}{\sqrt{2}}$).

Noise level of FIB measurements In terms of the dimensionless ratios R_1 and R_2 (see Equations 2.38 and 2.39), the resolution of the birefringence measurements was $\pm 0.01[-]$. In the present experiments this resulted in a noise level for the birefringence of $\approx \pm 2.3 \cdot 10^{-8}[-]$. This is a noise of $\approx \pm 10\,Pa$ for the first normal stress difference and for the shear stress of $\approx \pm 5\,Pa$.

Influence of viewing windows on FIB measurements As a result of the clamping of the flow cell windows, stresses are distributed non-homogeneously in these windows. This might introduce an offset in the birefringence measurement that varies with position. In the absence of flow, no significant spatial variation of the off-set levels was observed in the signals R_1 and R_2, due to the special, extremely low birefringent glass that was used [1]. This enabled elimination of these off-sets by simply measuring them in several points and subtracting the average from the measured signal during flow (see also Galante [40]). The correctness of this procedure was confirmed by the fact that the offsets, measured as described here, corresponded perfectly to the measured signals at the centerline in the

[1] Except at the lowest flow rate used (Figure 4.10), where the birefringence level was so low that it had the same magnitude as the background signal; no special procedure to account for this small spatial variation was used, however.

developed flow region where theoretically both R_1 and R_2 are zero (because stresses are then zero). These signals at the center line were also invariant with flow rate, as expected.

Spatial resolution of the LDA measurements The measuring volume is an ellipsoid with dimensions of $50 \times 50 \times 200\,\mu m$ (see Section 2.2.3). The longest dimension of the ellipsoid is directed along the bisector of the two intersecting beams. In the present set-up this implies that the longest side of the measuring volume is lying in the 2-direction, i.e. along the gradient of the velocity field. This is not optimal for the velocity measurements itself, but it was chosen because then the velocity in the 1-direction could be measured in the areas just upstream and downstream of the cylinder. Moreover, it enabled the (quasi-)simultaneous measurement with LDA and FIB, since the FIB system analyzes a laser beam that has been transmitted through the flow cell along the 2−direction.

The spatial resolution is also affected by the accuracy of the traverse system, which is according to its specifications $0.01\,mm$.

Resolution of the velocity measurements The spatial gradient of the velocity field in the measuring volume results in a statistical distribution of the measured samples around a central value. The measured distributions were Gaussian, and the average velocity was estimated with the root-mean-square value. Only near the bounding walls of the flow cell near the cylinder, where large velocity gradients were present, significant distortions of the ideal Gaussian shape of the histogram of the acquired samples were observed. This made the mean value less accurate at those positions.

The error bound for the velocity measurements was estimated with $3\sigma/\sqrt{N}$, with σ the standard deviation of the mean value for the velocity and N the number of samples ($N = 100$). This error bound was $\leq 3\%$ and mostly $< 1\%$ for the four highest Deborah numbers. In case of the lowest Deborah number, these numbers were a factor two higher. Near the confining walls (within $\approx 0.25\,mm$) relatively large errors exist that can rise up to 100%. This is due to the large velocity gradients combined with low velocities.

The LDA signal is created by the scattered light from particles that are moved by the surrounding fluid. The quality of this signal depends on the properties of the particles: (i) for backscatter measurements, the reflecting area of the particles must be large enough to detect the scattered light ($\mathcal{O}(10)\,\mu m$, Goldstein [45]), (ii) when the size of the particles is much larger than the fringe spacing in the measuring volume, the signal-to-noise ratio diminishes, (iii) particles might not follow the motion of the fluid due to slipping and/or to buoyancy forces.

The buoyancy force on a particle is a result of the density difference between particle and surrounding fluid. The steady rise velocity u_r depends on the balance between buoyancy force and the drag force on the particle, and is for a Newtonian fluid given by (Schraub et al. [100]):

$$u_r = \frac{(\rho_f - \rho_p)}{18\eta} g d_p \tag{4.12}$$

where ρ_f and ρ_p represent the density of the fluid and the particles respectively, d_p the

diameter of the particle, g the gravitational acceleration and η the viscosity. For the high viscosity fluids ($\eta = 1\,Pa\,s$) and the Iriodine particles, it follows that $u_r \approx 2 \cdot 10^{-7}\,m/s$. Thus the effect of the buoyancy forces can be neglected.
The response of the particles to a change in the fluid velocity can be expressed by the maximum frequency f_{max} that they can follow (Hinze [52]):

$$f_{max} = 0.023 \frac{35\eta}{(2\rho_p + \rho_f)d_p^2}, \tag{4.13}$$

which is here (with data as above) approximately $4 \cdot 10^{12}\,Hz$. Thus slippage can be neglected (again by the small size of the particles and the high viscosity of the fluid).
The Doppler signals are processed binary in the LDA hardware with a minimum resolution for the velocity of $0.26\,mm/s$ (Section 2.2.3). The overall resolution of the velocity measurements has been shown in Section 4.3.3.

4.7 Summary and conclusions

The flow of well-characterized polyisobutylene solutions has been studied for the steady planar flow past a confined cylinder. Two model fluids were used: a 5% PIB/C14 solution and a 9% PIB/C14 solution. In case of the 5% PIB/C14 solution both a symmetrically and an asymmetrically confined cylinder geometry were used.

Stable, nominally two dimensional flow was established in a flow cell through which the fluid was pumped continuously, with constant rheological properties as measured in simple shear flow. The experimental methods that were used (FIB and LDA) enabled spatially resolved, pointwise measurement of stresses and velocities respectively. Computations were performed with finite element methods for a generalized Newtonian constitutive (Carreau-Yasuda) and two non-linear viscoelastic constitutive equation (the Phan-Thien Tanner B (PTT-B) equation and the Giesekus equation). Accuracy of the measurements was demonstrated in the fully developed flow region by comparison with the computed velocity and shear stress profiles for the Carreau-Yasuda equation.

In case of the flow of the 5% PIB/C14 solution past the symmetrically confined cylinder, downstream of the cylinder the results of the axial velocities for the single mode PTT model deviated qualitatively at all Deborah numbers between 0.93 and 2.31 from the measured velocities. On the other hand, the simple (generalized Newtonian) Carreau-Yasuda equation agreed well. The single mode PTT equation gave an overshoot in the centerline velocity (approximately 1.5 cylinder radii past the cylinder), which was not present in the measurements nor in the results for the generalized Newtonian model. The precise origin of this overshoot is not clear. The agreement was significantly improved by the four mode PTT model, which predicted (almost) no overshoot of the axial velocity. However, some difference still remained. Both single and four mode PTT equations predicted stresses well at Deborah numbers ≤ 1.36 at all sites. At higher Deborah numbers $(1.87, 2.31)$, some differences exist between the two predictions, but both agree well with the measured data. The mentioned deviation between measured velocities and those computed with the single

mode PTT equation demonstrate the extra information that is obtained by measuring both stresses and velocities: for this fit the differences between computations and measurements of the velocity field are larger than in case of the stress field. The four mode Giesekus equation gave similar results as the four mode PTT equation. The results for the normal stresses as presented in this chapter are not in accordance with those from our earlier study (Baaijens et al. [9]). It was found that differences were not caused by differences between the flow cells, but that the only explanation left is a change of the fluid properties in the earlier experiments. The cause of this change has not yet been traced back.

In case of the flow of 5% PIB/C14 past the asymmetrically confined cylinder, the four mode PTT model agrees excellently with almost all measured data. The overall agreement is impressive. Differences that exist at some sites in the velocity field can (at least) partly be attributed to the inaccuracy of the viscosity fit for the PTT model at higher shear rates. Unexpectedly, also the Carreau-Yasuda model describes the velocity profiles well, although some significant differences exist downstream of the cylinder. There is no effect of viscoelasticity on the velocity field upstream of the cylinder, contrary to expectations that were raised by results in literature (see Section 1.4). This is probably due to the competition of shear thinning and elongational thickening that counteract in the narrow gap between cylinder and wall.

In case of the flow of a 9% PIB/C14 solution past a symmetrically confined cylinder at a Deborah number as high as 5.6, good agreement with measured axial velocities was found in case of the computations with the four mode PTT and Giesekus equations and the Carreau-Yasuda equation. The results for velocity field of the two viscoelastic computations agree within 1%. The maximum of the computed normal stress difference along the center line was approximately a factor two higher than in case of the measured data. Here, the predictions of the two viscoelastic models were practically the same. Differences between measured and computed stresses were remarkably large near the confining walls of the gap between the cylinder and the outer wall. In case of this fluid, the rheological properties were changed after an initial period of use in the complex flow system. This problem was pragmatically solved by fitting model parameters of the constitutive equations on viscometric data obtained with the used fluid. However, such changes are undesirable and in future research the question how to avoid this should be dealt with.

Overall, it is concluded:

- The experimental methods used (LDA and FIB) proved to be powerful tools to study the rheological behavior in the complex flows investigated.
- The agreement between three different finite element techniques confirms the accuracy of the viscoelastic computations.
- Typically, at higher Deborah numbers ($De > 1$) near the line of symmetry just upstream and downstream of the symmetrically confined cylinder, significant differences are found between the computations with the single and four mode PTT model. The four mode PTT model gives more realistic predictions of the velocity field and the stress field than the one mode model and should therefore be preferred.

- In the geometry with the asymmetrically confined cylinder, the agreement between viscoelastic computations with a four mode PTT or Giesekus model and measured velocities and stresses is excellent. This is impressive, since such excellent agreement has not been shown in literature before.
- The generalized Carreau-Yasuda model can describe the velocity field accurately in the flows investigated. Since the Carreau-Yasuda model can not describe normal stresses realistically, this implies, for the combination of material and flow considered, there is no strong influence of elongational stresses on the velocity field.

Chapter 5

Flow of LDPE melt past a confined cylinder

5.1 Introduction

Isothermal flows of a low density polyethylene melt (LDPE) melt at $190°C$ past a confined cylinder are studied at two Deborah numbers by means of comparing measured isochromatic birefringence patterns with those that are computed with a finite element method [1]. Both a symmetrically and an asymmetrically confined cylinder are used. To evaluate the adequacy of viscoelastic constitutive equations, two different equations have been used: the Phan-Thien Tanner-A model (PTT-A) and the Giesekus model (see Section 1.2). To the author's knowledge, the preliminary results presented below constitute for a polymer melt the first detailed comparison of finite element computations with measured birefringence patterns in the (strong) flow past a cylinder.

5.2 Experimental aspects

5.2.1 Experimental set-up

The flow cell is fed with the LDPE melt by a corotational twin screw extruder (Werner and Pfleiderer ZSK-25). During all experiments, the melt temperature was controlled at $190°C$. Fringe patterns were observed with optical systems for fieldwise measurements of birefringence patterns.

The flow cell was designed and manufactured in our group. It is made of steel (100 MnCrW4) and has four changeable windows in the lateral walls, two on each side, that are made of BK-7 glass (Schott [99]) and have radius $50\,mm$ and thickness $15\,mm$. The height of the channel is $5\,mm$ and the depth in the neutral direction is $40\,mm$ giving an aspect ratio of $1:8$. This ratio is assumed to be sufficiently large to create a nominally two dimensional flow and small enough to yield relatively high Deborah numbers, given

[1] This chapter is based on the master's thesis of Kruijt [65].

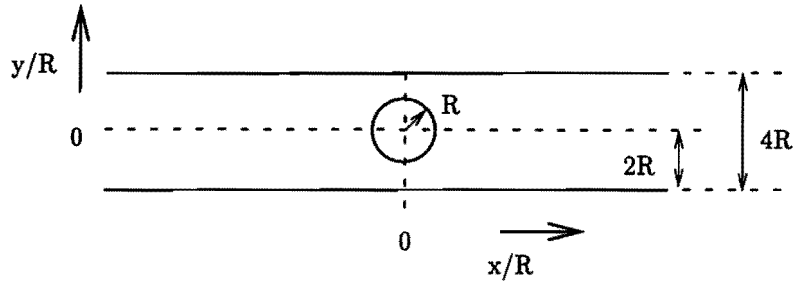

Figure 5.1: *Schematic cross sectional view of geometry with symmetrically confined cylinder. Radius R of the cylinder is 1.25 mm, height of the channel is $4R$, depth D (in the direction perpendicular to the plane of drawing) is $32R$ and total length in x direction is $256R$. Center of cylinder is at $x = 0, y = 0$. Mean flow is in positive x direction.*

the maximum throughput of the extruder and the minimal size of the cylinder (necessary to resists the force of the melt without bending more than a few percent of the cylinder radius). The length of the channel in the mean flow direction is 320 mm.

A rod of Wolfram with radius $R = 1.25\,mm$ was placed in blind holes in two opposite windows. To avoid damage due to contact between the cylinder and the glass, Teflon was used between the rounded ends of the cylinder and glass. In the asymmetric geometry, the rod was positioned $0.6R$ towards the upper wall. The center of the cylinder is kept (by definition) at $x/R = y/R = 0.0$. The flow domain of interest is illustrated schematically in Figure 5.1.

The flow cell is heated with eight heating elements (Hasco Z110, 400 W), that are located in pairs directly under and above the slit and near the entrance and exit of the flow cell. These elements are controlled by a four channel temperature control unit (Hasco Z126) and four thermocouples (Hasco Z1295/5) that are located between two elements in the walls of the flow cell. Isothermal flow conditions are assumed in the sequel.

The fieldwise measurement of birefringence is described in Chapter 2, which also contains details about the equipment used.

Results will be presented for each geometry at two flow rates, that are listed in Table 5.1.

5.3 Computational aspects

5.3.1 Constitutive equations and parameters

Details of the rheology of the LDPE (DSM, Stamylan LD 2008XC43) are described in Section 3.7, together with values of fitted parameters. Here, four mode versions of the

	$U\,[m/s]$	$U/R\,[s^{-1}]$	De_1
symmetric			
	$8.06 \cdot 10^{-3}$	$6.45 \cdot 10^{0}$	4.8
	$1.49 \cdot 10^{-2}$	$1.19 \cdot 10^{1}$	8.0
asymmetric			
	$9.94 \cdot 10^{-3}$	$7.95 \cdot 10^{0}$	5.1
	$1.64 \cdot 10^{-2}$	$1.31 \cdot 10^{1}$	9.8

Table 5.1: *Parameters characterizing flow conditions during the experiments with LDPE in the symmetrically and asymmetrically confined cylinder geometry: mean velocity U, characteristic shear rate U/R (R: radius of cylinder), Deborah number De_1 according to Definition 1.10.*

PTT model and of the Giesekus model have been used, both having proved to be capable of fitting the material functions in steady shear (Section 3.7). Four mode fits instead of the eight mode fit of Tas [107] (that were also listed in Section 3.7) were used to reduce computation times.

In case of the PTT model, two parameter sets have been used in the sequel: ($\xi = 0, \epsilon = 0.2$), and ($\xi = 0.1, \epsilon = 0.1$). Both sets fit $\eta(\dot{\gamma})$ and $N_1(\dot{\gamma})$ equally well, but differ in their prediction of elongational viscosity (see Figure 5.2). For the Giesekus model $\alpha = 0.25$ has been used. Also, computations with a (generalized Newtonian) Carreau-Yasuda model have been performed with parameters $\eta_{cy}, \lambda_{cy}, n_{cy}, a = \{2.45 \cdot 10^3\ Pa, 1.64 \cdot 10^{-1}\ s, 3.66 \cdot 10^{-1}, 1\}$. The results for the upper convected Maxwell model (UCM) are plotted for reference.

5.3.2 Numerical method

The finite element method of Baaijens [6] has been used as implemented within the code of the SEPRAN package by Selen [102]. Details can be found also in Baaijens [7]. Operator splitting is used to create two (coupled) problems that are solved via an iterative procedure in a decoupled fashion.

The operator splitting refers to a special treatment of the material time-derivative of the extra-stress tensor in the constitutive equation. This derivative, defined by

$$\frac{D\boldsymbol{\tau}_i}{Dt} = \frac{\partial \boldsymbol{\tau}_i}{\partial t} + \vec{v} \cdot \nabla \boldsymbol{\tau}_i \tag{5.1}$$

is approximated by

$$\frac{D\boldsymbol{\tau}_i}{Dt} \approx \frac{\boldsymbol{\tau}_i(\vec{x}, t_n) - \boldsymbol{\tau}_i(\vec{p}, t_{n-1})}{\Delta t} \tag{5.2}$$

where $\vec{p}$ is the position of a particle at time t_{n-1} that is at position $\vec{x}$ at time t_n and $\Delta t = t_n - t_{n-1}$.

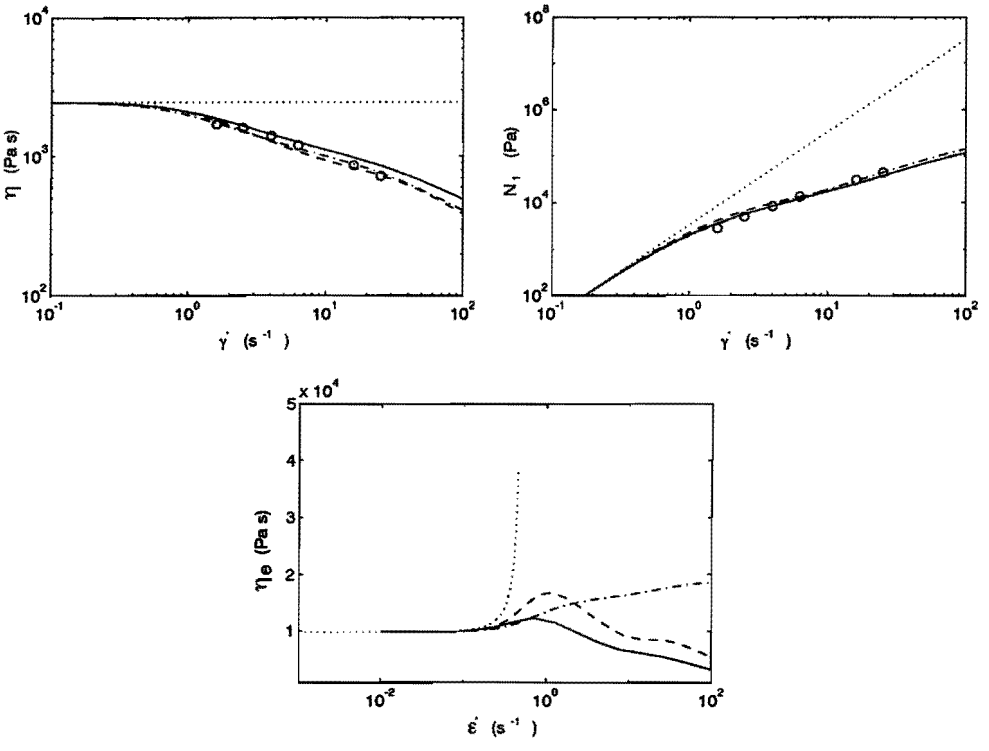

Figure 5.2: *Material functions for LDPE at 190°C in steady simple shear flow (top left: viscosity $\eta(\dot{\gamma})$, top right: first normal stress difference $N_1(\dot{\gamma})$) together with fitted models and (bottom figure) predictions in planar elongational flow (—: PTT model with $\xi = 0.0$ and $\epsilon = 0.2$, – –: PTT model with $\xi = 0.1$ and $\epsilon = 0.1$, – · –: Giesekus model, · · ·: UCM model).*

The stress $\boldsymbol{\tau}_{p,i} = \boldsymbol{\tau}_i(\vec{p}, t_{n-1})$ is found by integration of the advection (or transport) equation on the interval $[t_{n-1}, t_n]$ with the previously calculated velocity field $\vec{v}$:

$$\frac{D\hat{\boldsymbol{\tau}}_i}{Dt} = 0, \ \hat{\boldsymbol{\tau}}_i(\vec{x}, t_{n-1}) = \boldsymbol{\tau}_i(\vec{x}, t_{n-1}) \tag{5.3}$$

with $\boldsymbol{\tau}_{p,i} = \hat{\boldsymbol{\tau}}_i(\vec{x}, t_n)$. This integration was performed using the time-discontinuous/Galerkin least squares method (TD/GLS), which uses space-time finite element approximations of the stress field (see Baaijens [7]).

Once $\boldsymbol{\tau}_{p,i}$ is known, the stress, velocity, and pressure fields are found using the standard Galerkin method that is applied to the constitutive equation, conservation of momentum equation and conservation of mass equation. The non-linear system of equations obtained after the usual procedure (deriving the weak formulation of the problem, substitution of the finite element approximation and integration over the elements) is solved with a Newton-Raphson iteration. Usually one iteration step sufficed.

The finite element approximation was made with bi-quadratic polynomials for the stress field that are discontinuous over element boundaries, bi-quadratic polynomials for the velocity field and the pressure field was discretized discontinuously with a constant value in each element.

The method is intrinsically unsteady: a steady solution can only be obtained by using as many time increments as necessary to obtain a solution that is constant in time. The sequence of time increments used is listed in Table 5.2. The initial time step size is chosen so that it is not too small (to avoid too many time increments) and not too large (to avoid convergence problems). The computations are finished after 400 increments, corresponding with $2.228\,s$ (which is 2.228 times the maximum Maxwell relaxation time of the LDPE (Table 3.6; the minimum time increment was equal to 0.316 times the smallest Maxwell relaxation time).

To monitor the change of the solution with time, the relative change (referred to as θ in the sequel) of the maximum norm of the solution vector (containing stresses, velocities and pressures in all nodal points) over each increment has been calculated. A typical example is shown in the left plot of Figure 5.3; the 'spikes' in the curve correspond with changes in value of the time increment. This plot illustrates that θ becomes small ($< 1 \cdot 10^{-2}$) after a certain number of time steps with a given increment. Also, in the same figure, the result for N_1 along the center line at $t = 1\,s$ and after $t = 2.228\,s$ is plotted. The differences between the two computations are insignificant.

5.3.3 Mesh

In Figure 5.4, (part of) the meshes are plotted in case of both the symmetrically and asymmetrically confined cylinder. In the first case, the total mesh has 1000 elements with 4221 nodes. The problem solved at each time-step has 8442 degrees of freedom for the velocities and 12663 degrees of freedom for the stresses. In the asymmetrical geometry, these numbers are subsequently 4780, 1148, 9560 and 14340. In the latter case, the mesh is relatively coarse. A typical computation time was 157171 s (43,4 hours) with the mesh used

n_{iter}	Δt
200	$1.00 \cdot 10^{-2}$
50	$3.16 \cdot 10^{-3}$
50	$1.00 \cdot 10^{-3}$
50	$3.16 \cdot 10^{-4}$
50	$1.00 \cdot 10^{-4}$

Table 5.2: *Time increments used during the finite element computations. In total* 400 *time steps were used.*

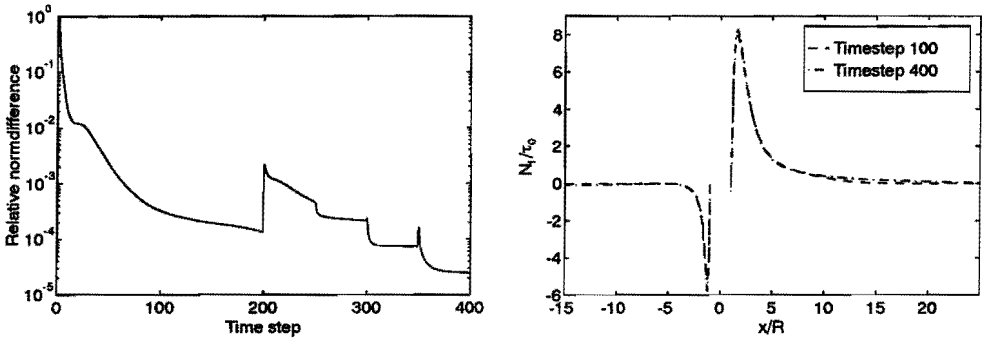

Figure 5.3: *Left: a typical example of the relative difference of the maximum norm of the solution vector as function of number of time increments. Right:* N_1 *along the centerline after two different numbers of increments (step* $100 : t = 1\,s$, $400 : t = 2.228\,s$*).*

here, which for practical reasons hindered strong mesh refinement. In the symmetrically confined cylinder geometry (using the PTT model with $\xi = \epsilon = 0.1$ with $De = 8.0$), a computation on a refined mesh showed no significant difference with the coarser mesh. The refined mesh has approximately 50% more elements than the original; it is in particular refined near the cylinder wall and near the centerline.

5.3.4 Boundary conditions

On rigid walls, the no-slip condition is used. In case of the symmetrically confined cylinder geometry, the symmetry condition along the centerline is prescribed. On the in- and outflow boundaries, a Newtonian velocity profile is prescribed (for convenience) while choosing entrance and exit sections of the computational domain sufficiently long to have fully developed flow regions upstream and downstream of the cylinder. The center of the cylinder is at $x/R = y/R = 0$ (R = radius of the cylinder), the entrance boundary at $x/R = -20$

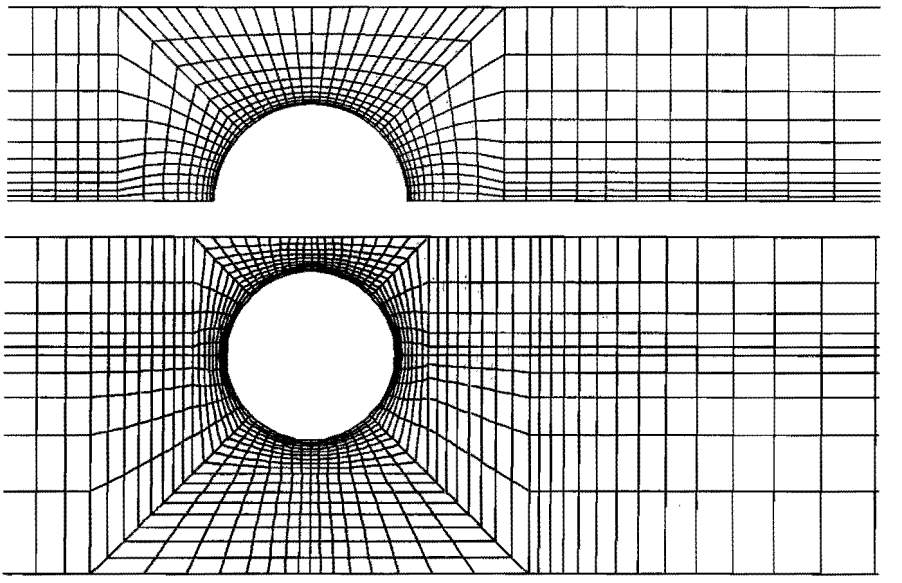

Figure 5.4: *Top: part of mesh used during the computations for the flow of LDPE at* 190°*C through the geometry with the symmetrically confined cylinder. Bottom: same, but now in geometry with asymmetrically confined cylinder.*

and the exit boundary at $x/R = 30$. In case of the symmetrically confined cylinder the confining wall is at $y/R = 2$ and in the asymmetrical case the lateral walls are at $y/R = -2.6$ and $y/R = 1.4$.

5.4 Results

5.4.1 Determination of stress optical coefficient

The stress optical coefficient was determined in fully developed flow by comparing birefringence measurements with computed shear stresses, using the field-wise measurement of birefringence (Section 2.3.3). This method involves multiple experiments. First, the isochromatic pattern (according to equation 2.35) in the fully developed slit flow is photographed (using only the spectral line at 546 nm of the high-pressure mercury light source). Second, the two quarter wave plates are removed. Then also the isoclinics are observed superposed on the isochromatic pattern (Equation 2.34). The polarizer is set parallel with the symmetry axis of the slit. The (single) isoclinic line then coincides with the zero-order isochromatic that is located at this symmetry line. Next, after rotating both polarizer

and analyzer in unison over 10°, a photograph was taken of the shifted isoclinic line (the isochromatic pattern remains unchanged). This has been repeated for subsequent rotations of 10° up to a total rotation relative to the symmetry line of 90°.
The isochromatic lines correspond with extinction of the light at discrete values of the retardation δ (Equation 2.35):

$$\delta = k2\pi, k = 0, \pm 1, \pm 2, ... \tag{5.4}$$

where k is the isochromatic fringe order. From the photograph, the retardation is obtained as a function of the cross sectional position.
The photographs with the isoclinic line as function of the rotation angle give the orientation (or isoclinic or extinction) angle χ as a function of the position. Following McHugh et al. [79], the position of the isoclinic lines has been measured at the edge of the fringe nearest to the symmetry line.
By combining these two sets of data, the quantity $\tau_{opt} = \frac{\Delta n}{2} \sin 2\chi$ has been evaluated at the position of each isochromatic line. The result for the shear stress of a finite element computation with the four mode PTT equation is plotted as function of this measured parameter τ_{opt}. The result is shown in the Figure 5.5 for two sets of data at different De_1 numbers. The stress optical coefficient C follows from a least squares fit of a first order polynom: $C = 1.53 \cdot 10^{-9}\, Pa^{-1}$.

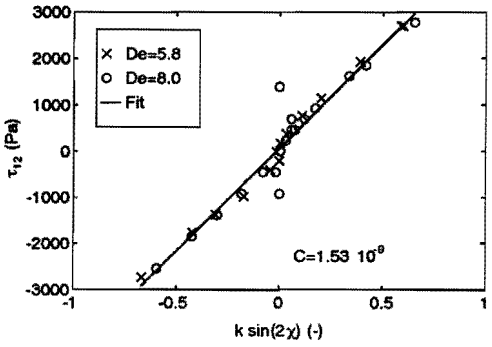

Figure 5.5: *Determination of stress optical coefficient for the LDPE at 190° by fitting the shear stress computed in fully developed flow on measured birefringence data. Experimental data from isochromatic and isoclinic photographs (see text) obtained at two different flow rates. Fitted stress optical coefficient C:* $1.53 \cdot 10^{-9}\, Pa^{-1}$.

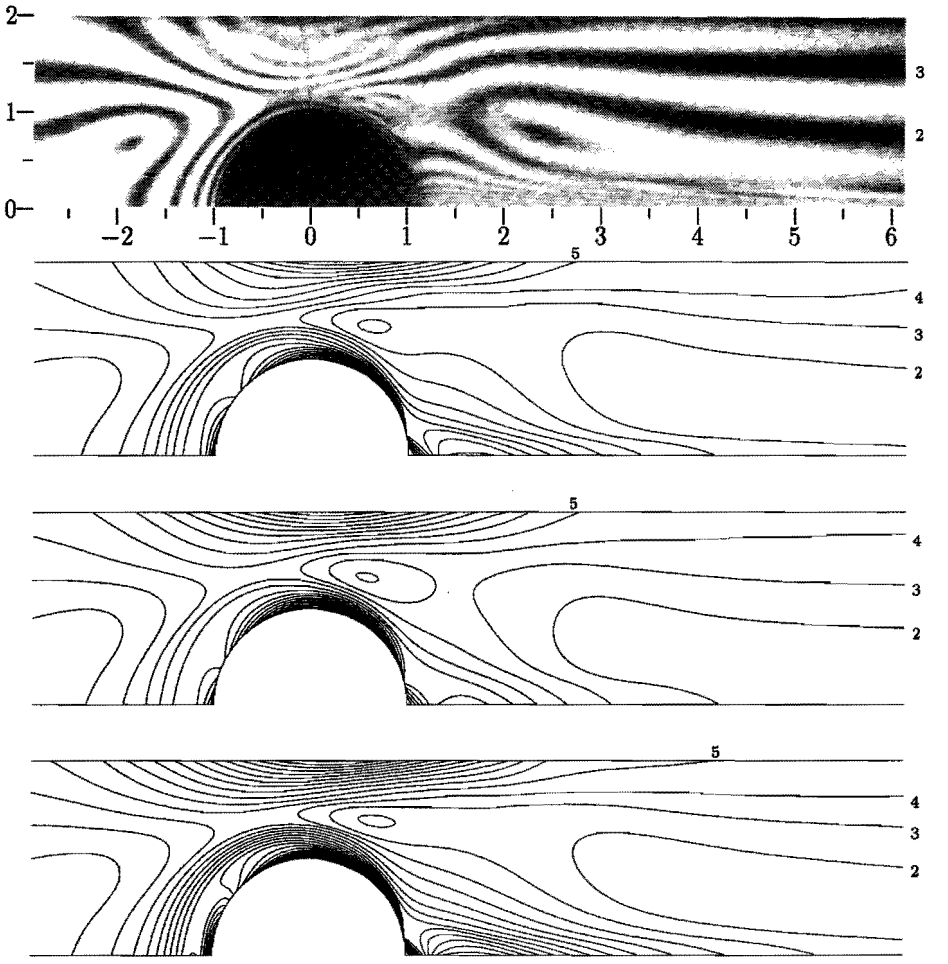

Figure 5.6: *Measured and computed isochromatic patterns at* $De_1 = 4.8$ *for the flow past a symmetrically confined cylinder of a LDPE melt at* $190°C$ *(flow from left to right). From top to bottom: (i) experiment, (ii) PTT-a model with* $\xi = 0.1$ *and* $\epsilon = 0.1$*, (iii) PTT-a model with* $\xi = 0.0$ *and* $\epsilon = 0.2$*, (iv) Giesekus model with* $\alpha = 0.25$.

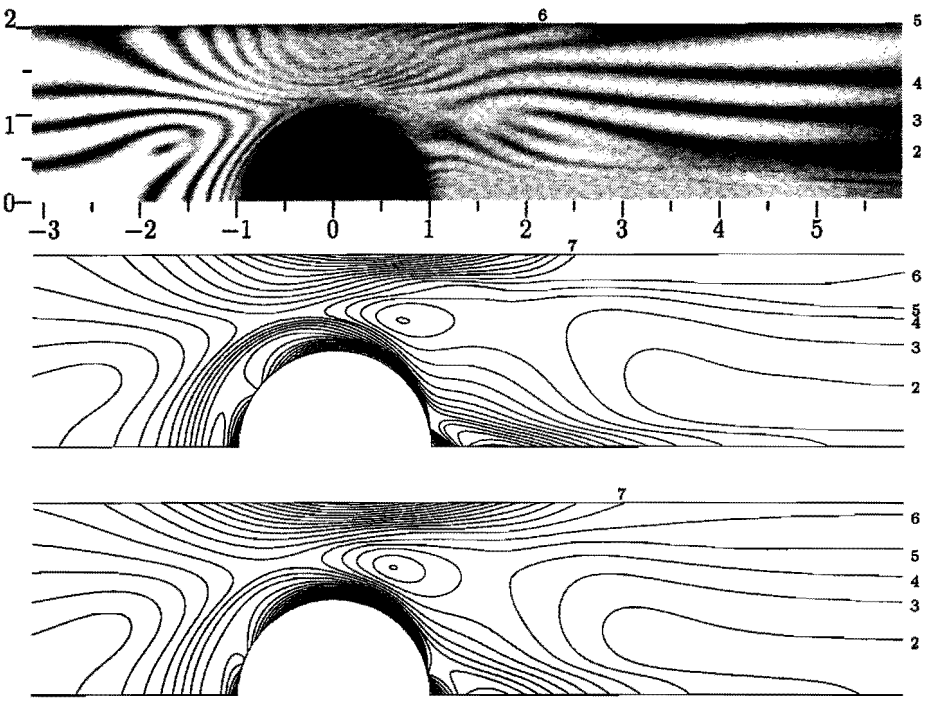

Figure 5.7: *Measured and computed isochromatic patterns at $De_1 = 8.0$ for the flow past a symmetrically confined cylinder of a LDPE melt at 190°C (flow from left to right). From top to bottom: (i) experiment, (ii) PTT-a model with $\xi = 0.1$ and $\epsilon = 0.1$, (iii) PTT-a model with $\xi = 0.0$ and $\epsilon = 0.2$.*

5.4.2 Flow past a symmetrically confined cylinder

A comparison of computations with experiments is presented at two Deborah numbers, $De_1 = 4.8$ and $De_1 = 8.0$, in Figures 5.6 and 5.7 respectively (note that only a part is shown of the spatial domain used in the computations). The photographs are made using the polariscope set-up that gives the isochromatic pattern (Equation 2.35), which corresponds with levels of retardance δ according to Equation 5.4. Since the birefringence $\Delta n = \lambda/(2\pi d)\delta$ (Equation 2.11), the isochromatics correspond with a level of birefringence. The isochromatic patterns of the computations are computed from the solution of the stress field with (using the stress optical rule) $\Delta n = C\sqrt{4\tau^2 + {N_1}^2}$ (Equation 2.36). The results for both situations are discussed next.

$De_1 = 4.8$ At first sight, the computed patterns agree qualitatively well with the measured isochromatic pattern. However, some distinct differences are observed too. The PTT

model with $\xi = \epsilon = 0.1$ and Giesekus model with $\alpha = 0.25$ agree reasonably well with the experiment, while in case of the PTT model with $\xi = 0, \epsilon = 0.2$ the agreement is only moderate.

Most remarkably, fringes on the photograph are more concentrated near the surface of the cylinder and near the downstream center line than in case of the corresponding contour lines in any of the computed plots. This is evident from several details. For example, in the computations just upstream of the cylinder a larger number of contour lines is observed than in the photographed pattern. Most probably, in the photograph the corresponding isochromatic lines are concentrated near the cylinder surface. They can not be resolved because of their concentration and because they are covered by the 'shadowed' boundary around the cylinder surface that is caused by perspective error in the photograph. Also, in the gap between cylinder and wall the measured fringe starting from the confining wall at $y/R \approx -2.0$ nearly touches the cylinder wall before it curves back to the upper wall downstream of the cylinder. In the computations, this fringe does not get that close to the cylinder. Also on the photograph, a closed fringe is observed near the cylinder wall just downstream of the center of the cylinder near $x/R \approx 0.5, y/R \approx 1$, whereas on the computed plots its position is shifted in the direction of the confining wall. Furthermore, downstream of the cylinder the fringes on the photograph are more concentrated along the center line compared with the computations and are directed more parallel with the centerline.

The contour patterns in the wake that are computed with the PTT model ($\xi = \epsilon = 0.1$) and the Giesekus model both resemble the photographed results reasonably well. On the contrary, for the PTT model with $\xi = 0$ and $\epsilon = 0.2$ only a few contour lines are present near the downstream center line and the agreement is poor.

$De_1 = 8.0$ At this Deborah number, only predictions for the two fits of the PTT model could be computed. In case of the Giesekus model, the computations failed after a number of time steps (due to the appearance of a singularity in the system matrix). When comparing the computations with the experiment, qualitatively the same conclusions can be drawn at the lower Deborah number.

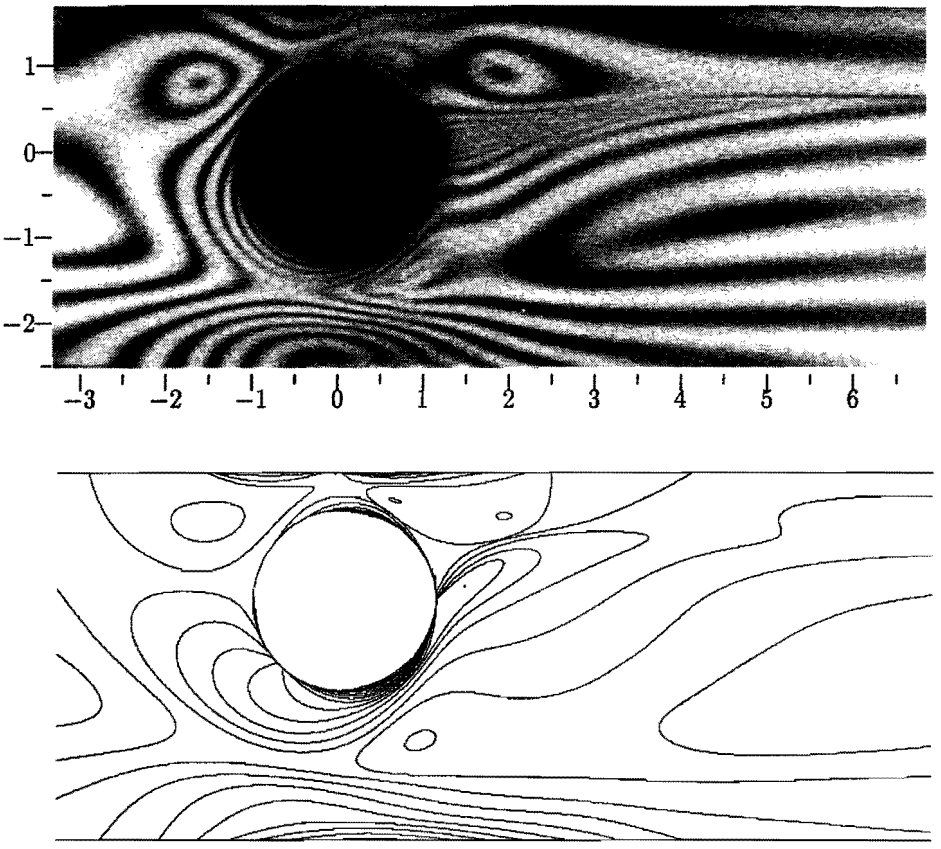

Figure 5.8: *Measured and computed isochromatic patterns at* $De_1 = 5.1$ *for the flow past an asymmetrically confined cylinder of a LDPE melt at* 190°. *Top: experiment. Bottom: PTT model with* $\xi = 0.1$ *and* $\epsilon = 0.1$.

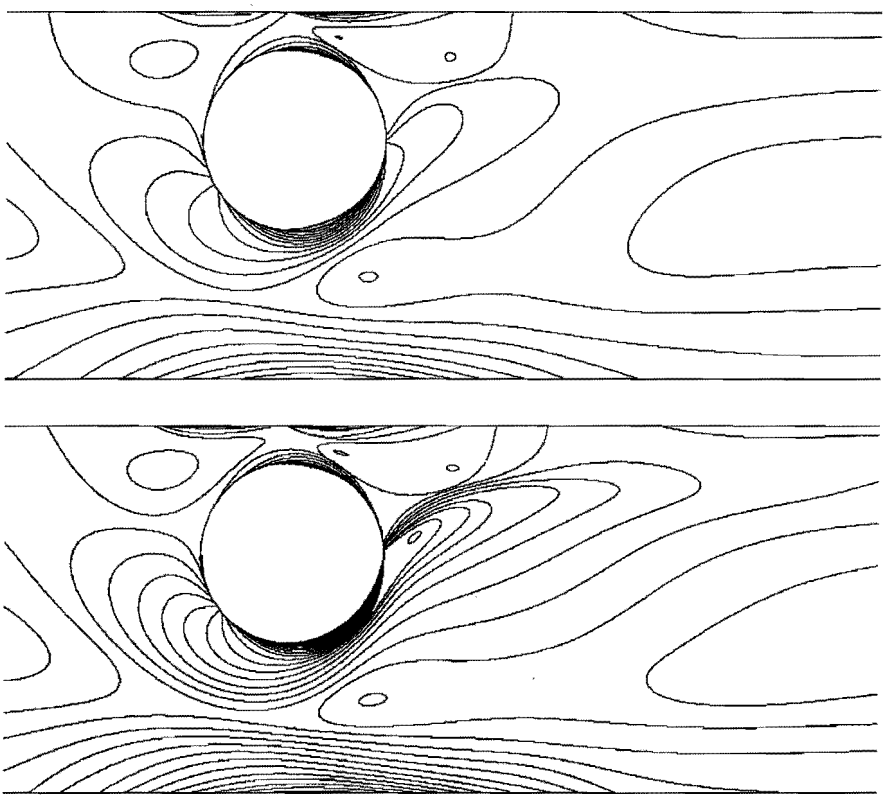

Figure 5.7: *(Continued:) Top: PTT model with* $\xi = 0.0$ *and* $\epsilon = 0.2$*. Bottom: Giesekus model with* $\alpha = 0.25$.

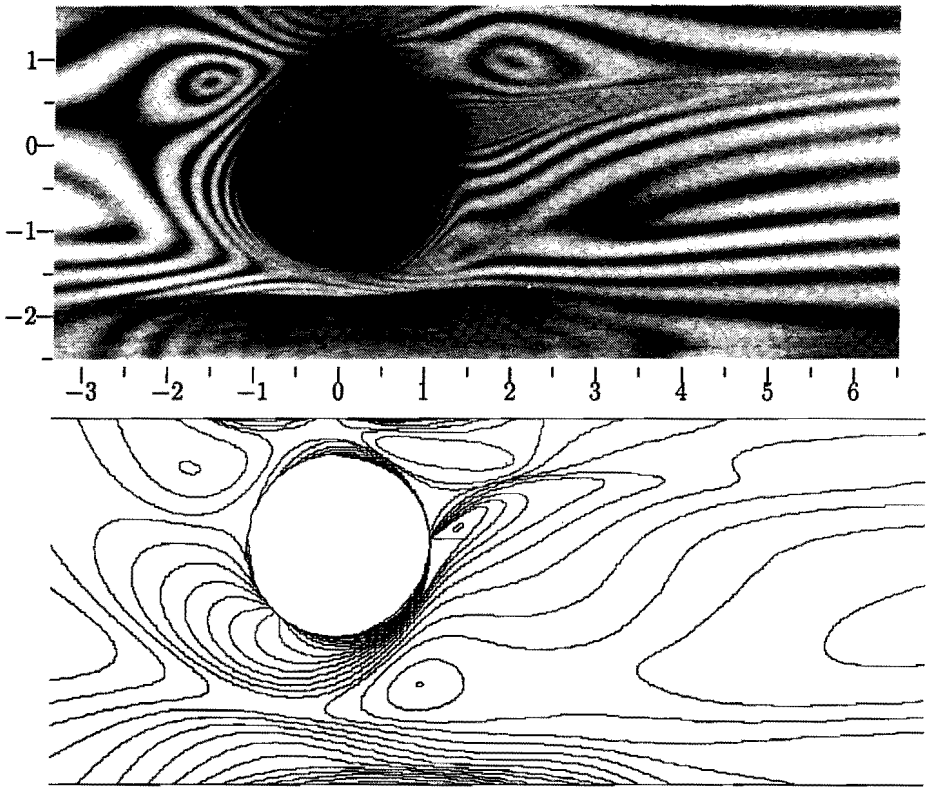

Figure 5.8: *Measured and computed isochromatic patterns at* $De_1 = 9.8$ *for the flow past an asymmetrically confined cylinder of a LDPE melt at* $190°C$. *Top: experiment. Bottom: PTT model with* $\xi = 0.1$ *and* $\epsilon = 0.1$.

5.4.3 Flow past an asymmetrically confined cylinder

In the asymmetrical geometry, the cylinder is placed $0.6R$ closer to the upper wall. The results are presented at the two Deborah numbers (listed in Table 5.1): in Figure 5.8 for the lower Deborah number and in Figure 5.8 for the higher Deborah number.

$De_1 = 5.1$ Qualitatively, the computations all agree with the experiment. The differences between the computations are small. The biggest difference between computations and experiment is observed upstream of the cylinder around $x/R \approx -1.5, y/R \approx -1.5$. Here, the computations show a number of curved contour lines that can not be observed in the experiments. Most probably, similar to the symmetrical case, these lines can not be seen in the photograph, because they are concentrated to close near the cylinder surface. This means that at this site, the measured stresses have larger gradients and that the transition of fully developed flow to the compressive deformation is located more closer to the cylinder surface. Furthermore, in the computations the stress wake is directed more towards the upper wall compared with the experimental result. Thus in the computations the stress relaxation downstream of the cylinder is slower than in the experiment.

$De_1 = 9.8$ In the asymmetrical case, only a solution was obtained in case of the PTT model with $\xi = \epsilon = 0.1$ (computations for the PTT model with $\xi = 0, \epsilon = 0.2$ and the Giesekus model failed due to the appearance of a singular matrix in the computations). As at the lower Deborah number, qualitative agreement with experiments is observed in case of the PTT model.

5.5 Conclusions and discussion

Photographs of isochromatic birefringence patterns were compared with results of finite element simulations. Two geometries were used: a symmetrically and an asymmetrically confined cylinder. Two viscoelastic constitutive models with four modes were used: the Phan-Thien Tanner model and the Giesekus model. The numerical simulations agreed qualitatively with the experiments, the differences between the models were small. Compared with the computations, the measured contour lines were concentrated closer to the cylinder surface, and downstream of the cylinder the stress relaxation was slower. The agreement might be improved by adjusting the model parameters of the constitutive models. If this is not sufficient, the models should be modified.

The finite element computations could not be verified by other numerical techniques, as was done in Section 4.6. The Discontinuous Galerkin technique and the streamline integration method used in that section did not work here. This certainly needs further investigation.

In the present study, it was not possible to measure the velocity field to check the absence of significant three-dimensional effects (because no laser Doppler system was available that could safely be used at the site of the extruder). This should be done in a continuation

study. The birefringence patterns observed were stable and time-independent. Therefore, it is unlikely that time-dependent effects are present in the flows considered.

The temperature distribution was not measured. It is, however, strongly recommended to do this. The addition of a static mixer in between the extruder and the flow cell will improve the homogeneity of the melt temperature in the flow cell.

The fieldwise measurement of the birefringence is particularly suitable to analyze transient flows like start-up of steady flow. To achieve this, a by-pass loop with a three-way valve with a drain and a gear pump should be installed between extruder and flow cell to control the throughput through the flow cell independently of the extruder screw speed.

Chapter 6

Conclusions and recommendations

After the rheological characterization in simple shear flows (Chapter 3), constitutive equations for polymer melts and solutions were evaluated in the complex flow past a confined cylinder (Chapters 4 and 5). This evaluation was accomplished by means of a comparison of measured data of the velocity and/or stress field with results of finite element simulations. Model fluids were used instead of polymer melts in the main part of this study (Chapter 4), which facilitated the analysis both experimentally and computationally. Most results for the complex flow past a cylinder were obtained for a 5% (w/w) solution of polyisobutylene in tetradecane (referred to with 5% PIB/C14). In case of a low density polyethylene (LDPE) melt, a preliminary analysis was made in the same complex geometry (Chapter 5).

6.1 Conclusions

Spatially resolved, pointwise measurements of velocities and stresses were obtained with laser Doppler anemometry and flow induced birefringence measurements respectively. The experimental methods used prove to be powerful tools to investigate the complex flow experimentally and enable a quantitative validation of finite element simulations. The numerical method of Hulsen and van der Zanden [56] was used, as implemented in the finite element package SEPRAN [101]. The accuracy of the viscoelastic computations was demonstrated by a comparison with results of two other numerical techniques (as proposed by Baaijens [6] and Baaijens [9] respectively), which show good agreement. Measured velocities and stresses agree well with the results of finite element computations with two constitutive equations of the differential type: the Phan-Thien Tanner equation of type B (PTT-B) and the Giesekus equation. Models with four modes instead of a single mode improve the agreement remarkably. Differences between the four mode PTT and Giesekus equation are small. In general, the generalized Newtonian model describes excellently the velocity field, implying that for the specific flows investigated little effect of the normal stresses on the velocity field is present. The displacement of the cylinder towards one of the confining walls did not change this observation of the velocity field essentially (although some differences are now found downstream of the cylinder), which is in contradiction with

the expectations raised in literature (e.g Dhahir and Walters [30]). However, a generalized Newtonian model can not predict normal stresses realistically, not even in a qualitative way.

In case of a LDPE melt at 190 °, fieldwise measured isochromatic birefringence patterns were compared with results of finite element simulations with viscoelastic constitutive models (PTT-A and Giesekus). These simulations, performed with the method as introduced by Baaijens [6], gave solutions at Deborah numbers as high as 9.8. In case of the PTT model a solution was obtained at all Deborah numbers, while in case of the Giesekus model the computations failed at the higher Deborah numbers. It was attempted to use the numerical techniques from [56] and [9] as well, but did not give convergent solutions. Measured fringe patterns agreed moderately to well with the computed patterns. Most remarkably, the measured fringes were concentrated near the cylinder surface and the downstream centerline clearly more than were the computed fringes. Most probably, these differences are caused by deficiencies in the models used. In case of the PTT model, it was shown which of two parameter sets, that fitted data in simple shear equally well, produced the most realistic results in the complex flows.

6.2 Recommendations

Recommendations for future research on the use of complex flows to test constitutive equations for viscoelastic liquids and to determine their parameters are listed as follows.

- The discrepancy between the results for the normal stresses found in our earlier study ([9]) on the flow of the 5% PIB/C14 past the symmetrically confined cylinder and those in this thesis can only be explained by a change in the rheology of the fluid in the older experiments. It should be investigated what caused these changes that had such a drastic effect.

- In case of the 9% PIB/C14 solution, a change in the viscometric functions in steady simple shear was observed for fluid used in the experiments with the confined cylinder geometry. This is attributed to the degradation of the polymer due to high elongational and shear rates in the flow loop. It should be investigated how this degradation can be prevented.

- At the higher Deborah numbers ($De > 1$) in the flows of the polymer solutions, differences increased between the measured stresses and those computed with the (four mode) viscoelastic models. Parameter adjustments using the measured data might improve this agreement.

- The cause of the failure of the finite element simulations, that occurred for the LDPE melt at higher Deborah numbers ($De > 8$), should be investigated.

- The setup for the complex flow experiments with melts should be extended with a by-pass loop with a drain and a gear pump to ensure that the throughput through

the flow cell is not influenced by variations of the extruder screw rotation. A static mixer should also be used to guarantee a homogeneous temperature distribution in the melt.

- In case of the polymeric model fluids, a flow should be searched with a pronounced influence of the stress field on the velocity field. Such flow will distinguish better between the viscoelastic constitutive models. In this search, not only the geometry, but also the fluid should be varied. A fluid with a larger relaxation time, such as the 9% PIB/C14 solution used tentatively in Chapter 4, enables larger Deborah numbers at the same flow rate. Also, different constituent polymers should be used in these solutions to find out how much variation in rheological behavior is typical among polymer solutions (compare the drastically different behavior in a circular contraction of two Boger fluids as reported by Boger and Binnington [15]).
  Numerical simulations should be used to help design the experiments. Initially, the simple technique of flow visualization with reflecting tracer particles is preferred to the pointwise techniques to have fast, qualitative fieldwise answers. When the level of birefringence is sufficient the fieldwise birefringence technique should be used for the same reason. Subsequently, the pointwise techniques should be used for a detailed, quantitative comparison as demonstrated in this thesis.

- Complementary to planar flows, axisymmetric flows should be studied in the same way. The birefringence measurements can then not be translated in terms of stresses, but the optically measured quantities can easily be computed from the finite element simulations (at perhaps the cost of some loss of information) (Burghardt [18]). Axisymmetric flows have the property of being strongly 'aligning' (Larson [70], p. 196), while planar flows are neutrally aligning like simple shear flows. The sensitivity of constitutive models for such flow varies (Larson [70]), and therefore they seem useful to discriminate between models.

- The results in this thesis show that compared with the velocity field the stress field is more sensitive for the particular combination of model and fitted model parameters. It would be interesting to consider industrial applications in which relevant product properties are influenced by the stress field. An example is the injection moulding of compact discs, where residual stresses can undesirably affect the optical properties of the disc (Wimberger-Friedl [116]).

- Any iterative procedure that uses field quantities of a complex flow to optimize parameters of viscoelastic constitutive equations will be hampered by the time-consuming character of the computations. Though significant progress on this problem can be expected by the evolution of computer science, methods that circumvent the use of fieldwise numerical simulations are intrinsically faster. A powerful method is computing the stress fields by integration of the constitutive equation along streamlines using the spatial derivatives of the measured velocity field. This method does not make the finite element computations superfluous, since both velocity and stress

field are determined by the constitutive equation. It will, however, help to discriminate between constitutive equations and to find the most realistic model. Also, prior to a full computation of the flow, parameters can be fit with data from elongational flow in an efficient way.
This hybrid method requires an experimental method that can measure all velocity components that are of interest (two or three). In case more than one component has to be measured, the laser Doppler method has the disadvantage of requiring refractive index matching of the fluid with the transparent flow cell. The method also measures the velocity in a single point at a moment in time, which is a disadvantage when studying time-dependent flows.
The particle image velocimetry (PIV) technique (Adrian [2]) surmounts these problems: it can measure two or three velocity components simultaneously and also dynamically. This technique seems of primary relevance when developing the hybrid technique as described above.

- Compared with polymer solutions, several experimental problems will complicate the experimental analysis of polymer melt flow. The use of the pointwise birefringence technique can be hampered by the presence of large stress gradients relative to the size of the measuring volume. In case the distance between two order transitions of the retardance δ is smaller than the beam diameter, the results will be useless, since averaging will take place over two (or more) orders. In this common situation, the fieldwise birefringence technique must be preferred, unless the fringe separation is so small they can not be resolved anymore. The pointwise birefringence technique is particularly suitable for (relatively low birefringent) polymer solutions.

- In polymer melts, non-isothermal flow conditions (that are at higher Deborah numbers intrinsically present due to viscous dissipation) will disturb any optical method that is sensitive for variation of the mean refractive index. This is particularly the case when laser beams are used, because these are deflected by gradients in the mean refractive index and the laser will even not reach the detector anymore. The relatively simple techniques of streakline visualization with tracer particles and the fieldwise birefringence method are expected to be less sensitive. But the observation can also be disturbed resulting in a poorly defined image. Other, non-optical techniques may be necessary as for example magnetic resonance imaging (MRI) for velocity measurements (e.g. Rofe et al. [97]). The applicability of this latter method to complex flow studies should be investigated. For the stress measurements, no alternative technique is known to the author.

- The analysis should be extended towards the start-up of steady complex flows. These flows contain more information on the fluid rheology and will be more rigorous tests for the constitutive equations.

Appendix A

Electromagnetic description of light

A.1 Introduction

The theories of the optical techniques (LDA and FIB) used in this thesis are formulated within the theoretical framework of electromagnetism. Below, a short recapitulation of the basic equations is given. It will be shown that an electromagnetic wave is the solution of the Maxwell equation. The most simple solution is the so called 'transverse electric' plane wave. Such waves are used when explaining the principles of LDA and FIB measurement techniques (Section 2). Furthermore, the molecular theory that explains the linear stress optical rule uses the electromagnetic theory also (Section 2.3.2).

A.2 Maxwell equations

Light can be regarded as an electromagnetic wave. Electromagnetic phenomena are governed by the Maxwell equations, which for sources in vacuum are ([59]):

$$\vec{\nabla} \cdot \vec{D} = \rho \tag{A.1}$$

$$\vec{\nabla} \cdot \vec{B} = 0 \tag{A.2}$$

$$\vec{\nabla} \times \vec{E} + \frac{\partial \vec{B}}{\partial t} = 0 \tag{A.3}$$

$$\vec{\nabla} \times \vec{H} = \vec{J} + \frac{\partial \vec{D}}{\partial t} \tag{A.4}$$

with $\vec{D}$ the dielectric displacement, $\vec{E}$ the electric field, $\vec{H}$ the magnetic field, $\vec{B}$ the magnetic induction, $\vec{J}$ the current density, ρ the charge density. In this thesis the SI units are adopted, but in literature on electromagnetism often the Gauss units are used ([59]).

Additional to the Maxwell equations , three constitutive equations are needed for $\vec{J}$, $\vec{D}$ and $\vec{H}$ respectively. With some assumptions[1] linear behavior is found, expressed by the

[1] neglecting multipole contributions of the charge distribution and excluding ferroelectric, ferromagnetic and optical active media and assuming weak enough fields

relations:

$$\vec{J} = \boldsymbol{\sigma}\vec{E} \tag{A.5}$$

$$\vec{D} = \boldsymbol{\varepsilon}\vec{E} \tag{A.6}$$

$$\vec{H} = \boldsymbol{\mu}^{-1}\vec{B}. \tag{A.7}$$

where $\boldsymbol{\sigma}$ is the conductivity tensor, $\boldsymbol{\varepsilon}$ the dielectric tensor and $\boldsymbol{\mu}^{-1}$ the inverse magnetic permeability tensor. The latter two equations are also written as $\vec{D} = \varepsilon_0\vec{E} + \vec{P}$ and $\vec{H} = {\mu_0}^{-1}\vec{B} - \vec{M}$ respectively, with ε_0 the dielectric constant in vacuum, μ_0 the magnetic permeability in vacuum, $\vec{P}$ and $\vec{M}$ the polarization and magnitization in the dielectric respectively. For isotropic media the tensors $\boldsymbol{\sigma}$, $\boldsymbol{\varepsilon}$ and $\boldsymbol{\mu}$ can be replaced by σ, ε and μ: the conductivity, the dielectric constant and the magnetic permeability respectively. In Section 2.3.2 the polarization $\vec{P}$ is expressed explicitly in $\vec{E}$.

A.3 The electromagnetic wave equation

Consider an isotropic dielectric for which constitutive equations A.5 - A.7 apply with scalar σ, ε and μ. The Maxwell equations can then be reduced to a set of two equations with two unknown variables $\vec{E}$ and $\vec{B}$. Interaction of electromagnetic waves with matter is dominated by the interaction of the electric field vector with oscillating electrons in the dielectric. Therefore, the contribution of the magnetic field is usually neglected:

$$\vec{\nabla}^2\vec{E} - \mu\varepsilon\frac{\partial^2\vec{E}}{\partial t^2} - \mu\sigma\frac{\partial\vec{E}}{\partial t} = \vec{\nabla}(\frac{\rho}{\varepsilon}) \tag{A.8}$$

For non-conducting media ($\sigma = 0$) free of charge ($\rho = 0$) Equation A.8 is a wave equation. The simplest solution of Equation A.8 is a transverse electric (TE) monochromatic plane wave, i.e. a field that is propagating in a single direction parallel with $\vec{k} = k\vec{e_k}$, the wave vector (planes of constant phase are perpendicular to this direction), and that has a single frequency (ω) and is linear polarized. Such a plane wave is represented by

$$\vec{E} = \vec{E_0}e^{i(k\vec{e_k}\cdot\vec{x}-\omega t)} \tag{A.9}$$

where k is the wave number, defined by $k = \frac{\omega}{v}$, with v the phase velocity of the wave. $\vec{E_0}$ is constant in space and time. The velocity of light in vacuum is $c = \frac{1}{\sqrt{\varepsilon_0\mu}}$, and the refractive index $n = \frac{c}{v}$.

Appendix B

Müller matrices

Stokes parameters The polarization state of light can be represented with the Stokes parameters (see for a comprehensive treatment Azzam and Bashara [5]). The four Stokes parameters, denoted with S_0,S_1,S_2,and S_3 are observable quantities with the dimension of intensity, defined by

$$S_0 = \langle E_1^2(t)\rangle + \langle E_2^2(t)\rangle \quad \text{(B.1)}$$

$$S_1 = \langle E_1^2(t)\rangle - \langle E_2^2(t)\rangle \quad \text{(B.2)}$$

$$S_2 = 2\langle E_1(t)E_2(t)\cos(\delta_1(t) - \delta_2(t))\rangle \quad \text{(B.3)}$$

$$S_3 = 2\langle E_1(t)E_2(t)\sin(\delta_1(t) - \delta_2(t))\rangle. \quad \text{(B.4)}$$

where $E_1(t)$, $E_2(t)$ represent the time-dependent amplitudes of two orthogonal components of the light wave. Here $\langle a\rangle$ signifies the time average of a with the integration time long enough to make the average independent of the integration time itself, allowing the description of quasi-monochromatic waves. Together, the Stokes parameters constitute the Stokes vector (actually a column) : $S = [S_0, S_1, S_2, S_3]^T$. The Stokes parametes can be measured from simple intensity experiments (see Azzam and Bashara [5]). The interpretation of S_0 is trivial: it is equivalent with the total intensity of the light.

Propagation of a wave, represented with a Stokes vector S_i, through an optical device is described by

$$S_o = MS_i \quad \text{(B.5)}$$

where M is the 4×4 Mueller matrix.

Three important Müeller matrices are (with $s_{2\theta}, c_{2\theta}$ for $sin(2\theta), cos(2\theta)$, and δ for the retardation of a birefringent material ($\delta = \frac{2\pi d}{\lambda}\Delta n$, d: thickness of sample , λ: wave length , Δn: birefringence)), see Fuller [37]:

Ideal polarizer oriented at θ:

$$\begin{bmatrix} 1 & c_{2\theta} & s_{2\theta} & 0 \\ c_{2\theta} & c_{2\theta}^2 & s_{2\theta}c_{2\theta} & 0 \\ s_{2\theta} & s_{2\theta}c_{2\theta} & s_{2\theta}^2 & 0 \\ 0 & 0 & 0 & 0 \end{bmatrix} \quad \text{(B.6)}$$

Birefringent element oriented at θ:

$$\begin{bmatrix} 1 & 0 & 0 & 0 \\ 0 & (c_{2\theta}^2 + s_{2\theta}^2 c_\delta) & s_{2\theta}c_{2\theta}(1-c_\delta) & -s_{2\theta}s_\delta \\ 0 & s_{2\theta}c_{2\theta}(1-c_\delta) & (s_{2\theta}^2 + c_{2\theta}^2 c_\delta) & -c_{2\theta}s_\delta \\ 0 & s_{2\theta}s_\delta & -c_{2\theta}s_\delta & c_\delta \end{bmatrix} \tag{B.7}$$

Left circular polarizer:

$$\begin{bmatrix} 1 & 0 & 0 & 1 \\ 0 & 0 & 0 & 0 \\ 0 & 0 & 0 & 0 \\ 1 & 0 & 0 & 1 \end{bmatrix} \tag{B.8}$$

Right circular polarizer:

$$\begin{bmatrix} 1 & 0 & 0 & -1 \\ 0 & 0 & 0 & 0 \\ 0 & 0 & 0 & 0 \\ -1 & 0 & 0 & 1 \end{bmatrix} \tag{B.9}$$

Quarter wave plates and halfwave plates are birefringent plates with a known phase retardation: $\pi/2$, and π respectively. Circular polarizers have no principal axes in the plane perpendicular to the direction of the wave propagation.

Appendix C

Laser beam dimensions

Laser beams are considered to be Gaussian. Such beams have a Gaussian intensity distribution as function of the radius of the beam and have contours with a concave shape along the axial beam direction. In a single point the beam radius is minimal, this radius is called the beam waist. A beam with waist w has a radius at an axial distance z from the position of the waist that is described by (Siegman [103]):

$$w_1 = w\sqrt{1+\phi^2} \tag{C.1}$$

with ϕ according

$$\phi = \frac{\lambda z}{\pi w^2} \tag{C.2}$$

where λ is the wavelength of the light. The transformation of Gaussian beams by lenses is expressed by the relation between the beam waist w_0 before and the waist w after a lens with focal length f:

$$w = \frac{\lambda f}{\pi w_0}. \tag{C.3}$$

To achieve a high spatial resolution during the pointwise FIB experiments the aim is to produce a laser beam with a minimal radius along the whole optical path in the flow cell. Equation C.1 implies that the beam is curved along the axial direction. The effective beam radius is determined by the beam radius at the entrance and exit planes of the flow cell. Focusing a laser with waist w_0 with a lens will result in a smaller waist w_1 after the lens. The waist w_1 decreases with decreasing focal lengths (Equation C.3) but the curvature of the beam in the axial direction increases too (Equation C.1). The optimal beam waist such that the beam radius is minimal at a distance z is found by differentiating w_1 in Equation C.1 with respect to the beam waist w. The result is

$$w_1 = \sqrt{2}w \tag{C.4}$$

$$w = \sqrt{\frac{\lambda z}{\pi}}. \tag{C.5}$$

$f[mm]$	$w\,[mm]$	$w_1\,[mm]$
200	0.021	0.32
300	0.032	0.20
400	0.043	0.16
600	0.064	0.12
750	0.083	0.12
1000	0.11	0.14

Table C.1: *Radius of laser beam ($\lambda = 672.4\,nm, w_0 = 2\,mm$) in waist ($w$) and at an axial distance l_c ($= 32\,mm$) from the position of the waist (w_1) as function of focal length f of the collimating lens.*

These equations define the Raleigh range of a laser beam: in this situation the radius of a beam for a given collimated length l_c is minimal; according to Equation C.5 it is maximally $\sqrt{2}w$ with $w = \sqrt{\lambda l_c/2\pi}$. The focal length f of the lens that collimates the beam with initial waist w_0 such that the collimated length is the Raleigh range equals (using Equation C.3) $f = ww_0\frac{\pi}{\lambda}$.

In the case of the FIB measurements in the flow cell for polymer solutions as described in Chapter 4, the waist of the Raleigh range is $0.083\,mm$ and the beam radius at the edges of the collimated length ($= 64\,mm$) is $0.117\,mm$. This Raleigh range is obtained with the diode laser beam with an initial waist $w_0 = 2\,mm$, if a lens is used with $f = 750\,mm$. Table C summarizes the beam radia at the edge of the collimated length for different focal lengths. All the above equations apply to beams in vacuum. In dense media with a refractive index n the actual beam radia are found after substituting $\frac{\lambda}{n}$ for λ.

Diode lasers do not produce beams that are perfectly Gaussian. In general, some optics is necessary to correct for several errors; for a description of these errors and the correctional optics it is referred to [85].

Appendix D

Measurement of stress optical coefficient in Couette flow

Comparing mechanical and optical data of the shear stress in a simple shear flow gives the most rigorous and reliable test of the linearity of the stress optical rule that can presently be performed. A Couette-cell for installation on the Rheometrics-RFS-II was developed in our lab: in this system the optical and mechanical measurements can be performed simultaneously. The optical measurement has been performed with ROA (Section 2.3.4).

The experimental set-up is displayed in Figure D.1. The numbers refer to: (1) part of Rheometric-RFS-2, (2) torque transducer, (4) bob of Couette cel, (5) cup of Couette cel, (6) window of SF-57 glass (Schott, [99]), (7) polarization modulation generator of ROA (laser, polarizer, rotating halfwave plate, lens), (8) circular polarizer followed by a mirror to deflect the beam over 90 degrees, (9) detector (in the actual measurements, the detector was adapted so that the mirror was not necessary anymore). The details of the measurement procedure are described by Schoonen [98].

In case of the 5% PIB/C14 solution used in Chapter 4, the result of the validation of the linearity of the stress optical rule is shown in Figure 4.6. The stress optical coefficient C is $1.86 \cdot 10^{-9}\, Pa^{-1}$, which is in excellent agreement with the value of Quinzani [93] who found $C = 1.87 \cdot 10^{-9}\, Pa^{-1}$.

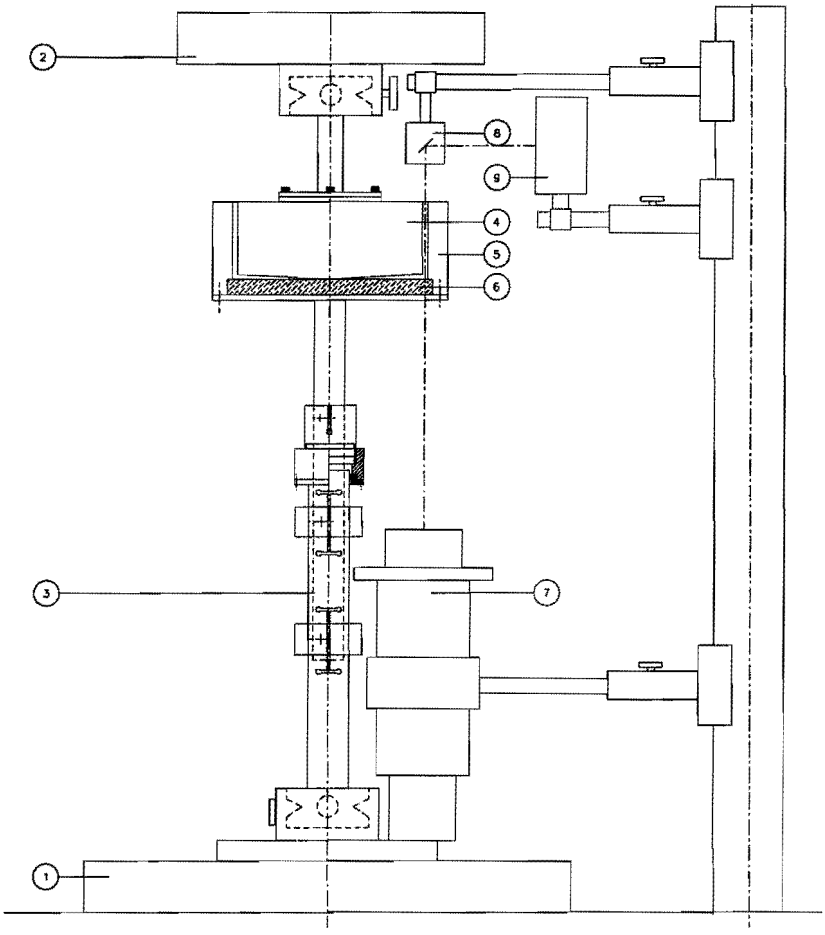

Figure D.1: *Couette cell installed on the Rheometrics-RFS-II to measure simultaneously mechanically (by measuring the mechanical torque on the inner bob) and optically (with the ROA birefringence system) the shear stress.Numbers are explained in the text.*

Appendix E

Estimation of statistical error in stresses measured with ROA

In the birefringence measurements with ROA (Section 2.3.4), two parameters are measured: R_1 and R_2. To obtain the stresses, two steps are made: first, the angles *chi* and δ are calculated from R_1 and R_2, and subsequently, from these angles the stresses are obtained. The equations are:

$$\chi = \frac{1}{2}\arctan\frac{-R_2}{R_1}, \tag{E.1}$$

$$\delta = sign(R_1)\sqrt{R_1^2+R_2^2}, \tag{E.2}$$

$$\tau = \frac{f}{2C}\delta\sin 2\chi, \tag{E.3}$$

$$N_1 = \frac{f}{C}\delta\cos 2\chi, \tag{E.4}$$

with C the stress optical coefficient, $f=\frac{\lambda}{2\pi d}$, with λ the wavelength of the light and d the length of the light path through the birefringent sample.

Denote the standard devitation of R_1 with $\sigma(R_1)$ and of R_2 with $\sigma(R_2)$. The standard deviation in χ and δ then follow from

$$\frac{\partial\chi}{\partial R_1} = -\frac{1}{2}\frac{R_2}{R_1^2+R_2^2}, \tag{E.5}$$

$$\frac{\partial\chi}{\partial R_2} = \frac{1}{2}\frac{R_1}{R_1^2+R_2^2}, \tag{E.6}$$

$$\sigma(\chi) = \sqrt{(\frac{\partial\chi}{\partial R_1})^2\sigma(R_1)^2+(\frac{\partial\chi}{\partial R_2})^2\sigma(R_2)^2}, \tag{E.7}$$

and

$$\frac{\partial\delta}{\partial R_1} = \frac{R_1}{\sqrt{(1-(R_1^2+R_2^2))(R_1^2+R_2^2)}}, \tag{E.8}$$

$$\frac{\partial \delta}{\partial R_2} = \frac{R_2}{\sqrt{(1-(R_1^2+R_2^2))(R_1^2+R_2^2)}}, \tag{E.9}$$

$$\sigma(\delta) = \sqrt{(\frac{\partial \delta}{\partial R_1})^2 \sigma(R_1)^2 + (\frac{\partial \delta}{\partial R_2})^2 \sigma(R_2)^2}. \tag{E.10}$$

Subsequently, in the same way the standard deviations of the shear stress τ and first normal stress difference N_1 are found with:

$$\frac{\partial \tau}{\partial \delta} = \frac{f}{2} \sin 2\chi, \tag{E.11}$$

$$\frac{\partial \tau}{\partial \chi} = f\delta \cos 2\chi, \tag{E.12}$$

$$\frac{\partial N_1}{\partial \delta} = f \cos 2\chi, \tag{E.13}$$

$$\frac{\partial N_1}{\partial \chi} = -2f\delta \sin 2\chi. \tag{E.14}$$

In all ROA experiments in this thesis (Chapter 4), the data were averaged from 100 measurements. As an example, the error bounds have been calculated for the data along the line $x/R = 1.5$ (in case of the 5% PIB/C14 solution with $De_1 = 2.31$, in the symmetrically confined cylinder geometry). In Figure E.1, the data points of the three types of data are plotted, with the error bounds calculated according $3/\sqrt{N}\sigma$, with N the number of samples and σ the standard deviation. The relative error in the stresses is typically $< \pm 2\%$. Larger errors occur when R_1 is near zero, or both R_1 and R_2 are near zero (i.e. when $\delta = k\pi, k = 0, \pm 1, ...$), since then the angle χ is indefinite.

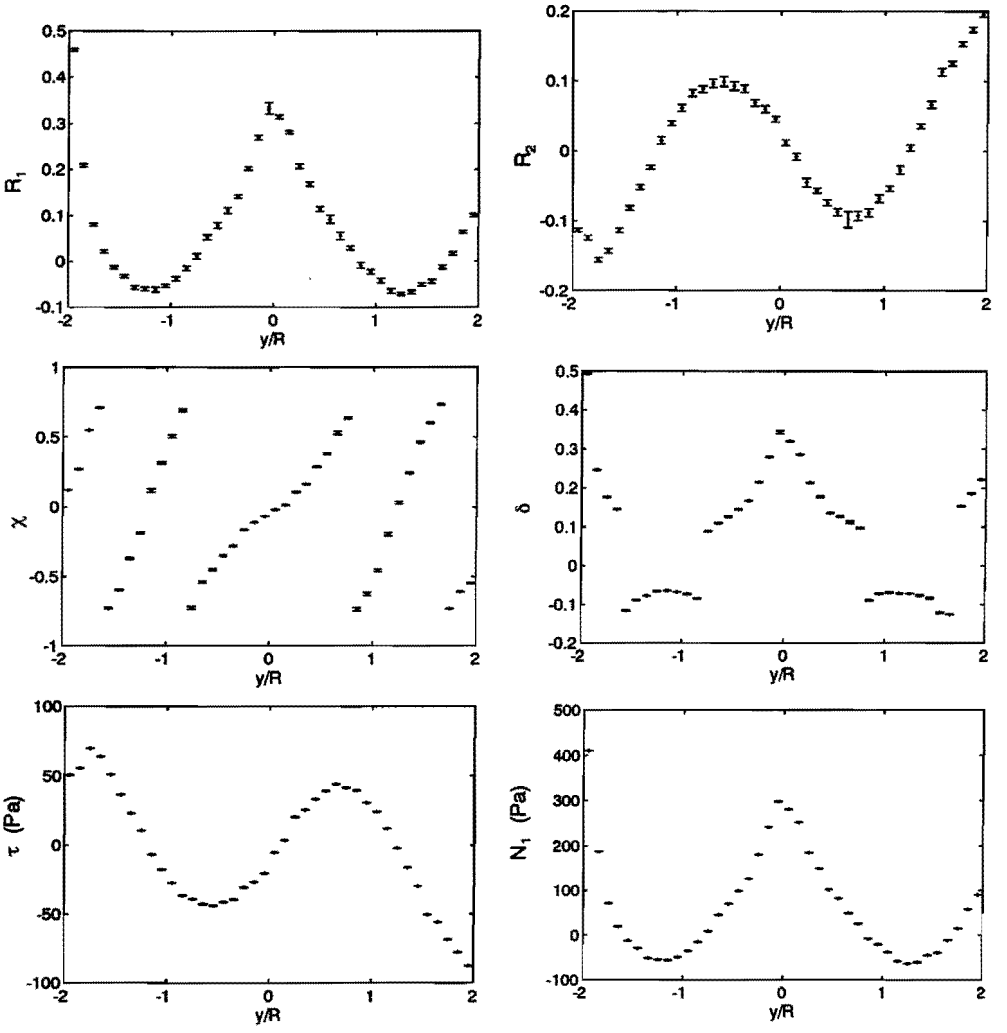

Figure E.1: *Example of data with error bounds of the birefringence measurements (with ROA, see text): (top) R_1 and R_2, (middle) the angles χ, δ and (bottom) the shear stress τ and first normal stress difference N_1.*

References

[1] V. Abetz and G.G. Fuller. Two-color rotary modulated flow birefringence. *Rheologica Acta*, 29:11–15, 1990.

[2] R.J. Adrian. Particle imaging techniques for experimental fluid mechanics. *Annual Review of Fluid Mechanics*, 23:261–304, 1991.

[3] S.T.E. Aldhouse, M.R. Mackley, and I.P.T. Moore. Experimental and linear viscoelastic stress distribution measurements of high density polyethylene flowing into and within a slit. *Journal of Non-Newtonian Fluid Mechanics*, 21:359–376, 1986.

[4] R.C. Armstrong, R.A. Brown, L.M. Quinzani, G.H. McKinley, and J.A. Byars. Measurement of velocity and stress fields in complex polymer flows. In P. Moldenaers and R. Keunings, editors, *Proc. XI Int. Cong. Rheology, Theoretical and applied rheology, Brussels*, pages 16–23, Amsterdam, 1992. Elsevier.

[5] R.M.A. Azzam and N.M. Bashara. *Ellipsometry and polarized light.* North-Holland, Amsterdam, 1987.

[6] F.P.T. Baaijens. Numerical analysis of start-up planar and axisymmetric contraction flows using multi-mode differential constitutive models. *Journal of Non-Newtonian Fluid Mechanics*, 48:147–180, 1993.

[7] F.P.T. Baaijens. Applied computational mechanics 2. Course book, Eindhoven University of Technology, P.O. Box 513, 5600 MB Eindhoven, The Netherlands, 1994.

[8] F.P.T. Baaijens. Non-isothermal viscoelastic flow past a cylinder. In F.J. Dijksman and G. Kuiken, editors, *Proceedings IUTAM symposium on numerical simulation of non-isothermal flows of viscoelastic liquids, The Netherlands*, 1994. to be published.

[9] F.P.T. Baaijens, J.P.W. Baaijens, G.W.M. Peters, and H.E.H.Meijer. A numerical and experimental investigation of viscoelastic flow around a cylinder. *Journal of Rheology*, 38:351–376, 1994.

[10] A. Baloch, D. Ding, P. Townsend, and M.F. Webster. Some transient studies of non-Newtonian non-isothermal flows in two and three dimensions. In P. Moldenaers and R. Keunings, editors, *Proc. XI Int. Cong. Rheology, Theoretical and applied rheology, Brussels*, pages 250–252, Amsterdam, 1992. Elsevier.

[11] L.E. Becker, G.H. McKinley, H.K. Rasmussen, and O. Hassager. The unsteady motion of a sphere in a viscoelastic fluid. *Journal of Rheology*, 38:377–403, 1994.

[12] R.J. Binnington and D.V. Boger. Constant viscosity elastic liquids. *Journal of Rheology*, 29:887–904, 1985.

[13] R.B. Bird, C.F. Curtiss, R.C. Armstrong, and O. Hassager. *Dynamics of polymeric liquids.* John Wiley and Sons, New York, 1987.

[14] D.V. Boger. Viscoelastic flow through abrupt contractions. *Annual Review of Fluid Mechanics*, 19:157–182, 1987.

[15] D.V. Boger and R.J. Binnington. Experimental removal of the re-entrant corner singularity in tubular entry flows. *Journal of Rheology*, 38:333–349, 1994.

[16] D.V. Boger, M.J. Crochet, and R.A. Keiller. On viscoelastic flows through abrupt contractions. *Journal of Non-Newtonian Fluid Mechanics*, 44:267–270, 1992.

[17] R.A. Brown and G.H. McKinley. Report on the VIIIth int. workshop on numerical methods in viscoelastic flows. *Journal of Non-Newtonian Fluid Mechanics*, 52:407–413, 1994.

[18] W. Burghardt, 1994. private communication (North Western University, Evanston, Illinois).

[19] W. Burghardt and G.G. Fuller. End effects in flow birefringence measurements. *Journal of Rheology*, 33:770–778, 1989.

[20] A.A. van Steenhoven C. Cuvelier, A. Segal. *Finite element methods and Navier-Stokes equations.* D. Reidel Publishing Co., Dordrecht, 1986.

[21] C.A. Cathey and G.G. Fuller. The optical and mechanical response of flexible polymer solutions to extensional flow. *Journal of Non-Newtonian Fluid Mechanics*, 34:63–88, 1990.

[22] R.P. Chhabra, P.H.T. Uhlherr, and D. Boger. The influence of fluid elasticity on the drag coefficient for creeping flow around a sphere. *Journal of Non-Newtonian Fluid Mechanics*, 6:187–199, 1980.

[23] M.D. Chilcott and J.M. Rallison. Creeping flow of dilute solutions past cylinders and spheres. *Journal of non-Newtonian fluid mechanics*, 29:381–432, 1988.

[24] C. Chmielewski and K. Jayaraman. Elastic instability in crossflow of polymer solutions through periodic arrays of cylinders. *Journal of non-Newtonian fluid mechanics*, 48:285–301, 1993.

[25] T. Cochrane, K. Walters, and M.F. Webster. On Newtonian and non-Newtonian flow in complex geometries. *Phil. Trans. R. Soc. Lond. A*, 301:163–181, 1981.

[26] M. Copic. Streaming birefringence of polymer solutions: anisotropy of internal fields. *Journal of Chemical Physics*, 26:1382–1390, 1957.

[27] D.L. Davidson, W.W. Graessley, and W.R. Schowalter. Velocity and stress fields of polymeric liquids flowing in a periodically constricted channel: Experimental methods and straight channel validations. *Journal of Non-Newtonian Fluid Mechanics*, 49:317–344, 1993.

[28] D.L. Davidson, W.W. Graessley, and W.R. Schowalter. Velocity and stress fields of polymeric liquids flowing in a periodically constricted channel: Observations of non-Newtonian behavior. *Journal of Non-Newtonian Fluid Mechanics*, 49:317–344, 1993.

[29] F. Debae, V. Legat, and M.J. Crochet. Practical evaluation of four mixed finite element methods for viscoelastic flows. *Journal of Rheology*, 38:421–443, 1994.

[30] S.A. Dhahir and K. Walters. On non-Newtonian flow past a cylinder in a confined flow. *Journal of Rheology*, 33(6):781–804, 1989.

[31] M. Doi and S.F. Edwards. *The theory of polymer dynamics.* Oxford University Press, Oxford, 1986.

[32] L.F.A. Douven. *Towards the computation of properties of injection moulded products: flow- and thermally induced stresses in amorphous thermoplastics.* PhD thesis, Eindhoven University of Technology, The Netherlands, 1991.

[33] L.E. Drain. *The Laser Doppler Technique.* John Wiley and Sons, Chicester, 1980.

[34] J. Ferguson and N.E. Hudson. The shear and extensional flow properties of S1. *Journal of Non-Newtonian Fluid Mechanics*, 52:121–135, 1994.

[35] J.D. Ferry. *Viscoelastic properties of polymers.* John Wiley and Sons, New York, 3 edition, 1980.

[36] G.G. Fuller. Optical rheometry. *Annual Review of Fluid Mechanics*, 22:387–417, 1990.

[37] G.G. Fuller. *Measurement of dynamics and structure in complex liquids: theory and practice of optical rheometry.* Oxford University Press, Oxford, 1995.

[38] G.G. Fuller and K.J. Mikkelsen. Note: Optical rheometry using a rotary polarization modulator. *Journal of Rheology*, 33:761–769, 1989.

[39] K. Funatsu and T. Kajiwara. *Stress measurements of viscoelastic fluids by flow birefringence technique and slip phenomena of polymer melts*, volume 7 of *Encyclopedia of fluid mechanics, Rheology and non-Newtonian flow*, chapter 13. Gulf Publishing Company, Houston, 1988.

[40] S.R. Galante. *An investigation of planar entry flow using a high resolution flow birefringence method.* PhD thesis, Garnegie Mellon University, Penssylvania (USA), 1991.

[41] S.R. Galante and P.L. Fratini. Spatially resolved birefringence studies of planar entry flow. *Journal of Non-Newtonian Fluid Mechanics*, 47:289–337, 1993.

[42] P.G. De Gennes. *Scaling concepts in polymer physics.* Cornell University Press, Ithaca, New York, 1979.

[43] G. Georgiou, S. Momani, M.J. Crochet, and K. Walters. Newtonian and non-Newtonian flow in a channel obstructed by an antisymmetric array of cylinders. *Journal of Non-Newtonian Fluid Mechanics*, 40:231–260, 1991.

[44] Giesekus. A simple consitutive equation for polymer fluids based on the concept of deformation-dependent tensorial mobility. *Journal of Non-Newtonian Fluid Mechanics*, 11:69–109, 1982.

[45] R.J. Goldstein. *Fluid mechanics measurement.* Hemisphere Publishing Corporation, New York, 1983.

[46] C.D. Han and L.H. Drexler. Studies of converging flows of viscoelastic polymeric melts, i. stress-birefringent measurements in the entrance region of a sharp-edged slit die. *Journal of Applied Polymer Science*, 17:2329–2354, 1973.

[47] C.D. Han and L.H. Drexler. Studies of converging flows of viscoelastic polymeric melts, i. stress and velocity distributions in the entrance region of a sharp-edged slit die. *Journal of Applied Polymer Science*, 17:2369–2393, 1973.

[48] C.D. Han and L.H. Drexler. Studies of converging flows of viscoelastic polymeric melts, i. velocity measurements in the entrance region of a sharp-edged slit die. *Journal of Applied Polymer Science*, 17:2355–2368, 1973.

[49] O. Hassager. Working group on numerical techniques. *Journal of Non-Newtonian Fluid Mechanics*, 29:2–5, 1988.

[50] E. Hecht and A. Zajac. *Optics.* Addison-Wesley, Reading, Massachusetts, 1974.

[51] M.A.N. Hendriks. *Identification of the mechanical behavior of solid materials.* PhD thesis, Eindhoven University of Technology, The Netherlands, 1991.

[52] J.O. Hinze. *Turbulence.* McGraw-Hill, New York, 1975.

[53] K. Hongladarom, W.R. Burghardt, S.G. Baek, S. Cementwala, and J.J. Magda. Molecular alignment of polymer liquid crystals in shear flows 1. Spectrographic birefringence technique, steady-state orientation, and normal stress behavior in poly(benzylglutamate) solutions. *Macromolecules*, 26:772–784, 1993.

[54] N.E. Hudson and J. Ferguson. The anomalous shear flow properties of S1. *Journal of Non-Newtonian Fluid Mechanics*, 52:105–119, 1994.

[55] M.A. Hulsen. *Analysis and numerical simulation of the flow of viscoelastic fluids.* PhD thesis, Delft University of Technology, The Netherlands, 1988.

[56] M.A. Hulsen. A numerical method for solving steady 2d and axisymmetrical viscoelastic flow problems with an application to inertia effects in contraction flows. Research note MEMT 11, Delft University of Technology, The Netherlands, 1990.

[57] M.A. Hulsen and J. van der Zanden. Numerical simulation of contraction flows using a multi-mode Giesekus model. *Journal of Non-Newtonian Fluid Mechanics*, 38:183–221, 1991.

[58] A.I. Isayev and R.K. Upadhyay. Two-dimensional visco-elastic flows: experimentation and modeling. *Journal of Non-Newtonian Fluid Mechanics*, 19:135–160, 1985.

[59] J.D. Jackson. *Classical Electrodynamics.* John Wiley and Sons, New York, 1975.

[60] H. Janeschitz-Kriegl. *Polymer melt rheology and flow birefringence*, volume 6 of *Polymers/Properties and Applications.* Springer-Verlag, 1983.

[61] D.M. Jones and K. Walters. The behaviour of polymer solutions in extension-dominated flows, with applications to enhanced oil recovery. *Rheologica Acta*, 28:482–498, 1989.

[62] T. Kajiwara, S. Ninomiya, Y. Kuwano, and K. Funatsu. Numerical simulation of converging flow of polymer melts through a tapered slit die. *Journal of Non-Newtonian Fluid Mechanics*, 48:111–124, 1993.

[63] M. Kerker. *The scattering of light.* Academic, New York, 1969.

[64] D.G. Kiriakidis, H.J. Park, and E. Mitsoulis. A study of stress distribution in contraction flows of an LLDPE melt. *Journal of Non-Newtonian Fluid Mechanics*, 47:339–356, 1993.

[65] P.G.M. Kruijt. Experimental and numerical analysis of polymer melt flow past a constrained cylinder. Master's thesis WFW 94.133, Eindhoven University of Technology, The Netherlands, 1994.

[66] P.G.M. Kruijt. The Rheo Optical Analyzer for birefringence measurements, Enhancement with a 2D traverse table using LABView. Technical Report WFW 94.011, Eindhoven University of Technology, The Netherlands, 1994.

[67] W. Kuhn and F. Grun. Beziehungen zwischen elastischen Konstanten und Dehnungsdoppelbrechung hochelastischer Stoffe. *Kolloid Zeitung*, 101(3):248–271, 1942.

[68] A. Kuske and G. Robertson. *Photoelastic Stress Analysis.* John Wiley, London, 1977.

[69] R.K. Lambert, G.J. Rofe, L. de Vargas, and P.T. Callaghan. MRI measurements of velocity profiles for capillary flows of aqueous solutions of xanthan. In *Progress and Trends in Rheology IV, Proceedings 4th European Rheology Conference, Sevilla, september 4-9 1994*, pages 492–493. Steinkopff Verlag, Darmstadt, 1994.

[70] R.G. Larson. *Constitutive equations for polymer melts and solutions.* Buttersworth, Boston, 1988.

[71] H.M. Laun. In Proceedings of the 9th International Congress on Rheology,Acapulco, Mexico, 1984.

[72] Y.J. Liu, J. Nelson, J. Feng, and D.D. Joseph. Anomalous rolling of spheres down an inclined plane. *Journal of Non-Newtonian Fluid Mechanics*, 0:000–000, 1994. To be published.

[73] R.C. Armstrong L.M. Quinzani, G.H. McKinley and R.A. Brown. Modelling the rheology of polyisobutylene solutions. *Journal of Rheology*, 34:705–749, 1990.

[74] W.J. Lunsmann, L. Genieser, R.C. Armstrong, and R.A. Brown. Finite element analysis of steady viscoelastic flow around a sphere in a tube: calculations with constant viscosity models. *Journal of Non-Newtonian Fluid Mechanics*, 48:63–99, 1994.

[75] M.E. Mackay and D.V. Boger. Flow visualisation in rheometry. In A.A. Collyer and D.W. Clegg, editors, *Rheological Measurement*, chapter 14. Elsevier, Amsterdam, 1988.

[76] M.R. Mackley and I.P.T. Moore. Experimental velocity distribution measurements of high density polyethylene flowing into and within a slit. *Journal of Non-Newtonian Fluid Mechanics*, 21:337–358, 1986.

[77] H. Maders, B. Vergnes, Y. Demay, and F. Agassant J. Steady flow of a White-Metzner fluid in a 2D abrupt contraction: computation and experiments. *Journal of Non-Newtonian Fluid Mechanics*, 45:63–80, 1992.

[78] O. Manero and B. Mena. On the slow flow of viscoelastic liquids past a circular cylinder. *Journal of Non-Newtonian Fluid Mechanics*, 9:379–387, 1981.

[79] A.J. McHugh, M.E. Mackay, and B. Khomami. Measurement of birefringence by the method of isoclinics. *Journal of Rheology*, 31:619–634, 1987.

[80] G.H. McKinley. *Dynamics of polymer solutions.* PhD thesis, Massachusetts Institute of Technology, Cambridge (USA), 1991.

[81] G.H. McKinley, 1993. private communication (Divison of Applied Sciences, Harvard University, Cambridge (USA)).

[82] G.H. McKinley, R.C. Armstrong, and R.A. Brown. A viscoelastic flow instability in the wake of a confined circular cylinder. In P. Moldenaers and R. Keunings, editors, *Proc. XI Int. Cong. Rheology, Theoretical and applied rheology*, pages 198–200, Brsussels, 1992. Elsevier.

[83] G.H. McKinley, W.P. Raiford, R.A. Brown, and R.C. Armstrong. Non-linear dynamics of viscoelastic flow in axisymmetric abrupt contractions. *Journal of Fluid Mechanics*, 223:411–456, 1991.

[84] D.W. Mead. *Modelling polydisperse polymer melts with single integral constitutive equations.* PhD thesis, Cambridge University, 1988.

[85] Melles Griot Inc. *Optics Guide 5*, 1993.

[86] B. Mena and B. Caswell. Slow flow of an elastic-viscous fluid past an immersed body. *The Chemical Engineering Journal*, 8:125–134, 1974.

[87] B. Mena, O. Manero, and L.G. Leal. The influence of rheological properties on the slow flow past spheres. *Journal of Non-Newtonian Fluid Mechanics*, 26:247–275, 1987.

[88] T. Olsson. A solver for time dependent viscoelastic fluid flows. *Journal of Non-Newtonian Fluid Mechanics*, 51:309–340, 1994.

[89] C.W.J. Oomens, M.R. van Ratingen, J.D. Janssen, J.J. Kok, and M.A.N. Hendriks. A numerical-experimental method for a mechanical characterization of biological materials. *Journal of Biomechanics*, 26:617–621, 1994.

[90] N. Phan-Thien and R.I. Tanner. A new constitutive equation derived from network theory. *Journal of Non-Newtonian Fluid Mechanics*, 2:353–365, 1977.

[91] W. Philippoff. Streaming birefringence of polymer solutions. *Journal of polymer science: part C*, 5:1–9, 1963.

[92] G. Pilate and M.J. Crochet. Plane flow of a second-order fluid past submerged boundaries. *Journal of Non-Newtonian Fluid Mechanics*, 2:323–341, 1977.

[93] L.M. Quinzani. *Birefringence Studies of Entry Flows of Concentrated Polymer Solutions.* PhD thesis, Massachusetts Institute of Technology, Cambridge (USA), 1991.

[94] L.M. Quinzani, R.C. Armstrong, and R.A. Brown. Birefringence and laser-Doppler velocimetry (LDV) studies of viscoelastic flow through a planar contraction. *Journal of Non-Newtonian Fluid Mechanics*, 52:1–36, 1994.

[95] W.P. Raiford, L.M. Quinzani, P.J. Coates, R.C. Armstrong, and R.A. Brown. LDV measurements of viscoelastic flow transitions in abrupt axisymmetric contractions: Interaction of inertia and elasticity. *Journal of Non-Newtonian Fluid Mechanics*, 32:39–68, 1989.

[96] D. Rajagopalan, J.A. Bryars, and R.C. Armstrong. Comparison of numerical simulations and birefringence measurements in viscoelastic flow between eccentric rotating cylinders. *Journal of Rheology*, 36(7):1349–1375, 1992.

[97] C.J. Rofe, R.K. Lambert, and P.T. Callaghan. NMR imaging of flow for a shear-thinning polymer in cylindrical Couette flow. *Journal of Rheology*, 38(4):875–887, 1994.

[98] J. Schoonen. Eindhoven University of Technology, The Netherlands, 1994. private communication.

[99] Schott Glass Inc. *Schott optical Glass.*

[100] F.A. Schraub, S.J. Kline, J. Henry, P.W. Runstadler jr., and A. Littel. Use of hydrogen bubbles for quantitative determination of time-dependent velocity fields in low-speed water flows. *ASME Journal of Basic Engineering*, 87:429–444, 1965.

[101] A. Segal. *Manual SEPRAN package.* Ingenieursburo SEPRA, Leidschendam, The Netherlands, 1992.

[102] S. Selen. Eindhoven University of Technology, The Netherlands, 1994. private communication.

[103] A. Siegman. *Lasers.* Oxford University Press, Oxford, 1986.

[104] D. Sigli and M. Coutanceau. Effect of finite boundaries on the slow laminar isothermal flow of a viscoelastic fluid around a spherical obstacle. *Journal of Non-Newtonian Fluid Mechanics*, 2:1–21, 1977.

[105] Y. Takahashi, M. Yamaguchi, K. Hori, F. Suzuki, and I. Noda. Effects of form birefringence on flow birefringence of polymer solutions in semidilute regions. *Polymer Journal*, 21(10):815–820, 1989.

[106] R.I. Tanner. *Engineering rheology.* Clarendon Press, Oxford, 1987.

[107] P. Tas. *Blown films: from polymer to product.* PhD thesis, Eindhoven University of Technology, The Netherlands, 1994.

[108] P. Townsend. A numerical simulation of Newtonian and visco-elastic flow past stationary and rotating cylinders. *Journal of Non-Newtonian Fluid Mechanics*, 6:219–243, 1980.

[109] J.S. Ultmann and M.M. Denn. Slow viscoelastic flow past submerged objects. *The Chemical Engineering Journal*, 2:81–89, 1970.

[110] M.R. van Ratingen. *Mechanical identification of inhomogeneous solids.* PhD thesis, Eindhoven University of Technology, The Netherlands, 1994.

[111] J.L.S. Wales. *The Application of Flow Birefringence to Rheological Studies of Polymer Melt.* PhD thesis, Delft University of Technology, The Netherlands, 1976.

[112] K. Walters. Recent developments in rheometry. In *Proc. XI Int. Cong. Rheology, Theoretical and applied rheology, Brussels*, Amsterdam, 1992. Elsevier.

[113] K. Walters. Proceedings of a meeting on: the rheometry of polymers, from the solution to the melt. Special edition of Journal of Non-Newtonian Fluid Mechanics, volume 52, 1994.

[114] S.A. White and D.G. Baird. Flow visualization and birefringence studies on planar entry flow behavior of polymer melts. *Journal of Non-Newtonian Fluid Mechanics*, 29:245–267, 1988.

[115] S.A. White and D.G. Baird. Numerical simulation studies on planar entry flow of polymer melts. *Journal of Non-Newtonian Fluid Mechanics*, 30:47–71, 1988.

[116] R. Wimberger-Friedl. *Orientation, stress and density distributions in injection moulded amorphous polymers determined by optical techniques.* PhD thesis, Eindhoven University of Technology, The Netherlands, 1991.

[117] R. Zheng and N. Phan-Thien. A boundary element simulation of the unsteady motion of a sphere in a cylindrical tube containing a viscoelastic fluid. *Rheologica Acta*, 31:323–332, 1992.

[118] R. Zheng, N. Phan-Thien, and R.I. Tanner. The flow past a sphere in a cylindrical tube: effects of inertia, shear thinning and elasticity. *Rheologica Acta*, 30:499–510, 1991.

[119] W. Zoetelief. On the numerical simulation of the multilayer injection moulding proces. Technical Report WFW 92.100, Eindhoven University of Technology, The Netherlands, 1992.

Samenvatting

Het gebruik van rekenprogramma's die geschikt zijn voor stromingsberekeningen aan viscoelastische polymere materialen, kan de ontwikkeling en de optimalisatie van industriële verwerkingsprocessen bevorderen, de kwaliteit van het uiteindelijke produkt verbeteren en de kostprijs reduceren. Een goed voorbeeld is de berekening van ingevroren moleculaire oriëntatie in produkten, gemaakt via het spuitgietproces. De kwaliteit van dit soort berekeningen wordt in sterke mate bepaald door de juistheid van de viscoelastische modellering van de stromende smelt via de zogenaamde konstitutieve vergelijkingen. De moleculaire oriëntatie die een gevolg is van de stromingsgeïnduceerde spanningsverdeling, is bepalend voor zowel de anisotropie van (mechanische, optische en thermische) eigenschappen van het produkt als voor het konstant blijven van de afmetingen van het produkt op de lange termijn.

In de reometrie is het gebruikelijk konstitutieve vergelijkingen te testen in enkelvoudige afschuifstromingen. Het is gebleken dat zulke stromingen niet voldoende informatie bevatten over het reologische gedrag van polymere materialen om betrouwbare voorspellingen te kunnen doen in complexe stromingssituaties (zie bijvoorbeeld Douven [32] en Tas [107]). Bovendien kunnen in veel gevallen de viscometrische funkties alleen in een relatief klein gebied van afschuifsnelheden gemeten worden. Daarbij komt dat het meten van materiaalfunkties in rekstromingen vaak onbetrouwbaar of onmogelijk is (Walters [112]).

Daarom zouden naast enkelvoudige afschuifstromingen *complexe stromingen* gebruikt moeten worden om de (parameters in) konstitutive vergelijkingen voor polymere smelten en oplossingen te bepalen. In de afgelopen twee decennia zijn er veel konstitutieve vergelijkingen voorgesteld waarmee tegenwoordig, met de eveneens ontwikkelde betrouwbare numerieke technieken, berekeningen mogelijk zijn in een redelijk ruime klasse van stromingen. De doelstelling van het huidige onderzoek is om simulaties van complexe stromingen te vergelijken met experimentele gegevens zodat daarmee de juistheid van de gebruikte modellen getoetst kan worden. Daarnaast kunnen de meetgegevens ook gebruikt worden om de modelparameters beter te bepalen. Als eerste aanzet op weg naar dit doel is in dit proefschrift gebruik gemaakt van het referentieprobleem van de stagnatiestroming rond een symmetrische en een asymmetrische cylinder. Om de vergelijking tussen experimentele en numerieke resultaten te vergemakkelijken zijn in een belangrijk deel van deze studie modelvloeistoffen gebruikt, met name een afschuifverdunnende oplossing van $5\%(g/g)$ polyisobutyleen in tetradecaan. Daarnaast is voor een smelt van lage-dichtheid polyetheen (LDPE) een verkennende analyse uitgevoerd in dezelfde geometriën.

Voor alle gebruikte vloeistoffen zijn in enkelvoudige afschuifstromingen de parameters bepaald voor twee konstitutieve modellen, het Phan-Thien Tanner en het Giesekus model. Vervolgens zijn voor twee polymere oplossingen puntsgewijs snelheids- en spanningsmetingen verricht in de stroming rondom een cylinder bij Deborah getallen tussen 0.25 en 5.61, gebruik makend van respectievelijk laser Doppler anemometrie en stromingsgeïnduceerde dubbele breking. Deze zijn vergeleken met eindige elementen berekeningen met de twee bovengenoemde modellen. In het algemeen is de overeenstemming tussen berekeningen en metingen goed. De verschillen zijn groter voor de meer geconcentreerde oplossing (9%(g/g)). Ter vergelijking zijn ook berekeningen gedaan met een, relatief eenvoudig, gegeneraliseerd Newtons model (Carreau-Yasuda). De goede overeenstemming in de snelheden impliceert dat er geen duidelijke invloed is van de normaalspanningen op het snelheidsveld. De normaalspanningen kunnen echter door het gegeneraliseerd Newtons model niet realistisch worden beschreven.

Tot slot is in een eerste analyse de stroming van een LDPE smelt rond een begrensde cylinder onderzocht. Daartoe is het gemeten dubbele brekingspatroon, bestaande uit contourlijnen van gelijke hoofdspanningen, vergeleken met het resultaat van eindige elementen berekeningen. De simulaties zijn uitgevoerd voor Deborah getallen tot 9.8. De berekende patronen stemmen redelijk overeen met de gemeten patronen. Het meest opvallende verschil ten opzichte van de berekeningen is, dat de gemeten contouren meer geconcentreerd zijn langs de wand van de cylinder en dat er een geconcentreerde 'samenvloeinaad' van de spanningen bestaat stroomafwaarts van de cylinder. Deze verschillen zijn waarschijnlijk een gevolg van onvolkomenheden in de modellen.

De belangrijkste conclusies kunnen als volgt worden samengevat. (i) De gebruikte experimentele methoden bleken krachtige hulpmiddelen om het reologische gedrag te meten in deze complexe stromingen. (ii) Voor de 5% polymeeroplossing kunnen de onderzochte planaire stromingen (met bijbehorende Deborah getallen) goed gesimuleerd worden. Bij de meer geconcentreerde oplossing zijn de verschillen groter. In een vervolgstudie voor polymeeroplossingen wordt aanbevolen om naast het gebruik van hogere Deborah getallen ook te zoeken naar een stroming, waarin de normaalspanningen een nog grotere invloed hebben op het snelheidsveld, zodat de stroming meer discrimineert tussen de verschillende modellen. (iii) In het geval van de LDPE-smelt worden de significante verschillen tussen gemeten en berekende spanningspatronen toegeschreven aan onvolkomenheden van de gebruikte modellen. In vervolgstudies moeten deze modellen dan ook verbeterd worden. Bovendien moet naast het spanningsveld ook het snelheidsveld experimenteel worden bepaald. (iv) Uitbreiding naar de analyse van het tijdsafhankelijke reologische gedrag tijdens het opstarten van de stroming rond de cylinder lijkt interessant voor een nog verder gaande evaluatie van de konstitutieve modellen.

Acknowledgement

The research project that has led to my thesis started in March 1992. An incredible amount of work had to be done and, of course, we were not aware of all kind of difficulties we were going to meet. The results described in this thesis could only be achieved by the co-operation of many people.

First of all, I would like to thank my professors Han Meijer and Frank Baaijens and my coach Gerrit Peters, who all enthusiastically supported my work. The support and advise of Gerrit Peters were invaluable. During the writing of my thesis I have appreciated the critical reading of particularly Han and Gerrit, while Frank proved to be a good travelling ambassador of my work.

The experimental work I have performed was made possible by the craftsmanship of Theo van Duppen, Sjef Garenfeld and Toon van Gils and their apprentices, who constructed all necessary equipment.

Furthermore, I would like to thank the students Marcel Schouwenberg, Joris van Dam and Peter Kruijt for their contributions. Especially, the collaboration with Peter Kruijt was fruitful. His dedicated work was of great value.

In particular, I would like to thank prof. G.G. Fuller. The impact of my thesis work was to a large extend created by the use of the Rheo Optical Analyzer (ROA), developed by him at Stanford University. I have appreciated his kind and enthusiastic support very much, particularly during his one week visit in May 1993, when he installed the ROA system in our laboratory. I acknowledge Marnix van Gurp (DSM Research), who has kindly placed his ROA system to our disposal during our first experiments.

Finally, I would like to honor my parents, who always have encouraged and supported me. Also I express my fondness to Daniëlle, who supported me with all her love and understanding.

Hans Baaijens, 22 October 1994

Curriculum Vitae

Hans Baaijens was born on February 17th 1964 in 's-Hertogenbosch, The Netherlands, where he grew up and went to the (*Gymnasium-β*) grammar school at the Jeroen Bosch College from 1976 to 1982. In august 1982, he started his Physics study at the Eindhoven University of Technology (EUT). In the late summer of 1986, he had a three-month internship at the Shell Bellair Research Center in Houston. In October 1989 he received his M.Sc. degree in Physics after completing a research project in the biomechanics group of prof. A.A. van Steenhoven (EUT) on the influence of the shear thinning behavior of blood on the flow through large blood vessels. He gratefully accepted the offer to stay in the Mechanical Engineering department to follow the post-graduate coarse Computational Mechanics that also included a continuation of his research on the non-Newtonian behavior of blood, which was now extended to the influence of the viscoelastic properties of blood. In March 1992, he received his certificate of this study. In the meanwhile, prof. H.E.H. Meijer (EUT) had offered him the opportunity to do a Ph.D. study on the evaluation of constitutive equations for polymeric liquids in complex flows. This research took place within the Center of Polymers and Composites at the EUT and eventually resulted in this thesis.

Stellingen

behorend bij het proefschrift

Evaluation of Constitutive Equations for Polymer Melts and Solutions in Complex Flows

1. Rheologen lijken soms theologen: de visie van veel rheologen die integraalmodellen verkiezen boven differentiaalmodellen is meer gebaseerd op geloof dan op feiten.

2. Boger-vloeistoffen zijn oorspronkelijk gecreëerd om rheologisch gedrag te verkrijgen dat beschreven wordt door het Upper Convected Maxwell (UCM) model. Nu echter gebleken is dat zij zich in stromingen met complexere deformaties dan alleen enkelvoudige afschuiving niet gedragen zoals het UCM model voorspelt, moeten zij geen onderwerp van studie meer zijn.

   - R.A. Brown en G.H. McKinley, *Report on the VIIIth International Workshop on Numerical Methods in Viscoelastic flows*, Journal of Non-Newtonian Fluid Mechanics,**52**, 407-413, 1994.

3. In nominaal twee-dimensionale polymeerstromingen kunnen parameters in viscoelastische constitutieve vergelijkingen relatief snel bepaald worden als het experimentele snelheidsveld en spanningsveld beide langs stroomlijnen bekend zijn. De spanningen kunnen dan immers berekend worden via integratie van de constitutieve vergelijking en direct vergeleken worden met de gemeten waarden. De ontwikkeling van deze hybride numeriek-experimentele methode zal bespoedigd worden als veldsgewijze meting van beide snelheidscomponenten mogelijk is. In vergelijking tot de *laser Doppler* methode is de *particle image velocimetry* techniek daarvoor beter geschikt.

4. Een constitutief model dat metingen in enkelvoudige afschuiving goed beschrijft, garandeert geen goede beschrijving van het rheologische gedrag in complexere stromingen, ook niet als deze planair zijn.

   - R.C. Armstrong, R.A. Brown, L.M. Quinzani, G.H. McKinley and J.A. Byars, Measurement of velocity and stress fields in complex polymer flows, In P. Moldenaers and R. Keunings, editors, *Proc. XI Int. Cong. Rheology, Theoretical and Applied Rheology, Brussels*, pages 16-23. Elsevier, 1992.
   - Dit proefschrift, hoofdstuk 5.

5. Het gecombineerd gebruik in polymeerstromingen van optische meettechnieken voor puntsgewijze snelheidsmetingen (met laser-Doppler anemometrie) en spanningsmetingen (via een dubbele brekingstechniek gebaseerd op polarisatie-modulatie), levert in *isotherme* stromingen waardevolle (rheo-optische) informatie waarmee constitutieve modellen grondig getoetst kunnen worden. In *niet-isotherme* stromingen wordt echter de toepassing van deze methoden gehinderd door de ruimtelijke variatie van de gemiddelde brekingsindex die wordt veroorzaakt door temperatuursgeïnduceerde dichtheidsverschillen.

   - Dit proefschrift, hoofdstuk 4.
   - S.R. Galante, An investigation of planar entry flow using a high resolution flow birefringence method, *PhD thesis*, Carnegie Mellon University, Penssylvania, USA, 1991.

6. Zolang bij numerieke stromingsberekeningen met visco-elastische constitutieve modellen het nog teveel een 'kunst' is om een geconvergeerde oplossing te verkrijgen, is een brede toepassing van deze berekeningen niet in zicht.

7. Het gemak waarmee computersimulaties overtuigende figuren leveren van oplossingen van complexe problemen, maakt een kritische houding ten opzichte van de verkregen resultaten noodzakelijk. Het aanleren van deze houding moet een essentieel onderdeel zijn van de ingenieursopleiding.

8. Wetenschap ontstaat als het *niet-begrijpen* verwondert. Techniek ontstaat als het *niet-kunnen* hindert.

9. De trend dat het bedrijfsleven kennisintensief, technologisch onderzoek steeds meer structureel 'uitbesteedt' aan universiteiten, en dus aan AIO's, heeft veel overeenkomsten met de vlucht van arbeidsintensieve banen naar zogenaamde 'lage-lonen landen'.

Eindhoven, november 1994 Hans Baaijens